THE UNIVERSITY
OF ADELAIDE
AUSTRALIA

Effects of the Troposphere upon Radio Communications and Implications for Weather Measurement

Nathan John Anderson

B.E. (Telecommunications, Honours)

Thesis submitted for the degree of

Doctor of Philosophy

in

Electrical & Electronic Engineering

The University of Adelaide

2018

Statement of Originality

I certify that this work contains no material which has been accepted for the award of any other degree or diploma in my name, in any university or other tertiary institution and, to the best of my knowledge and belief, contains no material previously published or written by another person, except where due reference has been made in the text. In addition, I certify that no part of this work will, in the future, be used in a submission in my name, for any other degree or diploma in any university or other tertiary institution without the prior approval of the University of Adelaide and where applicable, any partner institution responsible for the joint-award of this degree.

I give permission for the digital version of my thesis to be made available on the web, via the University's digital research repository, the Library Search and also through web search engines, unless permission has been granted by the University to restrict access for a period of time.

I acknowledge the support I have received for my research through the provision of an Australian Government Research Training Program Scholarship.

Nathan Anderson - 23 December 2017

Abstract

The aim of this research is to use observations of Very High Frequency (VHF) radio wave propagation to estimate the refractive index of air over a propagation path and subsequently the pressure, temperature, and water vapour. This can be accomplished by transmitting a known signal from one spatial location to another, and accurately timing the signal. The research develops methods for accomplishing the required measurements by means of a passive bistatic radar setup with a cooperative target. Such an approach overcomes the timing problems that are normally associated with propagation measurements. A network of these measurements can then be assimilated into a numerical weather prediction model, such as that used by the Australia Bureau of Meteorology, to increase weather forecast capability. Importantly, this research develops novel techniques to relate the propagation of radio waves from weather data. These techniques are important in their own right to identify true propagation paths.

Acknowledgements

I would like to thank many people for their continued support over the entire duration of my research and candidature. In particular, my supervisors, Christopher Coleman and Brian Ng, who provided their expert knowledge, ideas, support, guidance, and direction over the years.

I would also like to thank fellow colleagues and support staff members from the department of Electrical & Electronic Engineering, The University of Adelaide; especially, Jesse Frost, Danny Di Giacomo, and Ian Linke for their active support in research and helpful suggestions.

Additionally, I have appreciated the external assistance provided by Steve Adler (SCA), Paul Mullins (EARC), and Peter Stienle (BoM).

Most importantly, I would like to thank my family and enduring partner Jennifer, who have continually provided unconditional encouragement, patience, and support throughout my unexpectedly long duration of research candidature.

List of Acronyms and Abbreviations

ACMA	Australian Communications and Media Authority
ADC	Analog-to-Digital Converter
ACST	Australian Central Standard Time
AM	Amplitude Modulation
BoM	Bureau of Meteorology
BPS	Broadband Phase Shifter
CHAMP	CHAllenging Minisatellite Payload
COSMIC	Constellation Observing System for Meteorology, Ionosphere, and Climate
DAB	Digital Audio Broadcast
DUT	Device Under Test
DVGA	Digital Variable Gain Amplifier
DFT	Discrete Fourier Transform
DMZ	De-Militarised Zone
DSI	Direct Signal Interference
DTED	Digital Terrain Elevation Data
D-QPSK	Differential Quadrature Phase-Shift Keying
DVB-T	Digital Video Broadcasting (Terrestrial)
EARC	Elizabeth Amateur Radio Club
ERP	Effective Radiated Power
EWT	Elizabeth Water Tower
FET	Field Effect Transistor
FFT	Fast Fourier Transform
FIC	Fast Information Channel
FM	Frequency Modulation
FORMOSAT-3	Formosa Satellite Mission #3
FPGA	Field-Programmable Gate Array
FSPL	Free Space Path Loss
GPIO	General Purpose Input Output
GPS	Global Positioning System
GRACE	Gravity Recovery And Climate Experiment
ICI	Inter-Carrier Interference
IQ	Inphase Quadrature
ISI	Inter-Symbol Interference
LEO	Low Earth Orbit
LIDAR	Light Detection and Ranging

LPDA	Log Periodic Dipole Array
MoM	Methods of Moments
MSC	Main Service Channel
NASA	National Aeronautics and Space Administration
NAT	Network Address Translation
NCI	National Computing Infrastructure
NWP	Numerical Weather Prediction
OFDM	Orthogonal Frequency-Division Multiplexing
OSI	Open Systems Interconnection
PC	Personal Computer
PCB	Printed Circuit Board
POI	Point Of Interest
RDP	Remote Desktop Protocol
RF	Radio Frequency
RO	Radio Occultation
SAC-C	Satelite de Aplicaciones Cientificas-C
SAR	Synthetic Aperture Radar (SAR)
SCA	Southern Cross Austereo
SMA	SubMiniature version A
SNR	Signal to Noise Radio
UKV	Unified Model Variable Resolution
UofA	The University of Adelaide
USB	Universal Serial Bus
UTC	Coordinated Universal Time
VF	Velocity Factor
VHF	Very High Frequency

Contents

1 Research Topic Background

This section will introduce the background that is required to understand the motivation of the rest of this thesis. It will review relevant current literature on the topic and then propose how to extend the knowledge in the field by listing the aims and methods of this research. Finally, the significance of this research project will be explained.

1.1 Introduction

1.1.1 Introduction to Atmospheric Propagation

Radio waves are in continual use for wireless communications and data transfer every second of every day. The uses of radio waves are diverse; including mobile phone communications, navigation systems such as the Global Positioning System (GPS), and telemetry for deep space exploration. Radio waves are like any other wave in that they are defined by amplitude, frequency, and phase; and have a finite velocity.

The propagation of radio waves in terrestrial systems is mainly affected by the refractive index (the ratio of the propagation speed in a vacuum to the speed of propagation in another medium) of the troposphere. This refractive index is related to the common atmospheric quantities of pressure, temperature, and water vapour. It is these quantities that cause radio waves to bend as they travel through the lower atmosphere.

In the vacuum of free space (absent propagation medium boundaries), the refractive index, denoted by n, has a constant value of 1.0000 [1]. However, the tropospheric atmosphere exhibits large variations in its makeup that causes the refractive index to vary between 1.0000 and 1.0004 depending on the location and time of day. Due to these small numbers, refractivity, N, is related to the refractive index, n, by $N = 10^6(n - 1)$. Figure 1-1 shows the typical variations in refractivity. Note that the vertical structure of the refractivity changes more rapidly than the horizontal, and can vary significantly at different times.

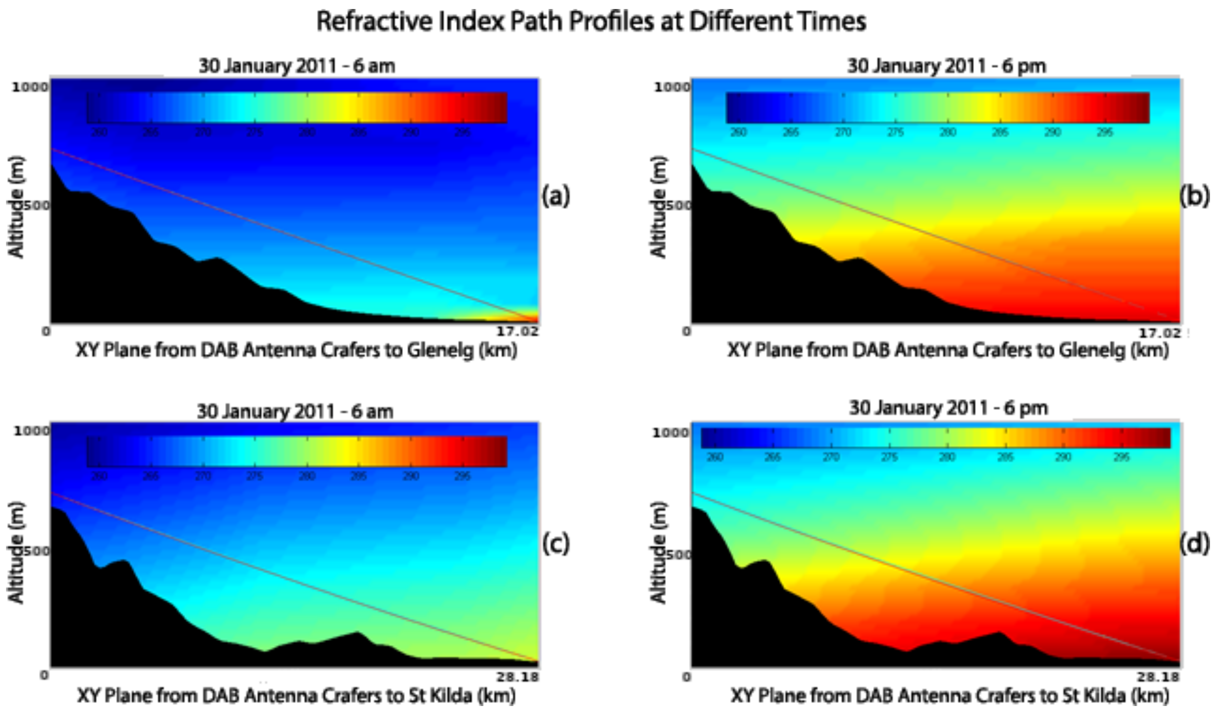

***Figure 1-1**: The refractivity (N) changes over two Adelaide paths denoted by colour. Digital Audio Broadcasting (DAB) Antenna Crafers to Glenelg at (a) 6 am and (b) 6 pm. DAB Antenna Crafers to Elizabeth at (c) 6 am and (d) 6 pm.*

The implications of the weather having an effect on radio wave propagation are numerous, including ghosting on old analogue television sets, interference in mobile networks that employ frequency reuse schemes, and further than expected signal propagation.

The purpose of the current project is to investigate the connection between weather and radio wave propagation in the lower atmosphere. Further, to investigate the possibility of using propagation observations as a means of obtaining information about current weather.

1.1.2 Current State of Research

Traditionally the way to measure refractive index throughout the atmosphere is to launch balloons with radiosondes attached. Radiosondes are expensive in both materials and labour as new ones are required for each launch [2]. Consequently, the provision of regular measurements of the vertical weather profile can be extremely expensive. Due to the expense, radiosondes are launched in sparse locations (38 locations over the whole of Australia) and are sent up only twice a day [3]. Radiosondes provide very limited data and without higher resolution datasets, it is likely that storm conditions will be averaged out and missed [4]. As a result of the limitations of radiosondes, other active detectors are used to obtain weather data; these include:

a) weather radars to detect precipitation size and wind direction,
b) weather satellites equipped with specialised sensors to detect specific atmospheric quantities, and,
c) Low Earth Orbiting (LEO) satellites to measure refractive index through Radio Occultation (RO).

Currently, considerable research [5] [6] [7] in obtaining measurements along the vertical path is focused on finding cheaper solutions than radiosondes and dedicated weather instruments by using passive solutions, such as signals of opportunity. In particular, the use of Global Positioning System (GPS) signals through RO to determine the water vapour present in the atmosphere is being actively used across the globe.

The UK Meteorological Office (UK Met Office) operates 120 GPS receivers across Europe [8], used to vertically integrate water vapour along a path. However, whilst this data has its uses, the set up does not offer high enough spatial resolution for Numerical Weather Prediction (NWP) purposes [9]. Furthermore, due to the significant path distances of the GPS signal travelling between a ground point and a satellite approximately 20,000 km higher, the spatial information that is obtained is subject to significant space-time averaging [10].

Global Positioning System Radio Occultation (GPSRO) is another attempt at using passive signals to ascertain information about the atmosphere. RO is a space-to-space method utilising two satellites' motion around the earth to observe the bending angles of a signal sent from one of the satellites to be received by the other, which is subsequently translated into a refractivity profile [11]. However, inverting this refractivity into the basic atmospheric quantities poses some challenges that will be mentioned in Section 1.2. It is for the reasons mentioned in this section that GPSRO is considered unsuitable for passive sensing in the lower troposphere.

The first attempted use of terrestrial signals to sense within the lower troposphere done in the 1950s [12] and was used to compare experimental results to the propagation theory at the time. The variation in time of arrivals of signals between line of sight antennas due to calm weather conditions is discussed in [13] and were found to be in the order of microsecond differences for transcontinental paths.

Terrestrial atmospheric monitoring using digital radio signals was proposed by Coleman et al [14]. The primary motivation of terrestrial monitoring is to decrease the cost of individual atmospheric measurements, allowing increased measurements to be made, in turn providing higher resolution datasets for NWP output. Terrestrial signals have the added benefit of minimal scintillation (fast phase or amplitude fluctuations of a signal due to electron density variations) and absence of the ionospheric effects that can be problematic for GPS techniques. The two signals used in the feasibility studies by Coleman et al were Digital Audio Broadcasting (DAB) and Digital Video Broadcasting – Terrestrial (DVB-T) broadcasts. As a result of good autocorrelation properties and synchronisation symbols, both DAB and DVB-T signals were shown to have useful sensitivity to changes in refractivity along their paths. Most importantly, given the large number of transmitters available, these signals could be used to study refractivity over a large region.

The major goal of the current work is to use radio wave timing between receivers and turn this into useful atmospheric parameters, which can be assimilated into the NWP. As part of this, the capability to assess propagation paths within an atmosphere from current NWP models is an important objective. This will enable the reverse process to develop techniques that allow radio wave propagation observations to be assimilated into NWP models. The research will concentrate on transmitters of opportunity as radio wave sources and, in particular, using the DAB system that is operating in the Very High Frequency (VHF) band at many sites around Australia.

1.2 Literature Review

The ability to obtain information without direct contact is known as remote sensing. Remote sensing was a term first used Evelyn Pruit in the late 1950s [15], but its beginnings originate in the 1800s with the discovery of infrared and photography [16]. Remote sensing can be active or passive in nature, typically measuring the sunlight or electromagnetic energy. Popular remote sensing techniques have involved aerial photography [16], or radar, e.g. Synthetic Aperture Radar (SAR) [17] or Light Detection and Ranging (LIDAR) [18]. The late 1950's and subsequently 1960's saw a shift from aeroplanes to satellites as the preferred bearer of remote sensors [19].

The first attempt using GPSRO to obtain Earth's atmospheric refractivity information from limb sounding measurements began in 1995 under the proof of concept GPS/Meteorology (GPS/MET) experiment [20]. Based on earlier studies of solar system exploration with the atmosphere on Mars [21], they used the refractivity to compute temperature along the path so long as water vapour was negligible. Despite this limitation, further missions were launched; Satelite de Aplicaciones Cientificas-C (SAC-C) launched in 2000 [22], CHAllenging Minisatellite Payload (CHAMP) in 2001 [23], and Gravity Recovery And Climate Experiment (GRACE) launched in 2002 [24]. Following the successful RO measurements of the upper troposphere and lower stratosphere from the CHAMP and GRACE missions [25], the first constellation of 6 satellites dedicated to RO was launched in 2006 [26], dubbed Formosa Satellite mission #3 (FORMOSAT-3)/Constellation Observing System for Meteorology, Ionosphere, and Climate (COSMIC), referred to solely as COSMIC in the United States of America. COSMIC produces between 1500-2000 global soundings every day and has shown to have constructive impacts for weather forecasting [9]. A future mission is already planned to replace COSMIC to increase the number of soundings made through RO, named COSMIC-2 [27]. Further discourse into how RO works is given by National Aeronautics and Space Administration (NASA) in [28].

The accuracy of the results obtained from occultation observations has been measured by comparing the COSMIC observations to that of independent observations from radiosondes currently employed by weather bureaus [29]. Here, the author compared observations from both methods from atmospheric pressures 200 to 10 hPa (≈12 to 25 km above ground – where water vapour is negligible), and found that the accuracy of the RO temperature observations were better than 0.13 K for the tested region. Measurements made from CHAMP GPSRO satellites have been inserted under test conditions (not real-time) into the MET office's NWP and it was found to reduce the Root Mean Squared (RMS) error associated with forecasting temperature by approximately 0.1 K in the Southern Hemisphere [30]. This author noted that the MET office has the capability to assimilate RO measurements into the NWP as refractivity profiles which is less computationally expensive. Further, the bending angles themselves can be directly assimilated in the models if desired [31].

Despite the advantages provided by GPSRO, it is not without limitations. When water vapour is present in the atmosphere, the method is unable to compute either temperature or water vapour without knowing the other's information [32]. This is because refractivity depends on three quantities (temperature, pressure, water vapour) and inversing the process to find the three quantities is only independently possible providing there is no water vapour present. When only two of the quantities are present, the methods described in [10] [32] explain how using the hydrostatic equation and ideal gas law can be used to derive the refractivity inversion. Consequently, GPSRO does not provide adequate data within the lower troposphere. Neural networks are being investigated as a method to retrieve temperature, pressure and humidity without prior knowledge of atmospheric parameters [33]. However, this proposed method was only tested with arctic data with predictable water vapour constraints.

Surface weather measurements using radio waves are also possible. Using the phase of signals to sense refractivity variations within the lower atmosphere was initially attempted in the 1950s by J.W. Herbstreit and M.C. Thompson [12]. The authors critically recognised the inhomogeneous nature of the atmosphere over radio paths, and also recognised that the phase of arrival of a signal is subject to this inhomogeneous atmosphere. With an experimental setup of a transmitter atop Cheyenne Mountain (≈2.7 km high) and a receiver at Colorado Springs (≈1.8 km high) separated by approximately 5.5 km, they measured the change of phase of a signal at each end over both a single path and also with a signal arriving over the first path as well as an adjacent path (two received signals). At the receivers, independent measurements of the refractive index, wind, relative humidity, temperature, and barometric pressure were taken using unspecified methods. They recorded phase differences between the paths and found that the standard deviation of the phase differences was 'very nearly' directly proportional to the radio frequency. Despite this, they found no correlation between meteorological data and radio data, but admit this may have been due to inadequate meteorological data along the path. This method required the transmitters to have stable phase characteristics such that phase fluctuations must be much greater than source fluctuations.

Using digital broadcasts to observe environmental effects was proposed in 2008 due to an ever-increasing amount of suitable digital transmitters becoming available [14]. Motivated by the weak GPS signals used in a similar fashion, the authors analysed the ambiguity function from DAB signals in the United Kingdom. Over a short time frame, they recognised fluctuations in the signal's amplitude, which hinted at using terrestrial signals to monitor atmospheric variations.

Expanding on this idea in 2010, preliminary feasibility studies were carried out by Coleman and Watson [9]. Again, DAB and DVB-T signals were used as they contain phase synchronisation symbols that can be easily tracked when the signal is demodulated. These signals also provide good autocorrelation properties. They found the phase stability of the transmitters to be inadequate, and instead had to measure phase differences at the receivers, requiring the receivers to be highly synchronised. The study proposed that using this method would yield path-averaged refractivity which could then be assimilated into the NWP or inverted using tomographic approaches. The study also demonstrated the autocorrelation function and noted that over several hours, changes in signal amplitude can be seen which is attributable to changes in refractivity affecting the propagation of rays.

Since this thesis work begun in 2012, a separate group in Japan [34] independently approached a comparable goal of this thesis to improve the accuracy of the numerical weather forecast. They estimated water vapour near the ground via radio wave propagation. While this thesis aims to use DAB transmissions, the group from Japan used DVB-T. The work differs further as they use natural reflectors that included buildings and transmission line towers, whilst this project employs an active repeater that can generate a larger radar cross-section, which is more applicable over longer distances. The group from Japan also match the phase measurements via a local oscillator at the receiver, which introduces a systematic error within a relative measurement. Nevertheless, their results showed promise and potential for similar approaches that this thesis work explores.

1.3 Objectives of the Thesis

This project will extend on the preliminary terrestrial sounding work by Coleman et al [9]. Initially efficient methods for calculating radio wave propagation under given atmospheric conditions will be developed. This forward model can then be used to relate propagation observations back to weather by assimilation into NWP models. In order to assimilate the large quantity of data that will be produced by observations, the propagation analysis techniques should be extremely fast to be usable in forecasts. In addition, these techniques should be able to capture the effects of important weather features such as fronts (a weather front is when a cold mass of air sharply approaches a warm mass of air, causing the temperature difference to change over a very short distance). The propagation models will also be useful in their own right as a means of providing propagation predictions given available weather data.

The project will also further develop the methods for measuring the propagation effects themselves. In particular, methods based on artificial radar targets will be investigated. These methods avoid some of the timing issues that are inherent in previous approaches introduced earlier, and discussed later in Section 3.2.1. The core hypothesis of the thesis is that there exists a measurable influence that tropospheric weather has on terrestrial radio wave propagation.

1.4 Methods

In order to add observations into the NWP, propagation paths need to be accurately modelled in given weather conditions (1.4.2) in order to enable radio link timing measurements to be used as a way of determining atmospheric structures (1.4.1). This section briefly introduces concepts on how to accomplish these goals. Detailed explanations are found in the subsequent chapters.

1.4.1 Determining Atmospheric Quantities from Terrestrial Signals

The major objective is to develop techniques that add detail to the NWP model through the assimilation of radio wave propagation data. This can be achieved by measuring the time of flight of radio waves, converting the measurements to refractivity profiles and then to atmospheric quantities.

There are two different systems to measure the time of flight of a signal; the first being the use of a single receiver with a repeater similar to an artificial radar setup. In this scenario the transmitter is separate to the path under test, and the transmitted direct signal first passes through the receiver, with an indirect signal coming over from the path of interest reflected by a repeater. With this approach, only a single receiver is needed to time the signals, with the assumption that the repeated path is the same path of the continuing direct signal. The second approach is to use multiple receiver stations all set up and capable of measuring time of flight of signals down to synchronised nanosecond accuracies using a GPS time stamping unit added into the receiver chain. The time stamps are identified either by signal level step functions, or if demodulation is performed, the pilot symbols can be tracked. Simplified topographies for the above scenarios are shown in Figure 1-2.

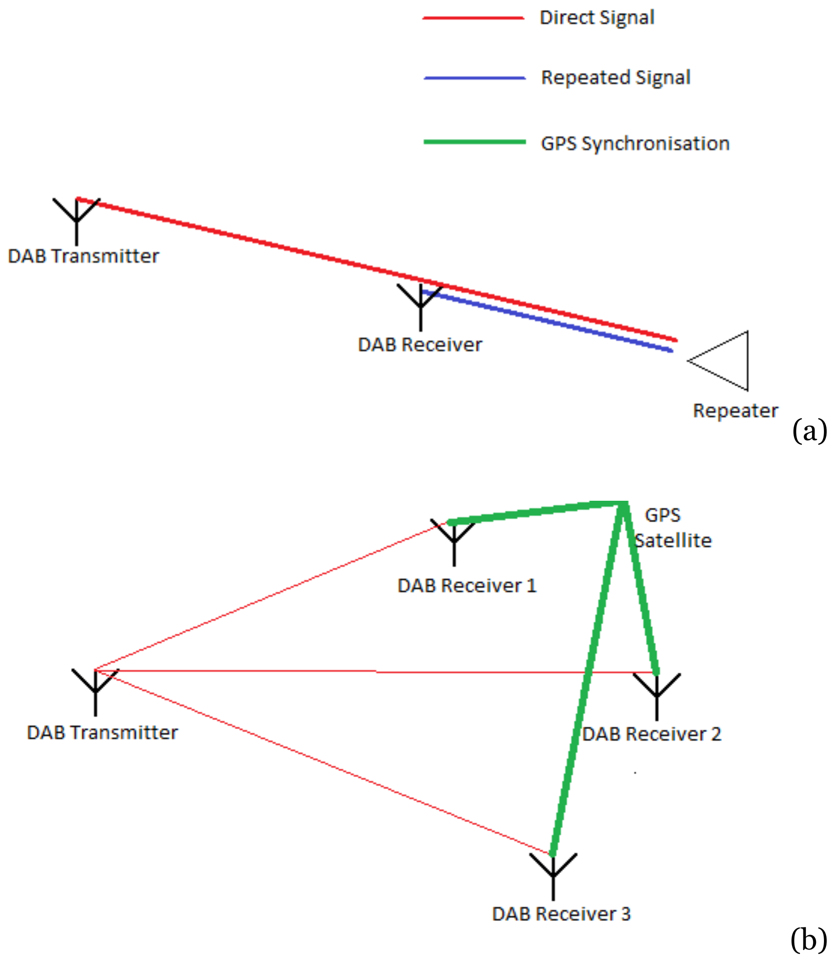

Figure 1-2*: Two different systems used to measure time of flight of signals. (a) Single receiver repeater configuration. (b) Multiple receivers using GPS timing.*

Due to the relative ease of the single receiver configuration (Figure 1-2a), this will be the chosen method to develop propagation weather data in this project. The advantage to using the single receiver configuration is the simplicity of the method as all of the time synchronisation issues can be avoided when the timing is done at one receiver. The direct and repeated signal can be relatively compared to observe the time difference over the path of interest. The major difficulty with this approach comes from Direct Signal Interference (DSI) [14]. Depending on the distances and signal gain over the direct and repeated paths, it is possible that the direct signal will have significantly more power than the repeated signal, swamping out the second signal. This issue can be minimised by retransmitting with cross-polarisation at the repeater and by choosing a direct path that attenuates the signal from the transmitter. It is generally the case that the time scales of propagation are very much smaller than those of the atmospheric variations [12], which are assumed to be a constant during a measurement.

The receiver must be placed in DAB or DVB-T coverage areas and at sufficient distances (between 20 - 60 km) from the transmitters such that flight times differ appreciably from straight-line propagation. With the time of flights recorded by autocorrelation of a repeated signal, and the theoretical straight-line propagation path known, the path refractivity can be obtained. The time of flight, t, along a path is related to the refractive index, n, via substitution:

Since $t = \frac{d}{v}$ and $n = \frac{c}{v}$,

$$t = \frac{nd}{c} \qquad \text{1-1}$$

where n is the refractive index,

c is the speed of light in a vacuum (m/s),

v is the velocity of propagation (m/s),

d is the distance (m).

The refractive index can be related to atmospheric quantities pressure, temperature, and water vapour using the empirically derived two-term relationship [35]:

$$N = \frac{77.6P}{T} + \frac{3.73 \times 10^5 e}{T^2} \qquad \text{1-2}$$

where $N = 10^6(n - 1)$,

P = atmospheric pressure in millibars (200 mb < P < 1100 mb),

T = temperature in Kelvins (240 K < T < 310 K),

e = water vapour pressure (0 mb < e < 30 mb).

This is the relationship relating radio wave propagation to weather. A more recent and accurate three-term relationship for refractivity is given in [36], however has not been printed here due to the length of the empirically derived coefficients.

Given the source and transmitter locations are known, the straight-line path between the two is known and it is trivial to estimate the straight-line time of flight under given weather conditions. The atmospherically bending path of propagation is longer than this straight-line path and a proposed method for determining this true propagation path will be discussed in section 1.4.2. Consequently, actually measuring the time of flight by autocorrelation at the single receiver will present a different result to the calculated straight-line time estimation. This difference is due to the changes in the refractive index over the path causing the propagation of the wave to have deviations from a straight-line. Assimilation of the time of flight data into the NWP (if not directly assimilating refractivity) can only be used if the data can be inverted into pressure, temperature, and water vapour from the refractivity information. As discussed in Section 1.2 about GPSRO refractivity inversion, the presence of water vapour in the troposphere complicates retrieving atmospheric parameters directly from refractivity and other sources of data are required to complete the inversion (discounting neural networks). Simple use of lapse rate modelling or independent data observations can facilitate finding solutions to the atmospheric quantities along the path. With the quantities solved, the data can be assimilated into the NWP model and used to correct weather predictions in a direction consistent with the observations using a process similar to Kalman filtering with feedback loops. Alternatively, if sufficient path measurements are made, tomographic techniques [37] [38] can be used to build a local model of refractive index.

It is evident that for the above scheme to be useful there needs to be considerable resources both in terms of transmitters and receivers. The UK has a lot of the infrastructure required for the transmit side as it already has 103 active transmitters compared to 7 transmitters available in Australia. The University of Bath is also active in this area of research and has appropriate receivers with more deployed with GPS time stamping capabilities since September 2012. Consequently, partial propagation research using the available data from the UK was carried out while at the University of Bath. Adding receivers in Australia for local research commenced in 2013 following the work done in Bath.

1.4.2 Propagation Calculations

A major objective of this thesis is the development of models that can calculate radio wave propagation from meteorological data, in particular the weather maps provided by various meteorological bureaus. This is an essential prerequisite to the data assimilation component of the work. Initial evaluation studies have concentrated on weather maps with a 4 km NWP grid (South Australian, North Atlantic and European) which, unfortunately, can only crudely capture variations of atmospheric quantities over typical radio paths. Plans to move to the Unified Model Variable resolution with 1.5 km grids (UKV) will allow atmospheric quantities to be characterised more precisely on local scales [39]. Both models have an upper limit of more than 40 km in altitude [40], however only the first kilometre of the lower troposphere will be processed as it is expected that all DAB transmitters and receivers will be situated within this region (it is not difficult to modify the height limit). Both models will also run every 6 hours, whilst data points are provided for every hour.

An important issue concerning various radio paths in order to produce atmospheric data at arbitrary points (and hence the refractive index) is the interpolation of the NWP gridded data. Simple linear interpolation can be used, but ultimately, a more sophisticated interpolation will be required. Special care will need to be taken at weather features such as fronts. Real time computation considerations currently prohibit any global interpolation methods, as the data sets are too large.

Calculation of physical radio wave paths is achieved through Fermat's principle [41]. In free space, the propagation path of a radio wave is a straight-line as the refractive index is constant, however in the presence of an atmosphere (i.e. what is in the troposphere) where the refractive index of the medium changes subject to both space and time, the propagation ray will bend. The ray of propagation will follow the path of minimum travel time caused by the refractive index changes along the path, and this is known as Fermat's principle of least time. Formally Fermat's principle is expressed as followed (for the path taken along the path of minimum time):

$$\delta S = 0$$

where

$$S = \int_a^b n \, ds, \qquad 1\text{-}3$$

where S = integral along the stationary optical wavepath from a to b, and,

ds is the infinitesimally small distance along the path.

It should be noted that Fermat's principle implies that changes in S will only be second order in terms of variations in the path geometry.

As the path end points are known transmitters or receivers at a and b, weather models can be used to determine the refractive index and hence true path taken by the wave. Once the propagation path is known, the ground elevation between the two points needs to be studied for possible diffraction effects (i.e. the Fresnel clearance needs to be calculated using through Digital Terrain Elevation Data files [42]).

At the lowest degree of approximation, the bending of the propagation path due to the principle of least time can be approximated by a parabolic deviation to a straight-line. This is usually adequate under normal weather conditions (i.e. the absence of ducting and sharp fronts), and can be subsequently refined by increasing the order of the polynomial or by representing the path as piecewise polynomial. The unknown polynomial coefficients are obtained through Fermat's principle. Essentially, this means that the coefficients will be obtained through numerical optimisation routines. The accuracy of the path estimation is limited by available computing power, real time processing limitations, and the required minimisation tolerance. Developing an analytical solution fitting a first order estimate will also be important to use a best 'first guess' for the path with a minimal flight time.

Prior to assimilating data derived from radio propagation measurements mentioned in the previous section (1.4.1), the un-assimilated (original) NWP data is required to have enough information to determine this path of minimum travel time. Keeping the system real-time capable is important because the original NWP output is required to subsequently refine values along the propagation paths where the timing measurements are made. This is because the radio timing values from Section 1.4.1 are supplementary observations to the original model outputs.

As fronts are where radio waves significantly deviate from straight-line estimations and even polynomial estimations, care and effort needs to be taken to detect fronts along the propagation path. Whilst numerical optimisation can be used to automatically find the minimum path, this is extremely time consuming to the point of being unacceptable in a real time system. If fronts can be detected along the radio path, then the parabolic path estimations can be adjusted accordingly, or in the case of numerical optimisation, better initial conditions can aid faster convergence towards the minimum path. With the minimum time propagation path known, phase shifts, wave numbers, and ray angles can be compared to the straight-line path.

1.5 Research Significance

Using the above methods will help augment the expensive radiosonde launching network and provide increased spatial information. In particular, it will provide continuous measurements in areas that are not accessible to ground based instruments and data only previously available through radiosonde observations or GPS occultation. This new dense data set will allow the tracking of irregular weather conditions such as fronts and ducting, causing further than expected signal propagation as shown in Figure 1-3.

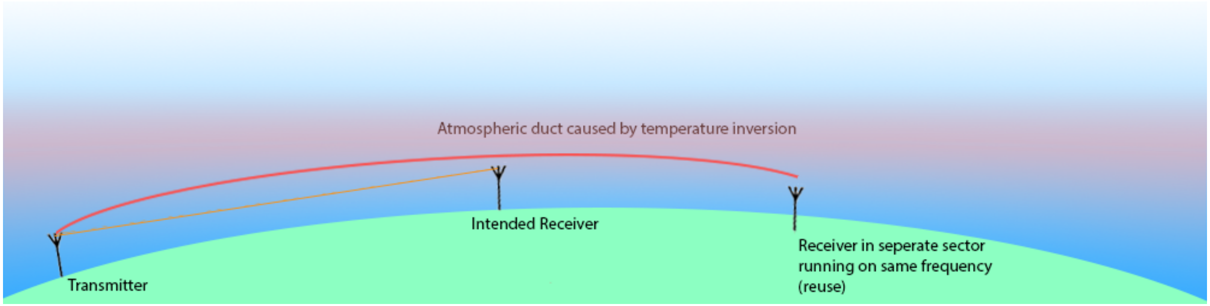

***Figure 1-3**: Temperature inversion (increasing temperature with height) causes radio waves to be refracted back down towards earth.*

The completion of the objectives described for this project has several possible significant impacts, including:

- Weather data – Increasing the granularity of Bureau of Meteorology's (BoM) NWP output will benefit all users interested in weather conditions, e.g. aviators, and forecasters.
- Bushfire and severe weather monitoring – Real-time processing of data provides early detection by flagging atmospheric conditions associated with bushfires or other severe weather conditions, e.g. storms.
- Defence and law enforcement – Identification of a signal of interest could be reverse-analysed to find possible signal source locations. Propagation predictions can also be provided given available weather data, which is important for radar operations.
- Telecommunication & media industry – Providing more accurate coverage maps and better planning of mobile sites.

1.6 Summary of Thesis Contents

Chapter 2 delves into capabilities of the tool developed to calculate the true path of propagation based on atmospheric conditions.

Chapter 3 investigates the problem of timing radio waves and the best method to overcome associated issues, and includes potential solutions to direct signal interference.

Chapter 4 describes the setup of all the hardware required and used for recording the time of flight over the repeated path.

Chapter 5 proposes several methods to obtain the time of flight from the recorded data.

Chapter 6 collates results over several months and compares them to the independent observations provided via BoM.

Chapter 7 discusses the results obtained, and how results reflect on atmospheric conditions. Sources of error are analysed for their effect.

Chapter 8 proposes suggestions for future work building on this project's findings.

Chapter 9 concludes this thesis, briefly overviewing the work done and results obtained, and provides future recommendations for continued work in this area.

2 Signal Propagation

For atmospheric radio wave propagation, the assumption that the ray propagation follows a straight-line path originating at the transmitter source is only acceptable as the lowest order of approximation. Specialised applications, such as the present work, requires a more detailed knowledge of the propagation. The path of propagation (also called the ray path) will always satisfy Fermat's Principle of Least Time [43] and the current chapter documents the development of a tool to find the propagation path based on this principle.

The main aim of this chapter is to gain a theoretical understanding of the effect of weather upon propagation. Such knowledge is required to then make inferences on the weather from observations of radio wave propagation. The primary observable factor is the time of flight between the transmitter and receiver. Fermat's principle states that the effect of deviations of the propagation path from linear will only have a second order effect upon this time of flight. Consequently, for a first approximation, it is reasonable to calculate the time of flight assuming the propagation path is a straight-line. It is important, however, to ascertain the impact of neglecting the deviations in path from linear. In order to uncover the true propagation path, software has been written (Sections 2.3 to 2.6) for this research that finds the path between two end points that gives the minimum travel time (i.e. satisfies Fermat's Principle of Least Time). The techniques of this chapter are validated by means of a model solution that is obtained by an independent method. It is assumed the reader is already familiar with the inhomogeneous nature of the atmosphere, but introductory knowledge can be found in [44].

2.1 Background

Physical propagation paths do not follow an idealised line, but rather bend through space as a function of the refractive index along the path. The work of this thesis requires that the actual propagation path be discovered for two main reasons:

1. The time of flight of a signal is affected by the propagation path, and,

2. The physical path taken by the wave is the path on which this work will derive path averaged refractivity.

Elaborating on the first reason, take the local experimental scenario of propagation between the DAB transmitter located at Crafers and a receiver located at Elizabeth (see Figure 3-4). Assuming linear propagation, the propagation time is 95.9322 µs. Taking into account a constant atmosphere's presence in place of free space, and a straight-line path from transmitter to receiver, a more realistic value of 95.9581 µs is obtained. If, however, the curvature of the propagation path was included due to changing refractivity along the path, a value of 95.9531 µs is obtained from the written software. Whilst the differences may appear small, perhaps even negligible, it would be premature to say that this research should ignore these small differences. This would especially be the case if the effects were exacerbated by strong gradients in refractive index or turbulence [12]. Moreover, while the absolute time difference is small, the VHF used by DAB transmissions cause the phase difference between the true and estimated paths to be amplified, as demonstrated in the equation 2-1:

$$\theta = 360 f \Delta t \tag{2-1}$$

where θ is the phase difference (°)

f is the frequency (Hz),

Δt is the time delay (s).

This means, for the case of the free space versus actual propagation time difference mentioned above, $\Delta t = 95.9581\ \mu\text{s} - 95.9531\ \mu\text{s} = 5$ ns, which when substituted into equation 2-1, using a DAB frequency of 204.64 MHz, results in a phase difference between the two signals of 368.352°, or put another way, more than one complete phase cycle. It is clear that, even though the effects path curvatures are small, it could still amount to substantial phase changes.

The importance of the second reason is that the subsequent steps will use the phase changes to infer the behaviour of the refractive index on the propagation path. Consequently, if the path curvature is large, the propagation tool could end up assigning a refractive index value to the wrong region of space.

Thus, it is evident now that capturing the actual path of propagation through the lower atmosphere is required. According to Fermat's Principle, this bending of the propagation path is such that the path taken between two end points is always the one taking minimum time [41], and is affected by the refractive variations of the medium between these end points. The time of propagation through refraction can be expressed by equation 2-2:

$$T = \frac{1}{c}\int_{A}^{B} n\,ds \tag{2-2}$$

where T is the time (s),

c is the speed of light in a vacuum (299 792 458 m/s),

n is the refractive index,

and the integral is taken along the path of propagation from A to B along an infinitesimally small distance along the path ds.

In general, the path of propagation is the one that gives a stationary optical path (equation 2-3):

$$\delta S = \delta\int_{A}^{B} n\,ds = 0 \tag{2-3}$$

where S is the stationary optical path,

n is the refractive index,

and the integral is taken along the path of propagation from A to B along an infinitesimally small distance along the path ds.

Another common way of finding physical ray paths is using Snell's Law [45], a law that follows on from Fermat's Principle of Least Time. This law relates the angle changes in propagation to the refractive index changes at each boundary:

$$\frac{\sin\theta_1}{\sin\theta_2} = \frac{n_2}{n_1} \qquad \text{2-4}$$

where θ_1 is angle of incidence (°),

θ_2 is angle of refraction (°),

n_1 is refractive index of medium 1,

n_2 is refractive index of medium 2.

Applying either of these equations (either 2-3 or 2-4) will yield the physical path taken by a wave when the location of the source transmitter and destination receiver are both known, provided that the background atmospheric information is also known.

2.2 Appropriate Solutions

While analytical solutions will give rapid answers, simplifying assumptions are required to avoid significant mathematical complexity when attempting to find a true path. Ultimately this type of solution will sacrifice accuracy in the best case of atmospheric variations (layered atmosphere varying only in the vertical axis), and be wildly inappropriate in the worst atmospheric cases (turbulent, inverted atmospheres varying along the horizon with moving fronts). A numerical estimation approach offers robustness for all weather scenarios and provides the highest accuracy available, and only limited by source data and computational time.

There were several requirements for the software being developed to find the minimum path:

- It must retrieve the highest resolution atmospheric data available from any given time or date (provided that the data sources exist),
- It had to work for both the UK and Australia radio paths at any given time or date (provided the data sources exist) for collaboration purposes,
- It had to be capable of 3D variations,

- It had to be fast enough to be used in real time to be beneficial to current weather prediction services, and,
- It had to be capable of running either silently outputting the minimum path or displaying verbose information when required.

The variations in the atmospheric refractive index in the first kilometre above ground occur much more rapidly in the vertical axis (-40 N/km) than the horizontal [43]. This leads to path deviations occurring more noticeably along the altitude than over either latitude or longitude. Although the deviations along the latitude and longitude may be minor in comparison to the vertical axis, for completeness the software is capable of evaluating 3D variations within the numerical optimisation routines.

2.3 Propagation Path Calculation

To determine the true path of propagation taken by a wave through the atmosphere, specialised software to apply the refraction theory to the atmospheric realities is required. For a first attempt at a propagation algorithm, it was assumed that the propagation path formed a parabola whose maximum point was exactly half way between the transmitter and receiver locations.

Under normal weather conditions, the changes of refractive index within the atmosphere can cause the ray to bend and extend over the horizon which forms the parabolic path, deviating from the simplistic straight-line assumption. Figure 2-1 shows the effect of altitude on several important atmospheric quantities (particularly pressure, vapour pressure, and temperature), all demonstrating decreasing values with respect to altitude (lapse rate) and this causes the refractive index to decrease with height. This generalisation provides a fast algorithm that gives an estimate of the order of magnitude of path deviations.

Extending this approach by breaking the path up into a larger number of segments (n_s), the tool can obtain more accurate results. Essentially, the time of flight now becomes a function of the parameters that describe the multiple segments (or the parabola in the initial approach) and Fermat's Principle implies that the correct propagation path will be that with the parameters for which the function is minimum.

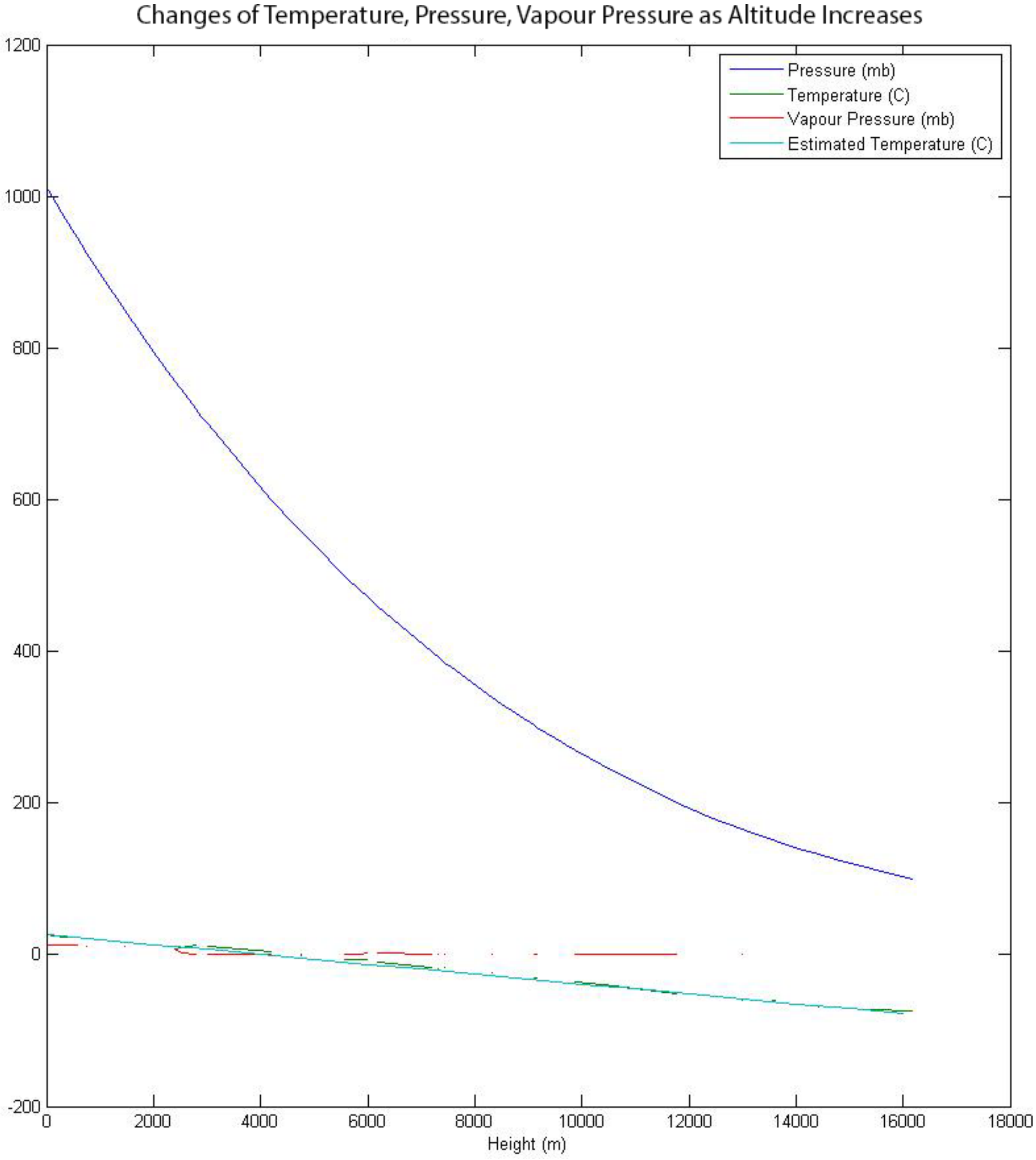

***Figure 2-1**: The change of atmospheric quantities with respect to height in Adelaide, South Australia, on a typical spring day (the absence of points indicate no data). Sample data provided by the Bureau of Meteorology.*

To apply Fermat's Principle [41] (Equation 1-3) for atmospheric purposes, the algorithm requires the input of both the transmitter and receiver locations and atmospheric state between these two end points. The software algorithm will need to accept different data sources of the atmospheric state; in particular, it will be designed to handle data derived from both Australian and British sources. In Australia, the BoM provides NWPs of the required weather parameters that are defined over a regular grid, whereas the UK MET office provides NWPs over a warped grid due to their proximity to the Earth's North Pole. Depending on the coordinates entered, the software will automatically determine whether the path is over the UK or Australia and retrieve atmospheric data accordingly, whilst taking into account the warping nature of the UK data sets. It also retrieves ground terrain elevations provided by the publicly available 30 arc second resolution Digital Terrain Elevation Data (DTED) Level 0 data sources [46] along the path, or the finer 3 arc second DTED Level 1 files if available. Terrain heights used within the NWP are on a grid four times as coarse as the publicly available DTED heights, and so are only used to reference gridded data points above the ground. Both Australia and UK atmospheric data sources come on a 4 km by 4 km grid with the vertical detail focused closer to the ground. It is anticipated that in the immediate future that the experimental UKV model featuring 1.2 km by 1.2 km gridded data sets will be released for public usage, which will provide finer resolution data and lessen the program's computational time spent on interpolation between grid points. The current program has the capability of seamlessly switching between either grid formats.

Each 3D gridded data point provides a value for pressure, vapour pressure, and temperature. From this, the refractive index is calculated at each point using the two-term relation from equation 1-2 used since 1953 for an accuracy 0.5% (2N) for frequencies up to 30 GHz. Optionally, the more recent (1973) three-term relation for the refractivity [36] can be used to increase the accuracy of results to 0.018% (0.05N) in dry air.

With all necessary information gathered, a straight-line path is calculated between the end points after converting the geodetic coordinates to Cartesian coordinates. This straight-line is used to assess whether the path is valid and not obstructed by the Earth's terrain, or whether the terrain will influence the signal of propagation by mechanisms such as diffraction. The path is broken up into a number of segments, n_s, and the atmospheric refractive index, wave velocity, and time taken to pass through the segment is calculated using equation 2-2. These line segments do not necessarily lie on the data points of given atmospheric data and so it is necessary to interpolate (e.g. Figure 2-2) the points of interest within the given 3D data.

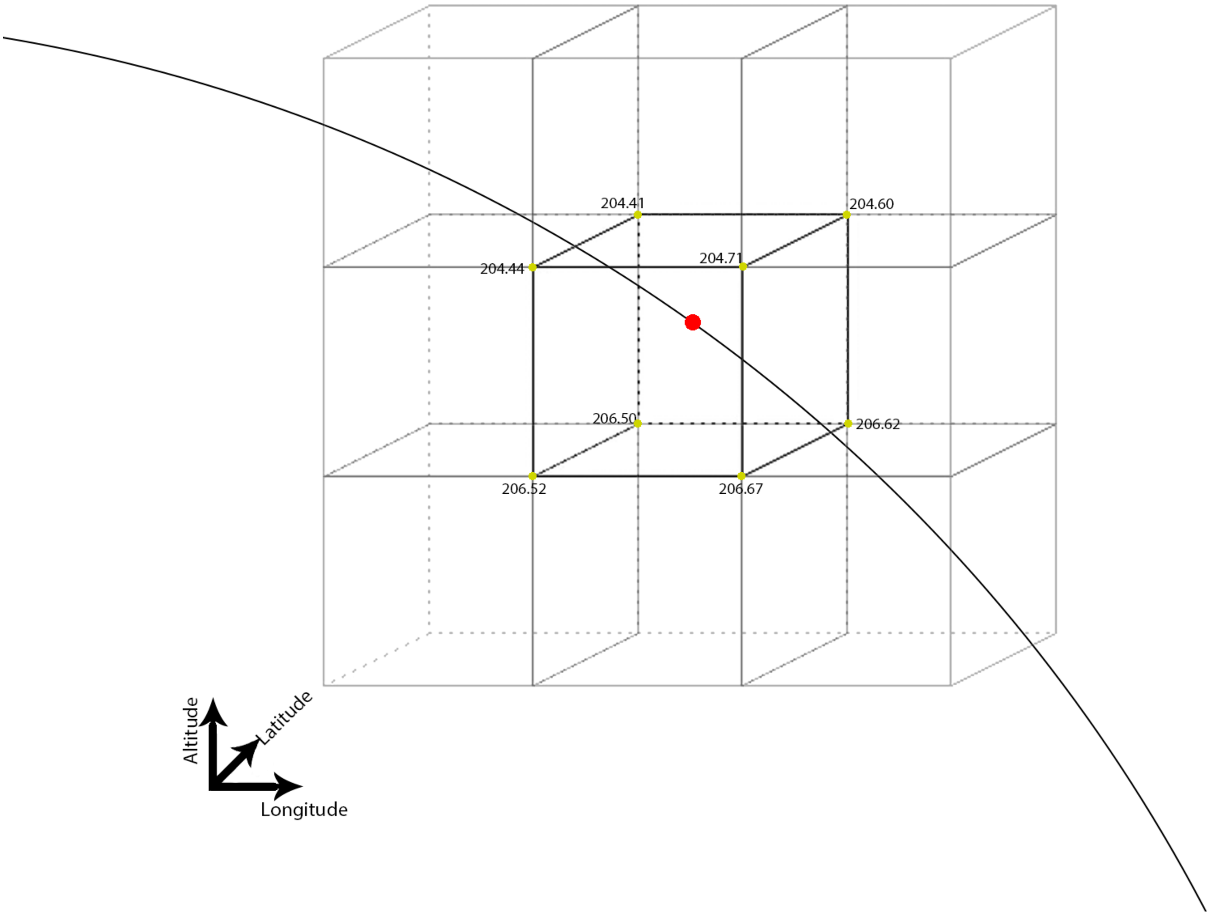

***Figure 2-2**: A ray shooting through gridded refractive index data points. To find the value of the arbitrary Point of Interest (POI) along the ray, use surrounding grid values and interpolate.*

In Figure 2-2, the vertices of each 3-D grid are refractive index values. These refractive index values are derived from the data given by the NWP. The actual value of the Point Of Interest (POI) along the path marked by a red dot is unknown and requires interpolation. Numerous methods of interpolation exist; some taking into account the eight immediate vertices (e.g. nearest neighbour, trilinear), some using several surrounding points of data (e.g. tricubic), possibly irregularly spaced (e.g. kriging, splines), and others taking into account the trend of values over the whole data set.

For reasons of real-time processing, and for preserving abrupt atmospheric changes present in weather fronts, the points in the software are interpolated by the trilinear method. This method uses a weighting of the surrounding eight local points linearly interpolated over each axis.

Each of the three spatial dimensions are interpolated sequentially. Whilst the order does not matter, used here is [longitude, latitude, altitude]. The POI within the data set is directly influenced by the distance from each surrounding vertex. NWP gridded data is not quite a symmetrical cube and is handled accordingly, and Figure 2-3 illustrates the fundamental process to estimate the value of the POI on a regular cube.

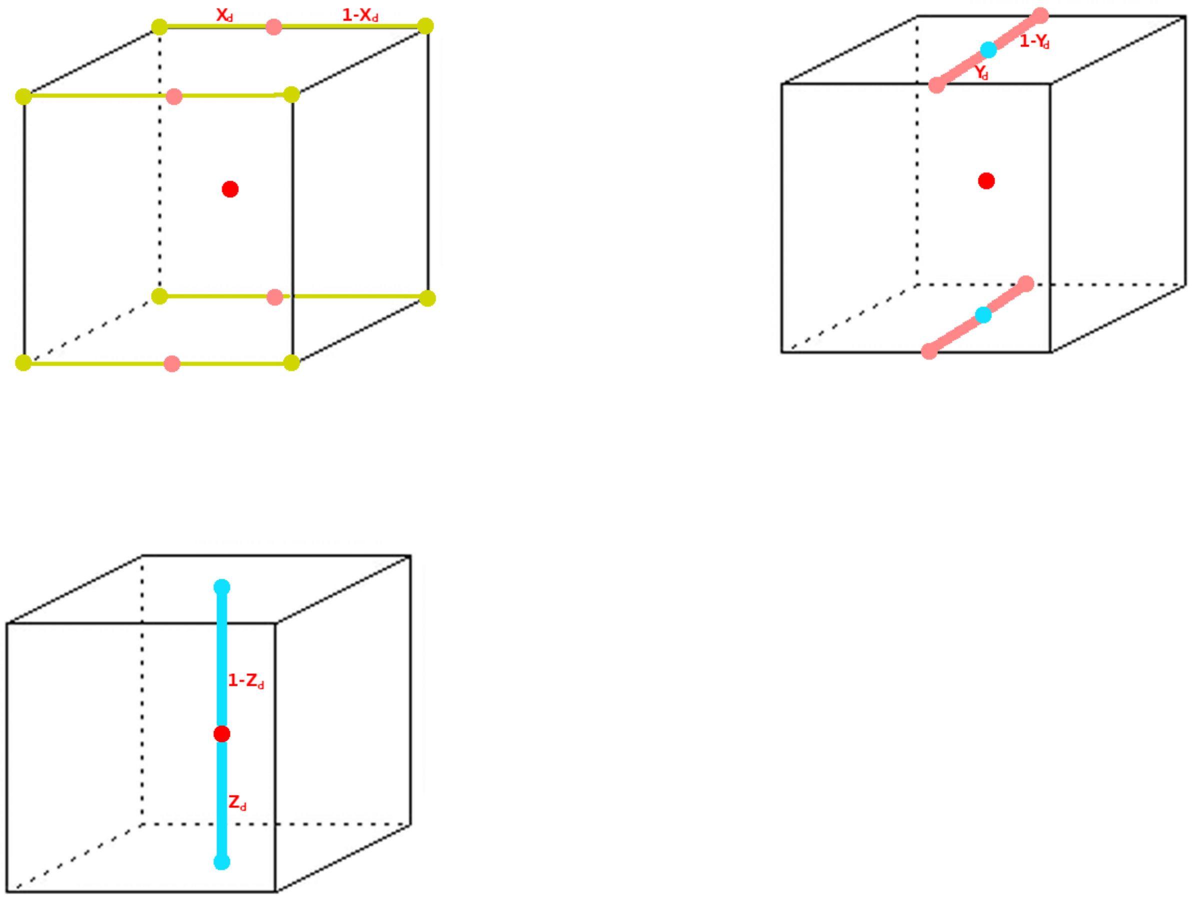

__Figure 2-3__: Three sequential linear interpolations results in a trilinear interpolation regardless of order.

The trilinear interpolation shown in Figure 2-3 is a simple but appropriate interpolation choice within gridded atmospheric data. Further details of tested alternative interpolation methods can be found in Appendix A.

The use of this interpolation allows retrieval of atmospheric data for wherever these line segments lie. All the time segments are then summed over the path to give an estimate of the total propagation time. Finding the true propagation path requires the minimisation of the propagation time with respect to all possible paths between the end points of the propagation path. In reality, this is a minimisation with respect to the parameters that describe the path segments. Such optimisation is done either through finding a constrained minimum of a scalar function or a pattern search (further details of both can be found in Appendix B).

2.4 Overview of an Example of Propagation Software Execution

Using an example of a test path from a transmitter atop Crafers Hill, South Australia, to a receiver at Glenelg, South Australia (GPS Coordinates shown in Figure 2-4), a step-by-step execution of the propagation tool is presented here to clarify the previous Section 2.3.

The first stage of the software finds a first guess propagation path with simple polynomial approximations.

a) The desired endpoints and atmospheric conditions are provided,

b) Atmosphere information is loaded and the geometric line between endpoints used as a base path,

c) The linear path is perturbed in the vertical direction (height) to form a concave quadratic path and the space of perturbations search to find the quadratic path that gives the minimum time of propagation. According to Fermat's principle, this will then provide an approximation to the real propagation path, and,

d) The parabolic path can then be improved using cubic and quartic functions.

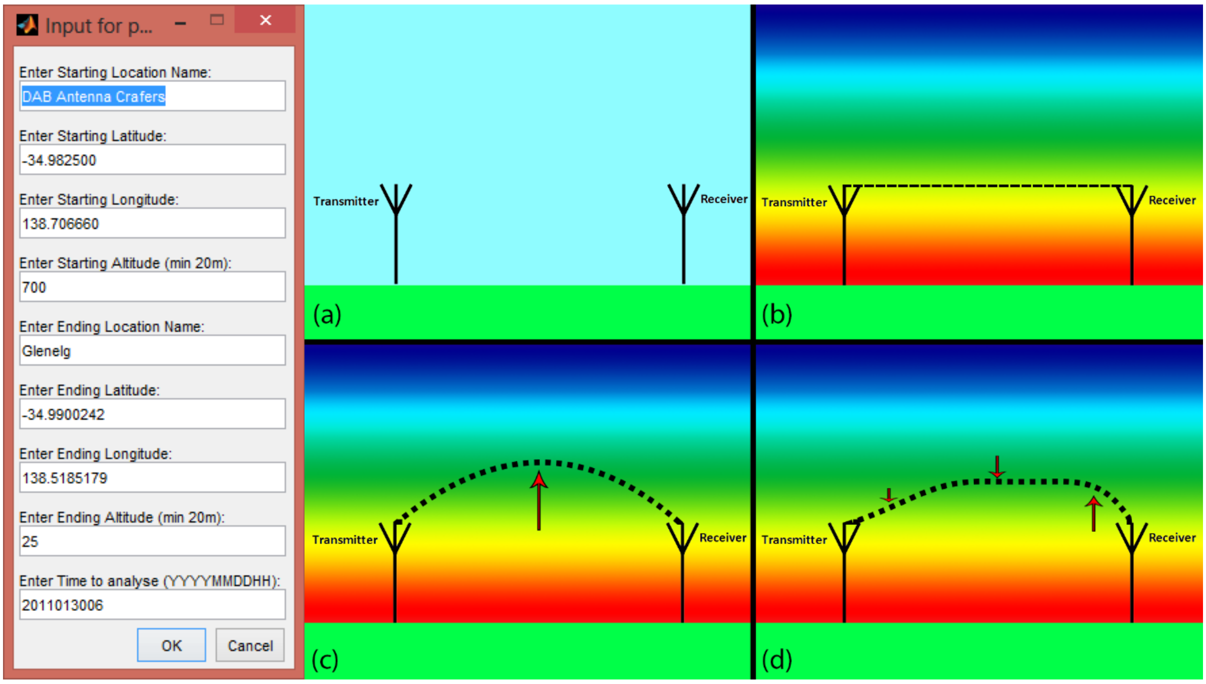

Enter Starting Location Name: DAB Antenna Crafers

Enter Starting Latitude: -34.982500

Enter Starting Longitude: 138.706660

Enter Starting Altitude (min 20m): 700

Enter Ending Location Name: Glenelg

Enter Ending Latitude: -34.9900242

Enter Ending Longitude: 138.5185179

Enter Ending Altitude (min 20m): 25

Enter Time to analyse (YYYYMMDDHH): 2011013006

***Figure 2-4**: Basic process of propagation software (note that propagation path deviations shown are exaggerated. (Left) User provided input. (a) Retrieve data for given input. (b) Straight-line path. (c) First order parabolic estimation. (d) Further refinement of path. The background gradient represents the layered and uniform atmospheric refractive index changing with respect to height.*

The polynomial approximation is only useful in uniform atmospheric conditions and insufficient for more complex environments. However, the above procedure is extremely fast to compute and are done for two reasons: 1) to gauge the atmospheric conditions, and 2) to provide the subsequent numerical optimisation routine with better initial conditions. It is the goal of optimisation routines to find the absolute minimum time of flight between the end points. This is the multi-segment analysis that allows deviations along the ray path to be determined.

This numerical optimisation treats the problem as a time minimisation problem and uses either the local minimum of gradients or pattern searching to find the minimum time of flight between the two points to a specified accuracy level. Once this numerical optimisation has been run, the minimum time of flight, and thus the true path between the two points, will be revealed.

Figure 2-5 illustrates the exaggerated output after numerical optimisation in a non-uniform atmosphere. The end product has taken the three critical points from polynomial approximation and resolved a path based on several hundred segments. This optimised path better reflects the path's deviations due to refractive index changes caused by the varying atmospheric quantities.

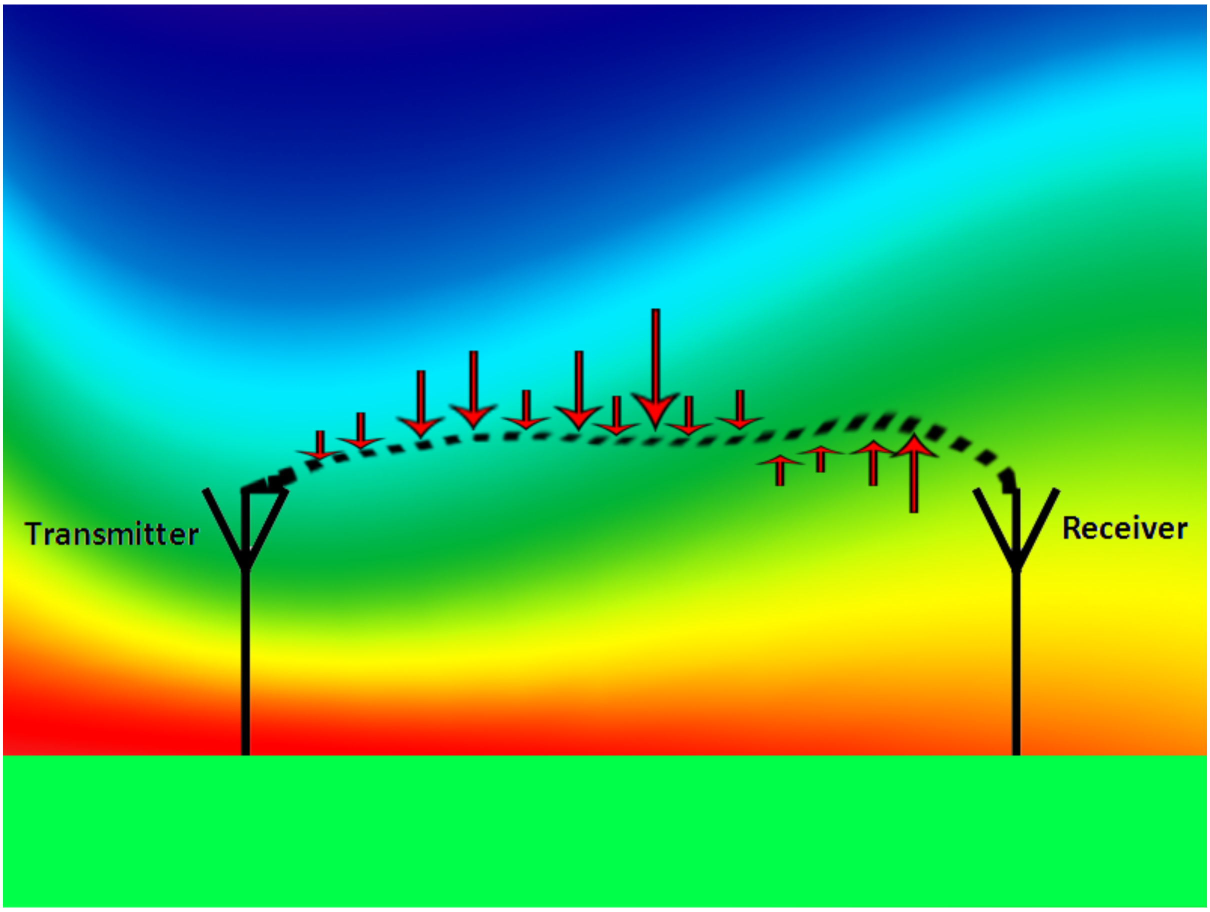

Figure 2-5*: Path deviations after multi-segment optimisation in turbulent atmospheric conditions.*

In Figure 2-6, it shows some typical divergences between path assessments. Even in the calm (and therefore uniform) conditions of the analysed path, there is a height difference of more than half a metre between the linear and actual path. The path in blue is the geometric line, which is then better approximated by the polynomial approximation shown in yellow, and further refined through the optimal path in red. The image illustrates that while a significant improvement is made using polynomial estimation, numerical optimisation is still required to find the true path of propagation.

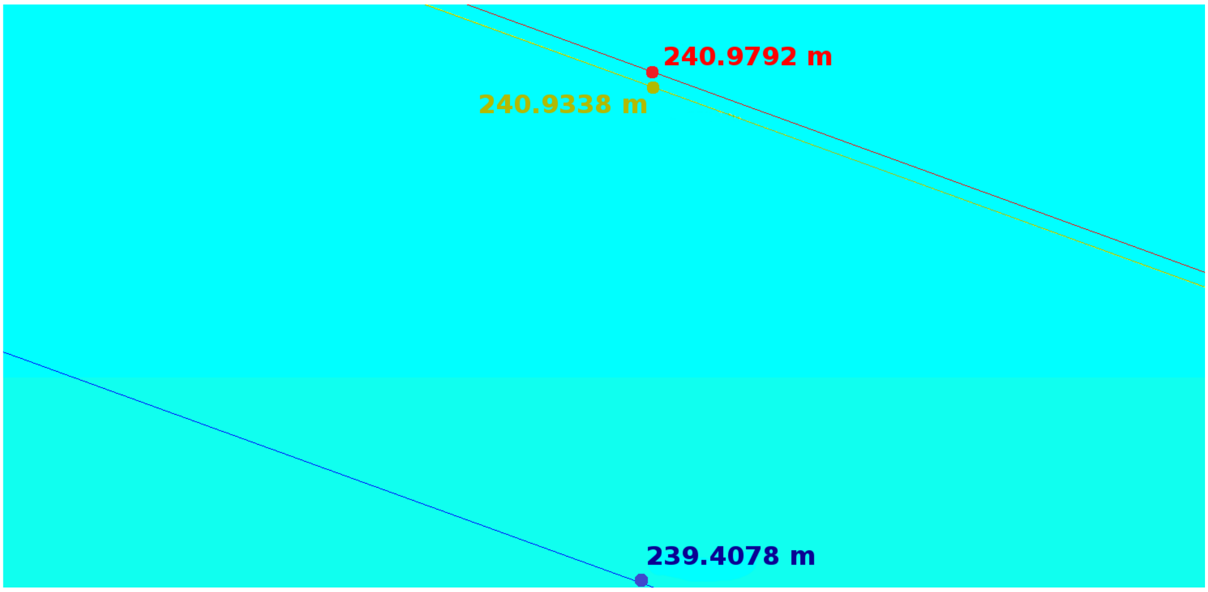

***Figure 2-6**: A zoomed in view of path deviations above terrain for a DAB signal received at Glenelg, South Australia. Blue = Geometric line, Yellow = Quadratic Approximation, Red = Numerically Optimised Result.*

2.5 Validation of Software Results and Computational Characteristics

The software output must be validated so that the user has some measure of confidence in the solution. If the user is to be certain that the path has converged to a reasonable approximation to the exact path, it needs to be shown the resultant path is always the same independent of the starting path. Figure 2-7 demonstrates when random noise is added to the initial conditions of the starting path over three consecutive program executions, the tool produces output paths that always tend towards to the same result.

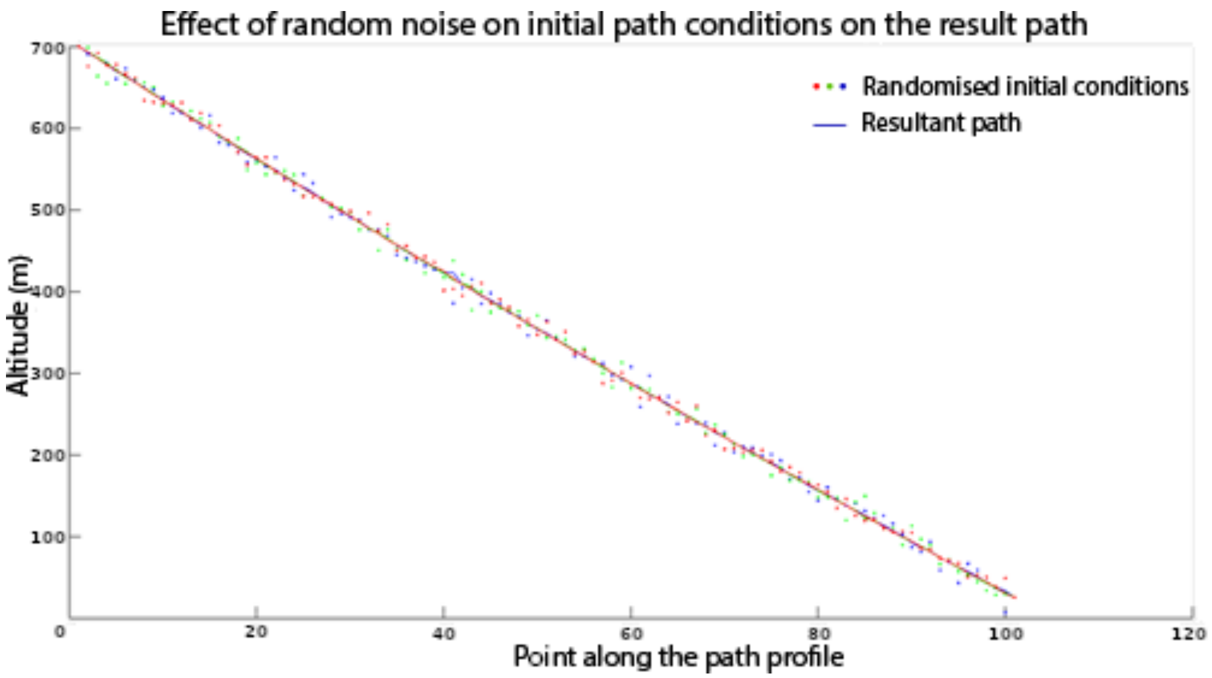

***Figure 2-7**: The software's path output (line) converged to a single solution on the Crafers to Elizabeth scenario, no matter the initial conditions (dotted points).*

Additionally, changing from the local to a global optimisation method found the same path as above, thus provides supporting evidence that the software consistently finds a single basin of attraction. Whilst this demonstrates that the implementation approaches a single answer regardless of its starting position, it is not enough that the solution converges. To verify that the program's path output is a reasonable approximation needs to be independently compared using another approach.

One alternative approach to finding the ray of propagation is to use Snell's Law (equation 2-4) as discussed earlier in the chapter. It was provisionally implemented as a secondary approach with the potential of being fundamentally simpler to implement than Fermat's Principle. With this method, a simulation was run incrementally to find the initial bearing angle of the transmitted ray, at the source antenna with respect to the horizon, which propagated through the atmosphere and found its way to the correct destination (the receiver). In practise though, this method was found to be computationally expensive as each infinitesimally small point along the path had to have a refractive index boundary check for every initial bearing degree analysis.

While the approach of using Snell's Law to uncover the propagation path is not suitable for real time software, it can however, be used to independently validate the solution provided by Fermat's variational approach. Using a simplified layered atmosphere scenario, both methods were compared against each other and Figure 2-8 compares each method.

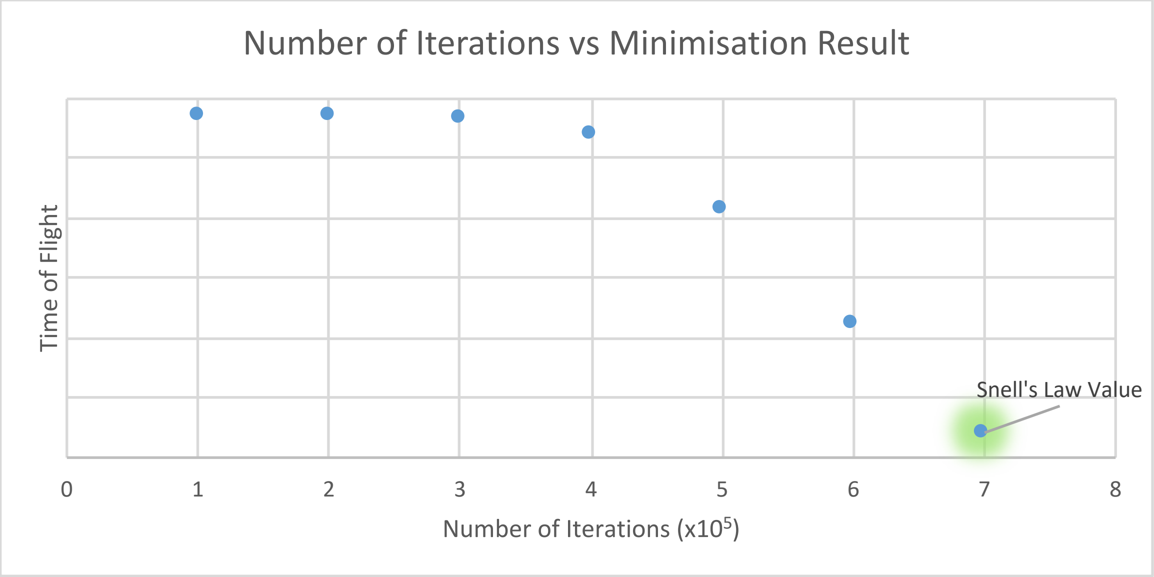

***Figure 2-8**: Comparing Fermat optimisation path implementation to Snell path as a function of iterations shows that after enough iterations (more boundaries considered), the solutions match.*

The speed at which the Fermat approach converges to the solution obtained via Snell's Law (highlighted in green) depends exponentially on the number of optimisation iterations. This was the expected result as Snell's Law is derived from Fermat's Principle of Least Time, therefore it should give the same answer when applied to the same problem. The convergence and validation tests support high confidence in the implementation of Fermat's principle of least time optimisation.

2.6 Computational Considerations

In order to keep the system real time capable, considerations to increase the performance in calculating the true path are required. Simple parallelisation of code enables a four-time speed increase in numerical optimisation routines on a desktop quad core machine. Not all parts of the software can be run in parallel, but for the routines where calculated results are independent of one another, running them in parallel results in a significant speed increase at no cost to the accuracy of the solution. Coordinate transforms are another way to increase speed at no cost of accuracy to the solution. Instead of using complex distance formula for spherical coordinates, it was much faster to convert from spherical coordinates to Cartesian coordinates where the distance formula is straightforward, and then subsequently convert back as appropriate.

Interpolation is required within the software to obtain point values within the given grid points from the data sources. Using trilinear interpolation taking a weighted result of the grid corners is a simple and fast method of 3D interpolation. There are many alternatives to trilinear interpolation that involve additional calculations and operations and thus longer run times. The use of trilinear interpolation is considered justified as the data grid values vary with small changes and these data grid values themselves are derived from of the NWP model and are therefore not true values, and contain their own error. The only faster interpolation method than trilinear is nearest-neighbour, which is not acceptable for this work. Other interpolation methods are discussed in Appendix A.

The nature of numerical optimisation is that the optimal result is found when the difference between iterations is below a certain threshold, typically adjusted within the software with tolerances based on turbulence of the atmosphere. Decreasing this threshold enables answers with higher accuracies but can greatly increase calculation times. Setting a reasonable threshold in the context of this optimisation problem to trade off computation time for accuracy has been chosen by analysing various scenarios and choosing a threshold which increases the accuracy over the initial conditions but is found within a few minutes to keep the software real-time capable. A more in depth look at solving the optimisation problem can be found in Appendix B.

The total time taken for the software tool to finish evaluating a path was measured in absolute time of execution and profiled using debugging tools to investigate areas of the program that require significant processing power. Running on the MATLAB 64-bit environment and using a quad-core processor running at 2.6 GHz, a typical breakdown of execution times was measured and shown in Table 2-1. While run time results are highly variable on the specifications of the computer, Table 2-1 highlights an area which stands out from the rest and could benefit from a speed increase – the optimisation module, and more details on this can be found in Appendix B.

Module	CPU Execution Time (s)	Execution Percentage (%)
Data retrieval	3.136	0.71
Interpolation	64.698	14.7
Path Estimation	54.513	12.4
Optimisation	315.856	71.8
Visualisation	1.725	0.39
TOTAL	**439.928**	**100.0%**

***Table 2-1**: Breakdown of a typical execution of the software running on a quad-core computer.*

It is promising that even regular runs on a modern home or office computer that the software can return useful results within 10 minutes. The software also has the capability of scalability with faster processors or more processor cores. As mentioned, the optimisation module is where the program spends a significant period of time, but the redeeming factor is the independence of each run of the optimisation routine. This independence allows for parallelisation of processing. Therefore, given better hardware such as supercomputers or a cluster of computers, which is generally available to meteorological agencies for real-time processing of data, the computational time decreases while the accuracy of the results increases with available computing power.

2.7 Visualisations

The software has two main components: the propagation path calculations, and visualisation of the atmospheric situation. As the software evolves and gains additional functionality, it needs to be capable of imparting obtained results to the atmospheric scientist, so detailed output is required after each stage that the user can interpret the progress of the simulation. This is accomplished by displaying results to the screen during execution and producing a figure of the simulation upon completion. In runs where the result is all that is needed, such as in a batch process job, the debugging and output capabilities can be disabled to increase simulation speeds and also remove the need for user interaction interruptions. These two components allow the software to be used as both a debugger and a visual interpreter of the current scenario to allow people from various backgrounds to have an intuitive understanding of the work being done.

To fulfil the goal of imparting atmospheric propagation scenarios to users of the program, both the propagation path and atmospheric conditions can be visualised. With a range of output figures available for use (including paths, coordinates, heights), the software automatically interpolates the background atmospheric quantities for the area of interest and plots them (including refractive index, temperature, pressure, and humidity plots). Calculating the background atmospheric quantities is not only done for visualisation, but also to quickly determine if weather fronts occur. To detect this, the software draws an imaginary horizontal line through the atmosphere and calculates the deviations along this line. If significant deviations are detected, then the initial conditions for path optimisation routines are widened and the user has the option of being informed that a front has been detected.

As all of the software has been verified to function correctly and assuming no debugging interruptions occur, the written software then provides a visual output for the user. An example of such is given in Figure 2-9. The visual output primarily includes a profile view of the atmosphere, terrain, and the true propagation path calculated via Fermat's principle. Second, it includes the path across land and data points, as well as the Fermat path versus the straight geometric line between endpoints. Whilst all numeric results are saved separately, the visual output gives an atmospheric scientist several images to contextually appreciate the propagation conditions.

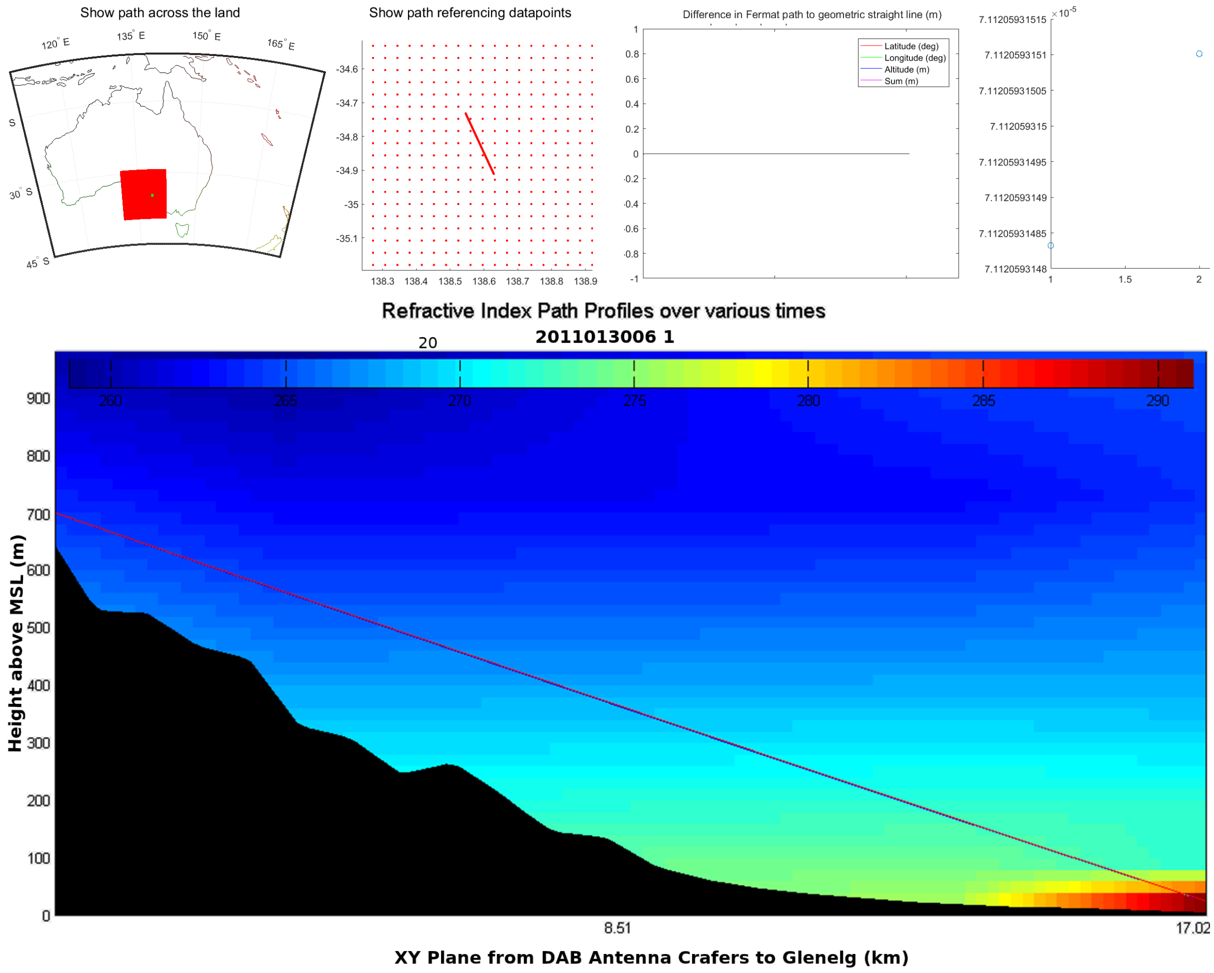

Figure 2-9*: Various examples of the visual output derived from the propagation tool software developed within the project. Images shown only to illustrate breadth of reporting visualisations available. The top row of the figure is along a horizontally scrolling window and thus the display appears truncated here.*

2.8 Propagation Path Summary

This tool has one primary objective, which is to calculate the physical propagation that a radio wave takes between two antennas. It has been developed as part of a larger project whose aim is to determine atmospheric quantities from radio wave propagation timing information. As part of it, it also has several useful features, including:

- Terrain elevation and site logistical analysis for valid radio path determination,
- Completely automated batch processing mode, or easy to use GUI,
- Simple atmospheric front detection,
- Visualisation of weather data surrounding the path, and,

- Visualisation of path deviations from the straight-line.

The implemented method of finding true ray paths via Fermat's principle has been independently verified via Snell's Law. The limiting factor in the propagation tool is tied directly to processing power for interpolation as well as optimisation routines. Whilst exact implementation details have not been divulged for intellectual property reasons, a broad overview of the steps involved have been presented. The completion of this tool and its successful validation permit the next stage of ray propagation analysis beyond simple point-to-point approximations, and further accounts for the atmospheric conditions. This links in to the next stage of the project where the reverse is performed - measuring the time of flight of a radio wave in real time.

3 The Radar Method for Measuring Propagation

This chapter describes the technique that is at the core of the current work, namely the radar method for measuring propagation. This is a powerful technique that overcomes the major problem of traditional techniques identified in previous works, namely the problem associated with timing. The radar technique, however, has its own problems of which direct signal interference is the greatest. The following chapter describes the radar method and investigates the issues that must be overcome to make the approach a reality. Further, the chapter looks at ways around the problems of the method and a designed implementation that can overcome these problems.

3.1 DAB – A Signal of Opportunity

As mentioned in the introductory chapter, Radio Frequency (RF) spectrum allocation is crowded, and it is prohibitively expensive to purchase separate frequencies for use in this research, not to mention the cost in setting up and maintaining private transmitting and receiving stations. Instead, it was worth considering an already existing signal with a strong transmitter. One such signal of opportunity is the national DAB network. The DAB system was developed as a digital replacement for Amplitude Modulation (AM) and Frequency Modulation (FM) broadcasting signals, designed to overcome their susceptibility to multipath fading and interference. DAB has the critical benefit for radar applications of being almost purely random [47], due to its modulation, coding, and interleaving within the signal. Utilising the DAB signal for the required measurements is just one particular implementation of the project's generic technique, but it should be noted that any other signals of opportunity could be used with minor adaptations, where DVB is another example.

For South Australia, there is a sole DAB transmitter located at Crafers in the Adelaide Hills, transmitting on two separate frequencies. This transmitter serves metropolitan Adelaide and its surrounding regions. Figure 3-1 shows the license and estimated coverage areas with an assumed power of 50 kW Effective Radiated Power (ERP) for the transmitter, with both images provided by the Australian Communications and Media Authority (ACMA) [48].

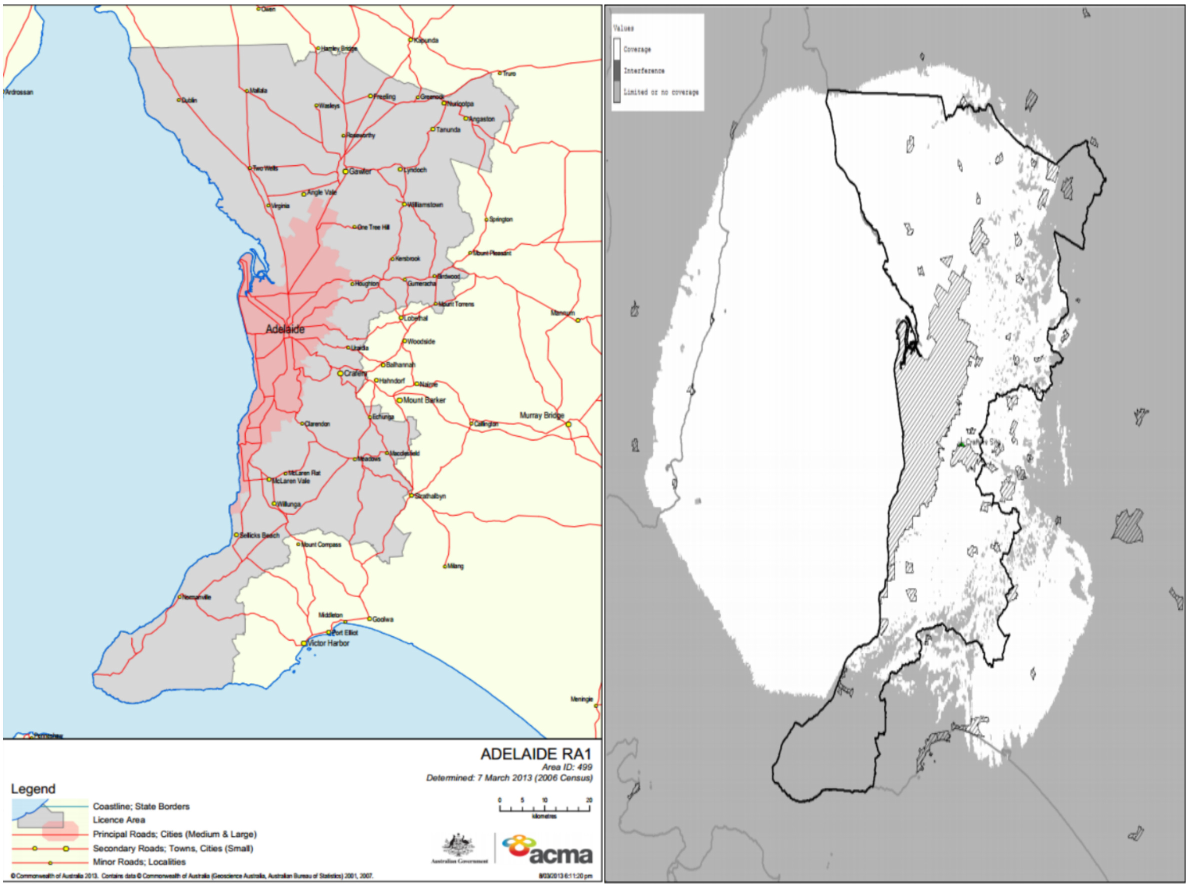

***Figure 3-1**: Digital Audio Broadcasting (DAB) transmission charts from the Australian Communication and Media Authority (ACMA, www.acma.gov.au – accessed on 14 April 2014). (Left) Adelaide DAB transmitter license area, and (right) expected coverage area.*

The outdoor field strengths indicated in Figure 3-1 are estimated using the ITU-R P.1546-1 propagation model. Indoor field strengths are slightly reduced due to the signals having to penetrate building materials. The transmitter is used for both state broadcasts (channel 9B 204.64 MHz), as well as national ABC/SBS broadcasts (channel 9C 206.352 MHz). Unlike the European DAB systems, the Australian DAB system only utilises a single transmitter for each carrier frequency. As a consequence, the proposed experiments do not suffer from the problems of similar experiments with the European systems [49].

Due to the indoors received power of the DAB signal being sometimes too low for adequate reception, the ACMA has a Low Interference Potential Device (LIPD) Class License, which allows DAB signal retransmission in localised areas in order to overcome poor signal strength (specifically inside stores and shopping centres). Whilst such retransmission might be a problem for other broadcast modes, this is not a problem for DAB. DAB has been specifically designed to overcome the problems of multipath and retransmission can be regarded as just another path. Such retransmissions are the basis of the radar method for measuring radio wave propagation and so the use of this method is a benign use of DAB broadcasts. The downside is that the low retransmission power that is allowed for repeated DAB signals (10 µW) [50] [51] is dwarfed by the huge power of the DAB broadcast transmitter. This poses a challenge for the described method, and a scientific license would be required from the ACMA for outdoor retransmission.

3.2 Propagation Measurement Timing Techniques

Measuring the time of flight over a path is not a trivial task and each method involves certain trade-offs. This section evaluates several methods in order to put the chosen method in perspective.

3.2.1 The Problems of Propagation Timing

A possible approach to overcoming timing issues is to use the DAB signal structure. The DAB signal is comprised of frames, with each frame containing the payload as well as a two synchronisation symbols per frame [52]. At first glance, it might seem possible to use these synchronisation symbols to measure the propagation delay. However, to use these synchronisation symbols, the signal must be decoded, which adds complexity to the receiver and a penalty for the real-time objective.

More importantly, however, there is no common reference between the DAB transmitter and the receiver timestamps to provide an accurate absolute time measurement. Even if both clocks were using NTP [53] as the same reference, the drift and jitter of local hardware clock is unpredictable, thus leading to unreliable and unrepeatable delay measurements.

3.2.2 Potential Solutions

A possible solution to the clock timing problem is to use GPS timestamps. Using GPS receivers at each path end, time differences in the order of nanoseconds can be measured [54]. A similar approach was used in UK research [9] where measurements were sufficiently accurate considering the time of flights over terrestrial paths of typically 10-40 km. However, a disadvantage is the added cost of the equipment, asymmetrical signal delays in separate receivers, as well as the remaining (albeit small) absolute timing discrepancies associated with using an external clock reference.

3.2.3 The Radar Method and How It Overcomes Timing Problems

The favoured alternative to these techniques is to use signal correlation at the receiver, in a similar fashion to the measurement of radar returns. In this approach, a signal is measured that that has been reflected from a distant target and one that has travelled directly from the illuminating transmitter. Accuracy is improved due to the relative measurement of both signals in the same receiver and originating from the same transmitter (these are copies of the same original signal). Thus, the clock synchronisations problems are removed. The measurement of time delay is achieved by cross correlating the direct and reflecting signal at the receiver and this can be achieved in one of two ways. In the first approach the receiver has two channels (using the same clock to avoid timing issues) with one receiver designed to primarily receive the direct signal and the other to primarily receive the reflected signal. The two signals are then cross correlated and the time difference can be derived from this cross correlation (further details in Section 5.2). Unfortunately, due to the strength of the direct signal, it is never possible to totally isolate the direct signal from the reflected signal at the receiver. With careful nulling in the antenna system, however, it is possible to remove the reflected signal to a large degree. The residual direct signal, however, can be turned to an advantage and provide a simpler approach to the measurement process. In this approach, called the autocorrelation approach, only the reflection channel of the receiver is used. Since this channel also contains the direct signal to some extent, the autocorrelation will also include the cross correlation and hence provide an estimate of the time difference.

3.2.4 Complications with the Radar Method

This radar approach has its own drawback in that it suffers from DSI. The main concern with DSI is the potential to swamp the receiver with a high powered signal causing the return signal to be below quantisation level of the digital receiver used. Techniques for combating the problem of DSI will be the main concern of the remaining sections of this chapter.

3.3 System Arrangement and Topography Considerations

The experimental setup for the radar approach is similar to that for bistatic radar, and as with bistatic radar, the relative placement of the receiver and transmitter are critical for the successful measurements [14]. In the case of radar, a target is illuminated by one or more transmitters and the signals are returned to a receiver. Cross correlation with a direct signal then produces the time of flight and hence calculates the distance of the target. For the current purposes, the target attributes will be completely known and fixed. This then allows for the changes in time of flight to be deduced, and hence any changes in the propagation medium. The measurement of the relative delay between the direct and reflected signals can be used to avoid the extreme clock accuracy that is required by absolute measurements. However, the power in the reflected signal must be sufficiently large to be detectable against the residual direct signal within the receiver. Achieving this is the main challenge of the current work.

The most basic geometry is shown in Figure 3-2.

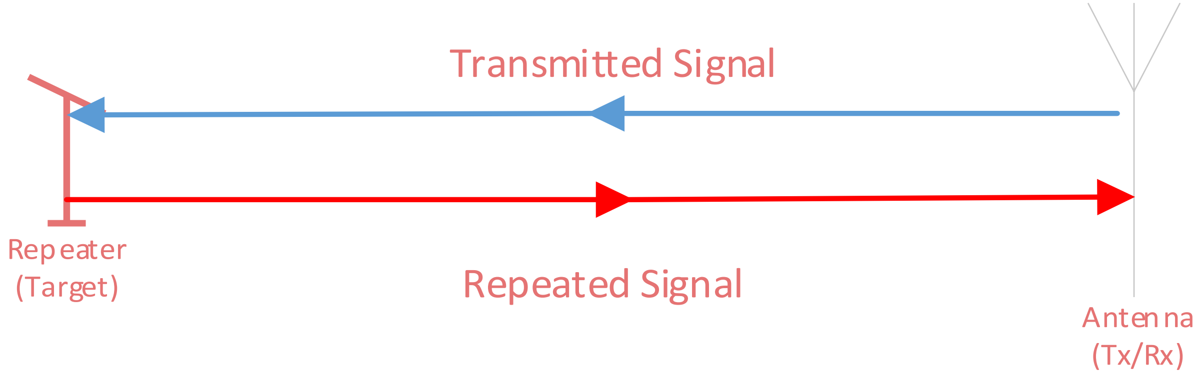

***Figure 3-2**: The most basic transmit and receive timing set up possible to measure a radio wave's time of flight.*

Figure 3-2 shows a collocated transmitter and receiver where a known signal can be transmitted at a known time and its time of return can be measured. Time stamping of transmitted and received signals can be achieved by a single clock and has accuracy as high as the clock itself. This approach requires a cooperative transmitter and allocation of spectrum for the measurement.

The scenario devised for the current research requires a system with a target (the repeater), one illuminator (usually a commercial transmitter of opportunity), and a receiver. The repeater could consist of a single antenna with a duplexer, or two antennas tied together. In the current implementation, a DAB transmitter is used as the illuminator due it its 50 kW ERP and the repeater is made by chaining the receiver and transmitter antennas together (from this point on collectively referred to as the repeater). A receiver is placed as close as practical to the transmitter so that the time of transit for the direct path is as small as possible in comparison with the repeated signal. A simplified diagram of the set up used for experiments is shown in Figure 3-3.

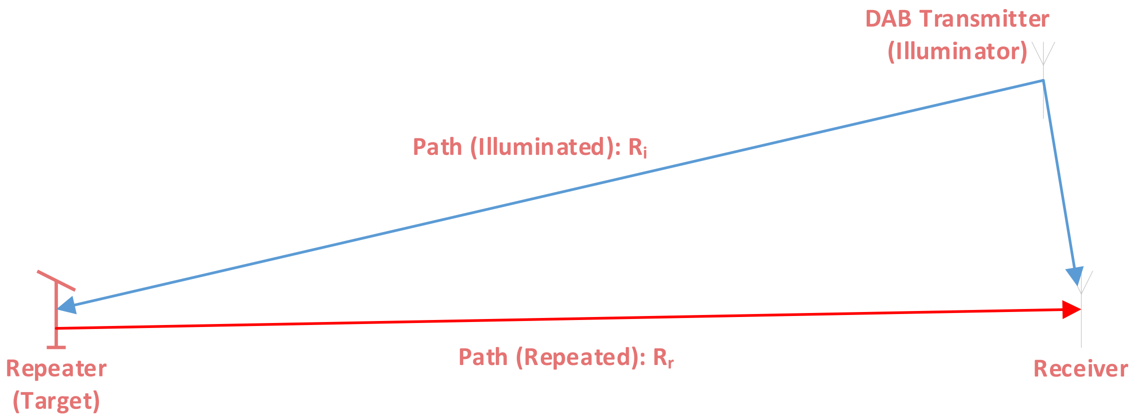

***Figure 3-3**: Basic bistatic radar set up with a single illuminator, target, and receiver.*

As shown in Figure 3-3, there are two signals arriving at the receiver. The first is the direct signal, and the other is the repeated signal. The first (direct) signal arrives at time t_1, and the repeated signal subsequently arrives at time t_2. The difference between the arrival times can be estimated by a cross correlation at the receiver. This delay will consist of a peak in the cross correlation away from the main peak (the cross correlation of the direct signal with itself) and the time can be estimated from the displacement with knowledge of the Analog-to-Digital Converter (ADC) sample rate.

The advantage of the described approach is that it reuses a frequency that is already in use by a high powered transmitter. The limitation in the approach, however, was that the location of the transmitter is fixed. Fortunately, the receiver and repeaters could be moved and set up at temporary sites in order to create optimal configurations for the experiments.

With the architecture of the experiments decided, the best locations within Adelaide's DAB coverage had to be considered. Careful site selection was needed to ensure an unobstructed signal path between the transmitter to repeater path, and from the repeater to receiver. The transmitter to receiver path can be obscured, as additional attenuation on this path can be advantageous. Using the propagation tool mentioned in Chapter 2, a list of potential sites for both the repeater and receiver was drawn up. A primary consideration was for a line of sight from the repeater to both the Crafers transmitter and receiver, allowing sufficient vertical clearance from terrain obstructions so as to not suffer signal deterioration inside of the first Fresnel zone [55]. A secondary consideration was for the receiving antenna to have good gain in the direction of the target and a deep null in the direction of the transmitter. These potential sites were then prioritised according to their suitability for the research and whether these sites were university-owned or owned by external organisations that might benefit from the research. Site accessibility (access control), availability of power, and distance from the Crafers transmitters were top priority determinants when deciding potential sites. Short path distances were problematic as it required the time delay detection system of the two signals to be more stringent. Distant locations were preferred to lessen the effect of this (but not so far away as to be below the horizon) as they would ensure sufficiently measureable time delays of the signals being received and permit faster data processing.

The top sites in Adelaide, South Australia that best matched the outlined criteria were the North Terrace Campus at The University of Adelaide's (UofA) and the Elizabeth Water Tower (EWT) in Elizabeth. Access to rooftops of the buildings within UofA provided swift antenna installation with higher altitude mounts, continuous power, and parallel computing facilities that were suitable for a receiver station. Unfortunately, a repeated signal could not be detected when this site was tested. The receiver site was then replaced with a location on Kings Rd, alongside Parafield Airport. This new site was used as a secondary location for the ideal UofA receiver site. The EWT site provided an elevated level for antennas with a continuous power supply, which was suitable for the repeater.

The final chosen layout for the bistatic radar experiments is shown in Figure 3-4.

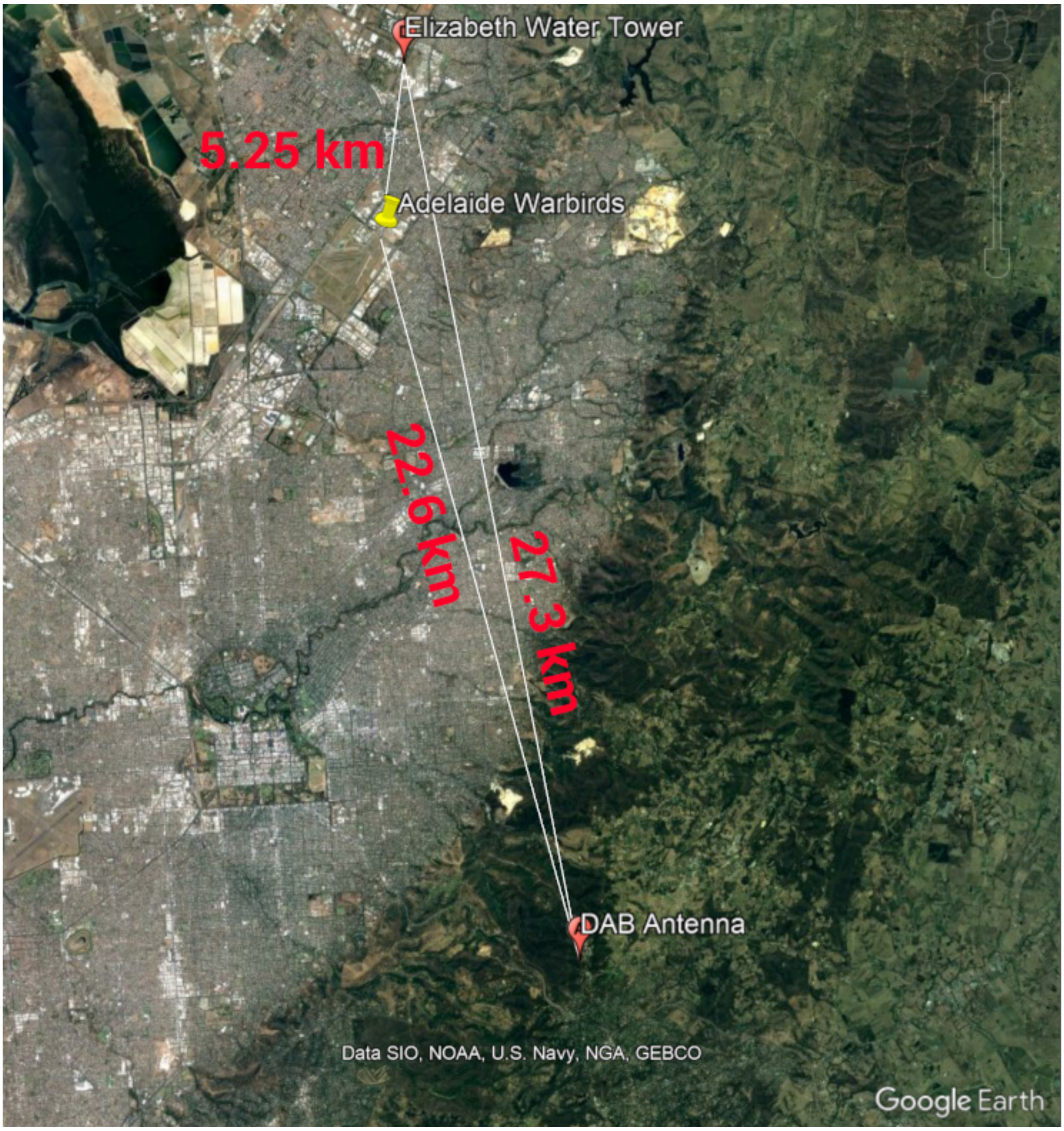

Figure 3-4: *Best possible experimentation paths based on given requirements and restrictions. Digital Audio Broadcasting (DAB) antenna transmitter located in Crafers, repeater at Elizabeth Water Tower in Elizabeth, and receiver alongside Kings Rd, near Parafield Airport.*

The set up chosen closely matches the basic bistatic radar set up with a single illuminator that was outline previously (see Figure 3-3). Whilst the repeater path is angled away from the illuminator path for optimal measurements, meaningful results could still be obtained due to the large distance over which the target is illuminated relative to the minor deviations between the forward and return paths. The arrangement outlined allows for the monitoring of the relative changes of the refractive index over metropolitan Adelaide.

3.4 Direct Signal Interference

To achieve the experiment, two paths are required – the direct path from the transmitter to the receiver, and a second path involving a distant repeater. As explained in the previous section of this chapter, the receiver has to be placed as near as possible to the transmitter so as to record the output signal directly from the transmitter for relative timing purposes. This is because the repeater path signal travels a considerably greater distance in order to enhance the changes in time of flight caused by the changes in refractive index.

Due to the differences in propagation losses, and the fact that the radar cross section of the repeater is quite small, the receiving antenna collects the two different signals from the transmitter at very different magnitudes. This requires the receiver to simultaneously fit two immensely differing signal levels within its dynamic range (further reading available [56]). In the case of passive radar, this problem is often referred to as that of the DSI problem.

To describe the scale of the aforementioned problem, some basic propagation considerations for the Adelaide scenario described are:

Transmitter [57]**:**

Centre Frequency: 204.64 MHz (channel 9B)

Bandwidth: 1.6 MHz

ERP: 50 kW (omnidirectional, vertical polarisation)

Path Distances and Free Space Losses:

For the scenario described in Figure 3-4, the individual path losses using the Free Space Path Loss (FSPL) formula [58] were calculated by equation 3-1.

$$FSPL = (\frac{4\pi d}{\lambda})^2 \qquad 3\text{-}1$$

where d is the distance between two points (m), and,

λ is the wavelength (m).

Figure 3-5 shows how the power falls as a receiver moves away from the transmitter due to FSPL. Note that the complete return path comprises of the distances of both the illuminated path and the repeated path.

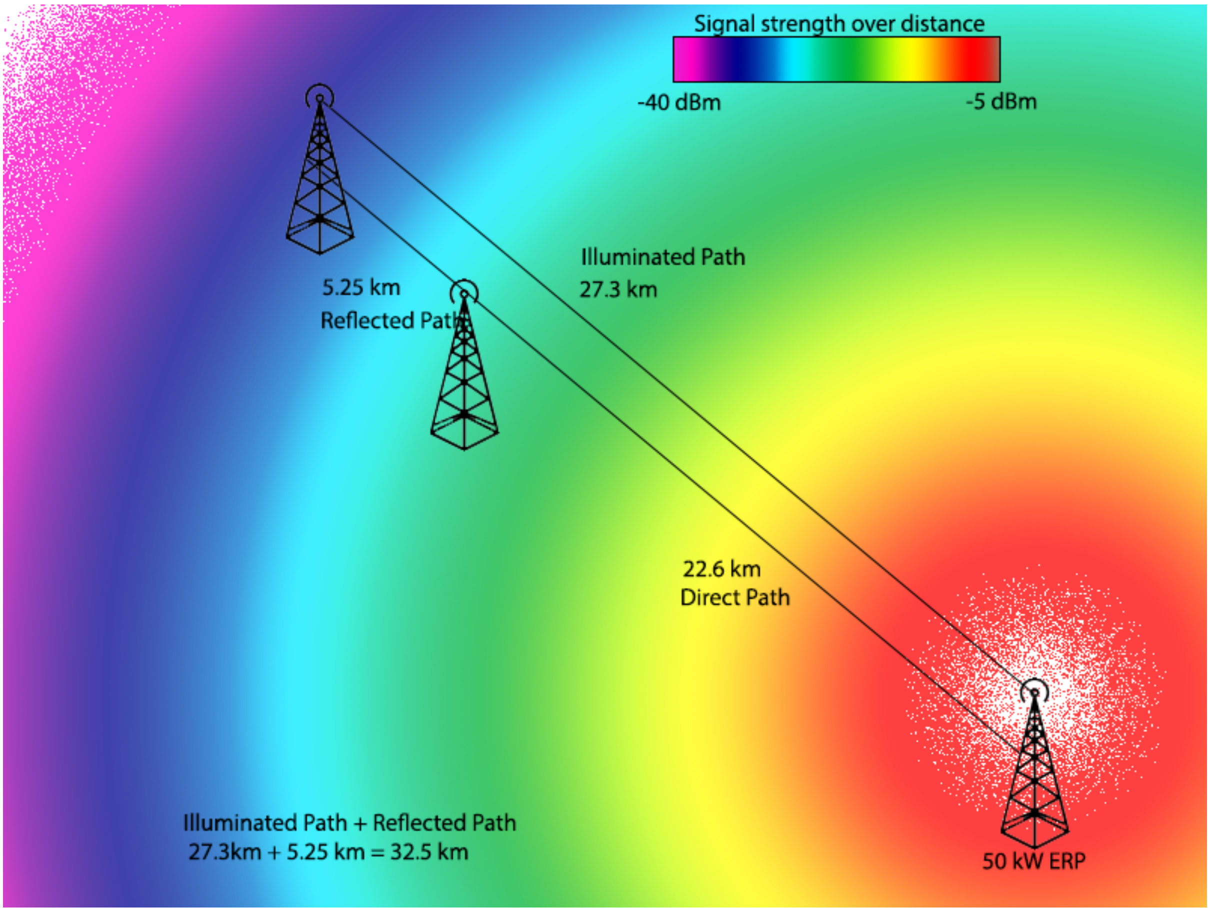

__Figure 3-5__: Signal strength radiating outwards in a sphere decreasing at a rate proportional to the square of the distance from the transmission source.

Using equation 3-1 over each path, estimates of the free space loss were calculated and are shown in the second column in Table 3-1.

The calculation of the received powers the Friis transmission equation [59]:

$$P_r(dBm) = P_t + G_r + G_t + FSPL \qquad 3\text{-}2$$

where P_r *and* P_t are the received and transmitted powers respectively (dBm),

G_r *and* G_t are the gain of the receiver and transmitter respectively (dB),

$FSPL$ is the free space path loss calculated in equation 3-1 in dB.

Using the transmitter specifications of the system presented earlier, and assuming a directed antenna with 5 dB gain, each path is analysed by summing up any transmitter power, gain, and path loss. The repeater path, Elizabeth to receiver, assumes a transmission power that is equal to the power received by the repeater's receiving antenna with no losses. The calculated results have been presented in Table 3-1.

Path	**Distance (km)**	**FSPL (dB)**	**Received Power (dBm)**
Crafers to Elizabeth (Illuminated)	$R_i = 27.3$	$L_i = 107.38$	$P_{r,i} = -30.41$
Crafers to Receiver (Direct)	$R_d = 22.6$	$L_d = 105.75$	$P_{r,d} = -28.76$
Elizabeth to Receiver (Repeated)	$R_r = 5.25$	$L_r = 93.07$	$P_{r,r} = -123.48$

***Table 3-1**: FSPL and received power calculated from the distance and transmitter powers for each stage.*

Therefore, from Table 3-1, the receiver would be expected to accept two input signals of around -28.76 dBm and -123.48 dBm each. That is a dynamic range $DR = \frac{P_{r(max)}}{P_{r(\min)}} = 94.72$ dB in the best-case scenario. In comparison, a typically available 16-bit receiver has a maximum dynamic range of $20 \log 2^{16} = 96\ dB$. Thus, this is inadequate headroom for the expected varying power levels.

Alternatively, the signal strength at the receiver arriving via the repeater can be described with the bistatic radar equation 3-3 [60].

$$P_r = \frac{P_t G_t G_r \lambda^2 \sigma}{(4\pi^3) R_t^2 R_r^2} \qquad \text{3-3}$$

where $\sigma = AG_{rt}G_{rr}\lambda^2/4\pi$ is the radar cross section (m²),

G_{rt} is the gain of the repeater transmit antenna,

G_{rr} is the gain of the repeater receive antenna,

A is the gain of an amplifier between the antennas of the repeater.

Now the dynamic range requirement expressed as a function of only the path distances and radar cross sections:

$$DR \geq 4\pi R_i^2 R_r^2 / \sigma R_d^2 \tag{3-4}$$

This suggests that a cross section greater than 4 m^2 target will be required for a 16-bit receiver. If the cross section is too small, it will be impossible to detect the repeated signal when the direct signal is present. The direct signal will be rounded into quantisation error due to a lack of dynamic range. This is the problem caused as a result of direct signal interference.

For general applications, consumer products prefer strong signals as a method to raise the Signal to Noise Radio (SNR). However, this research requires simultaneously reading in two signals of very different power levels, and so to avoid swamping the receiver, the direct signal must be reduced (recall it is treated as interference [49]) and the repeated signal amplified, which subsequently raises the target cross section. These matters will be discussed in the following sections.

3.5 Techniques to Reduce Dynamic Range

The simplest method to reduce the dynamic range is to reduce the strength of the direct signal. If the topography will allow it, it could be possible to situate the receiving antennas behind hills or other obstructions, so as to permanently dampen the direct signal received.

Another simple way to reduce the dynamic range is to switch polarisation at the repeater (also commonly known as cross polarisation) [61]. This then requires switching of the receiving antenna’s polarisation. This will physically alter the orientation of the receiving antenna such that it is opposite or mismatched to the transmitting antenna. As the transmitting DAB antenna is polarised vertically, this would mean that the receiving antenna would need to be horizontally polarised. If a transmitter and receiver are both set up to be vertically polarised, then maximum power transfer occurs. However, if the transmitter and receiver are not aligned, they suffer a polarisation mismatch, and the received signal level is diminished by the polarisation loss factor $PLF = \cos^2\theta$ where θ is the angle between the polarisations. By exploiting this polarisation mismatch in practice, a complete mismatch is unobtainable but a further reduction of up to 20 dB in dynamic range is realistic [62] [63]. It should be noted that the repeater can no longer be a single antenna with a duplexer, but instead will need to consist of two antennas with opposite linear polarisations tied together.

A third approach to reduce the dynamic range is by amplifying the signal within the repeater. This can be achieved by placing a linear amplifier between the antennas of the target repeater. A high performance bandpass filter will need to precede the amplifier in order to prevent any undesired signal being repeated in the process. However, this adds the requirement of a power supply (either mains or battery) at the repeater, and care must be taken not to overstep the ACMA's specified power levels. The dynamic range is then reduced by an amount equal to the gain of the amplifier. The use of an amplifier can introduce the problem of instability due to the feedback between the receive and transmit antennas of the beacon. It should be noted, however, that the use of cross polarisation helps to reduce the feedback between the repeater antennas. This problem can be further reduced by placing the antennas in each other's nulls and placing the antennas a sufficient distance apart.

The most sophisticated method for reducing DSI is through analogue beam steering. This requires an array of antennas which is steered by varying the phase and amplitude of RF signals arriving at the receiver from the various array elements. Beamforming is primarily used to steer the main lobe (maximum antenna sensitivity) towards the wanted signals, while steering nulls (dips in antenna sensitivity) towards the unwanted interference [64]. Beamforming through a phased array allows an adaptive approach where the beams are adjusted in situ to match the time changes in the environment. If the direction of the signal is known, which is the case in the current application, then the beamforming will be set once during calibration and only minor adjustments are needed throughout the experiment.

3.6 Dynamic Range Reduction Solution

This section details the approach chosen to combat DSI in this research and focuses on the system aspects whilst the hardware details are described in Chapter 4.

DAB transmitted radio waves are vertically polarised and so the repeater has been implemented to receive in vertical polarisation whilst retransmitting in horizontal polarisation. As a consequence, the receiving antenna is set to horizontal polarisation and is therefore cross polarised with the DAB transmitter antenna. The results of experiments into the effectiveness of polarisation mismatch is outlined in Appendix C.

It was found, on average, that an approximate reduction of 10 dB in received signal could be achieved with two Log Periodic Dipole Array (LPDA) antennas directly facing each other but being oppositely polarised. Reflections were mainly responsible for the inability to achieve a higher degree of isolation [62] [63]. The experiments, however, were specifically designed to mimic the conditions at the location where the receive antenna was installed.

The repeater adds an amplifier into the chain to reduce the dynamic range by increasing the power level of the repeated signal. At the repeater, two helical band pass filters each attached to 20 dB amplifiers are placed between the transmitting and receiving antennas. This provides a net boost of +40 dB to the repeated signal, but only in the frequency bandwidth used by the DAB (the specifications of the amplifier and filter quantities, including power requirements and roll off, are described in Chapter 4).

The methods listed are combined and used in the system to combat DSI. The simple solutions, antenna polarisation and amplification at the repeater, are used to reduce the differences in received signals of the direct and repeated path down from 94.72 dB to 70 dB. Consequently, both signals fit quite easily in the 16-bit receiver's dynamic range of 96 dB. The proposed future work (see Section 8.1) involves an adaptive antenna array to provide additional reduction in the dynamic range and to ensure that the system has even better SNR performance.

3.7 Topography and DSI Summary

This chapter has described the radar method for measuring propagation delay. This technique is based on the ideas of passive bistatic radar, a radar system that uses a transmitter of opportunity. This chapter has also investigated the requirements of a system that implements this technique and has identified DSI as a major problem to be overcome. Various methods for reducing the problem of DSI have been discussed and a suitable experimental system has been designed. The hardware implementation of the techniques discussed here are described further in Chapter 4.

4 Receiver Architecture

This chapter details all the hardware used in the experimental set up with concise reasoning behind component selection. Complete component specifications are left to datasheets when off the shelf components are used.

4.1 High Level System Overview

The receiving system of the experimental set up is depicted as blocks shown in Figure 4-1. This system's purpose is to process two separate signals, the direct and indirect signal path transmissions, permitting detection of both.

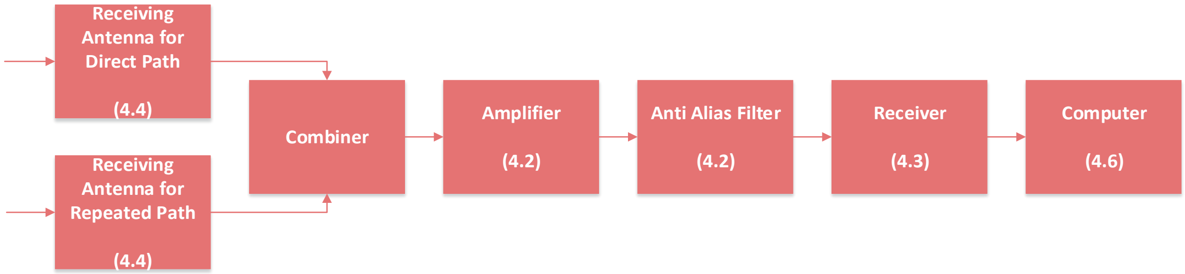

***Figure 4-1**: Diagrammatic overview of the receiving system blocks.*

The blocks shown in Figure 4-2 show the set-up of the repeater (also known as the target). The purpose of this system is to retransmit a signal and provide some gain for easier detection in the receiving system shown in Figure 4-1.

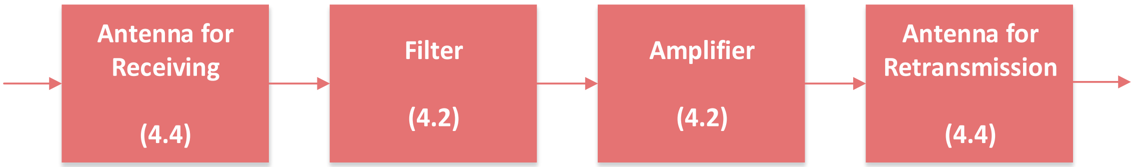

***Figure 4-2**: Diagrammatic overview of the repeater.*

Simulations of all receiving components were done in a MATLAB environment to ensure components were performing as expected along every step of the way. Atmospheric propagation effects including path losses and delays were modelled deterministically on ideal theoretical expectations.

4.2 Amplifiers and Filters

Low noise amplifiers (LNA) need to increase the power of the signal without adding excessive noise or misrepresenting the input. A filter’s function is to allow a specific bandwidth of frequencies to pass through while rejecting undesired frequencies. The practice of combining an amplifier and filter together is useful in increasing the amplitude of only the desired range of frequencies. In the first system, the repeater, an amplifier and filter combination is required to transmit through an antenna only the DAB signal bandwidth to comply with Australian spectrum regulations [65]. In the second system, the receiver, two of these devices are put in series together and used as an anti-aliasing filter with the subsampling ADC. With these basic amplifier and filter qualities, inexpensive but linear devices were anticipated. Both systems employ the same in house designed boards shown in Figure 4-3.

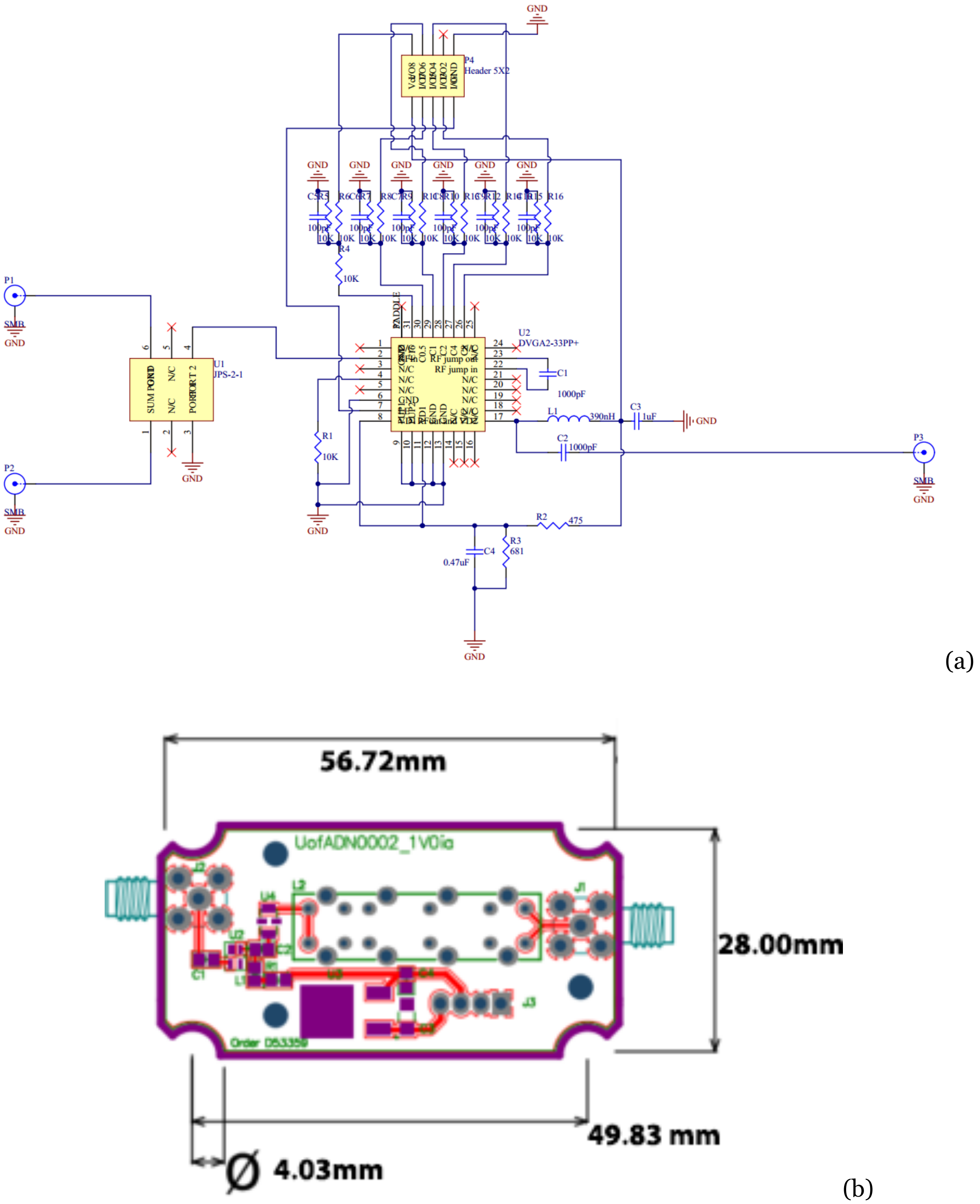

Figure 4-3: Custom filter and amplification board used in both repeater and receiver systems. (a) Schematic and (b) Board footprint.

The amplifiers used are Gali 74 and Gali 84 monolithic amplifier [66] [67]. The typical gain is given as 25 dB for DC-1 GHz with a noise figure of 2.7 dB. The filter used is the TF8929B1-201M helical filter [68]. The centre frequency is adjustable from 196-220 MHz with a -3 dB bandwidth of 5 MHz. Insertion loss is specified as 4.5 dB. The devices were soldered together on a single Printed Circuit Board (PCB), taking in a signal via SubMiniature version A (SMA) connector, first filtering then amplifying, and outputting into another SMA connector.

Characterisation of the device's performance is repeatable and similar across all units. The actual performance of each device was measured by using a Rohde & Schwarz ZVL network analyser and the graph of the output is shown in Figure 4-4. Noticeably, the interaction between the filter and amplifier reducing the specified gain in the passband.

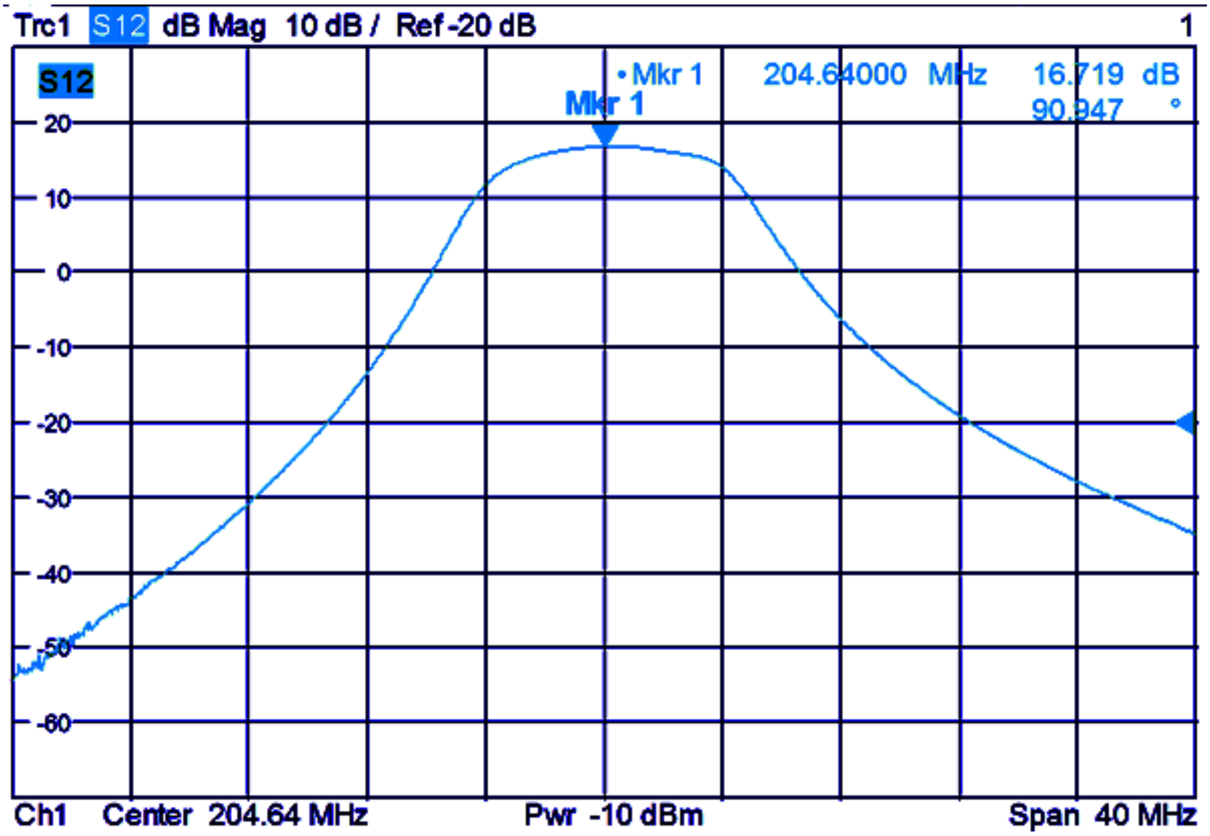

***Figure 4-4**: Transmitted power vs frequency of the Gali 74 amplifier and the Temwell helical filters at the DAB centre frequency.*

The filter has its centre frequency tuned for the DAB frequency in Adelaide of 204.64 MHz (channel 9B) as represented by Marker 1. At this point, the amplifier provides 16.7 dB gain. The cut-off frequencies measured by the 3 dB half power point are between 201.14 MHz on the lower cut-off to 208.64 MHz on the upper cut-off giving a 3 dB bandwidth of 7.5 MHz. The passband here intentionally additionally permits frequency block 9C (206.352 MHz) to be received, which is used as a national DAB broadcast channel. 1.6 MHz (strictly 1.536 MHz) of bandwidth is allocated to each DAB channel, meaning that the lowest frequency component of the required channels of 203.84 MHz and the highest 207.152 MHz are all ideally linearly amplified and all other channels rejected.

Actual performance of the three complete device chains (2x on the receiver, 1x on the repeater) are shown in Figure 4-5. This was measured using the same Rohde & Schwarz ZVL network analyser, and at the exact power as expected in the field, the output gain across 20 MHz was measured. Both receiver chain channels 1 and 2 consist of two helical filters, a Gali-74 amplifier, and a Field Effect Transistor (FET) amplifier. The FET amplifiers are placed at the end of the chain to minimise the Noise Figure (NF). As can be seen in the illustrated frequency responses, each board outputs are very similar to one another. The repeater chain consists of one of the helical filters, a Gail-74 amplifier, and a Gali-84 amplifier. This chain avoids using noisy FET amplifiers, and thus, achieves a high gain whilst maintaining acceptable input power levels specified in the amplifier datasheets [66] [67].

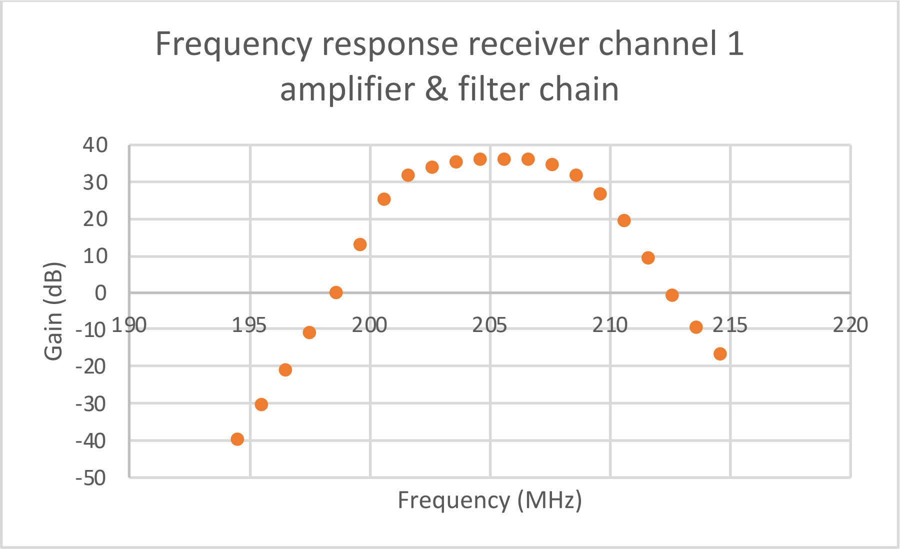

(a)

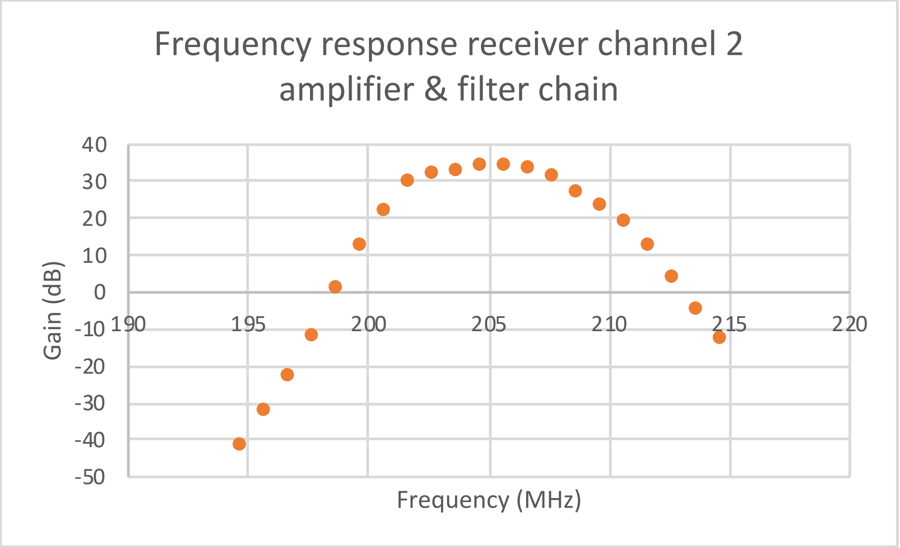

(b)

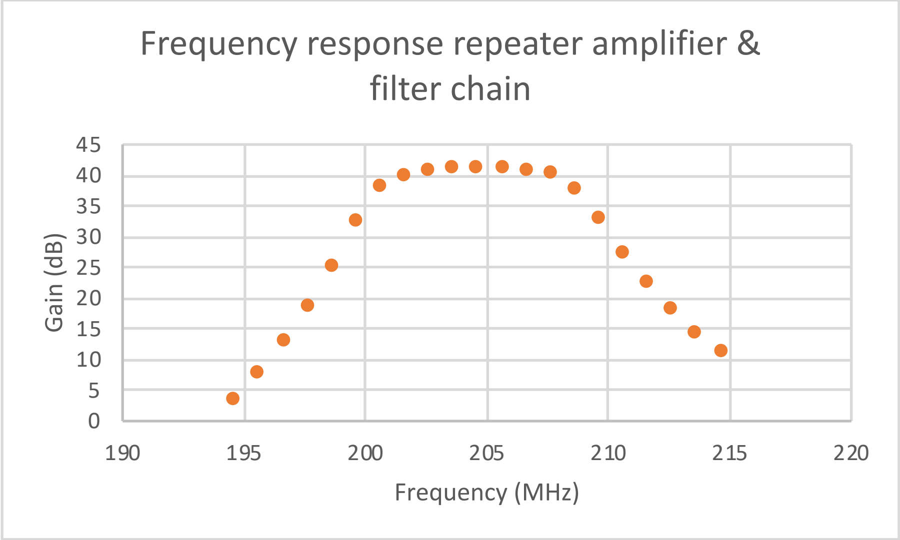

(c)

Figure 4-5*: The measured of the tuned frequency response for amplifier and filter chains used at (a,b) receiver and (c) repeaters.*

4.3 Analogue to Digital Converter

Taking the real world analogue signals and analysing them on a computer was made possible by an ADC. The frequency of the signal this research uses is centred around 204.64 MHz, with 205.44 MHz being the highest frequency component, which would require an expensive and fast ADC capable of sampling at 410.88 Million Samples Per Second (MSPS) in order to satisfy the Nyquist-Shannon sampling theorem's [69] minimum required sampling rate.

An alternative to such expensive high speed ADC sampling is to use subsampling (also known as undersampling). A limited bandwidth signal at high frequency can be reconstructed provided the signal is sampled at a Nyquist rate that is consistent with signal bandwidth. Subsampling takes a copy of the desired signal and shifts it to an intermediate frequency (IF), also known as a signal alias. This method captures not only the desired signal, but also whatever other signals are present at the aliases. To remove this interference, the frequencies outside of the desired range are filtered out in the analogue domain. This is one the purposes of the filters described in Section 4.2. As only the desired signal frequencies are allowed to pass through the system, when it comes to the subsampling aliases, the IF only contains the desired signal moved down in frequency. Further information about this technique is described in [70].

The resolution of the ADC needs to be as high as possible to capture the two signals at vastly different power levels (both the direct and repeated signals). A higher bit depth or resolution allows an analogue value to be more closely mapped (quantised) to a unique digital value and avoids the problem of two distinct signal levels being allocated the same value in the digital domain. The higher bit depth gives a greater dynamic range (DR) between the minimum and maximum signal levels that the receiver detects. This is important as the direct path signal usually peaks at a much higher quantisation level than the repeated path signal. For these reasons, a high resolution ADC is desirable.

Typical ADCs have bit depths of 8, 14, or 16 bits. A 16-bit ADC has $65536 = (2^{16})$ different quantisation levels, or 96 dB of dynamic range. There are techniques such as dithering [71] that can be used to improve the performance of the ADC beyond their specified bit depth.

The chosen ADC capable of subsampling is the LTC2207 [72], sampling at 105 MSPS and at a 16-bit resolution with optional dithering. Integrating the ADC and Personal Computer (PC) together is an XEM3010 [73] Field-Programmable Gate Array (FPGA) via the use of a Universal Serial Bus (USB) 2.0 connection.

The LTC2207's sample rate of 105 MSPS has a direct effect on available experimentation paths. If the experimental path were too short, the signals arriving at the ADC would arrive at very similar times. The ADC would be unable to discern below a certain time and inadvertently merge the two different signals into a single sample. Conversely, if the paths were too long, the signals arriving at the ADC would not arrive in the same ADC frame, as the ADC does not continuously stream samples. However, 105 MSPS provides an extreme number of samples when the signal of interest only has a bandwidth of 1.536 MHz. The excess samples, however, allow for further filtering in the digital domain and this reduces the number of samples, known as decimation. When considering a likely decimation factor of 64, this reduces the sample rate to 1.5625 MHz. It would still satisfy the Nyquist rate as it processes both I (in-phase) and Q (quadrature) samples. The shift in sample rate changes the length of data (order of ms) for a finite N amount of samples, and consequently the minimum and maximum path lengths. To calculate these upper and lower path length limits for each sampling rate (neglecting inherent component delays), see Table 4-1. Using the constants N_s, the number of samples (2^{18} for FPGA frame over USB2), c, the speed of light, and L_D, a DAB frame length of 96 ms.

Sample Rate (MSPS) F_s	**Sampling Interval (ms)** $T_s = \frac{1}{F_s}$	**Frame Length (s)** $L = N_s \frac{1}{F_s}$	**Min Path Resolution (m)** $d_{min} = cT_s$	**Max Path Distance (km)** $d_{max} = N_s cT_s$	**DAB Frames** $\frac{L}{L_D}$
105.0	0.0095	0.0025	2.86	748	0.0260
1.562	64.0	0.17	192	50,300	1.75

Table 4-1*: Effect of different sample rates on the limits of recorded data.*

The maximum path difference with either of the sample rates is more than enough for a terrestrial link. As the lower sample rate can capture the DAB signal bandwidth of 1.536 MHz without aliasing while maximising the length of DAB transmission (1.75 complete DAB frames), the lower sample rate is sufficient. The disadvantage with using a lower sample rate is the minimum path resolution. A 2.86 metre resolution is substantially better than 191.87 metres for a range cell. Using such intervals in correlation measurements would be pointless, however there is an alternative approach to finding useful information despite such intervals as discussed in Chapter 5.

In the case of cross correlation, two of these ADC units are used, synchronised by a single shared oscillator and design attentions down to the microstrip line length, to provide two channels of data.

It is worth mentioning that RTL Software Defined Radio (RTL-SDR) made popular by the cheap DAB/DVB-T dongles based on the Realtek RTL2832U chip unofficially allow the recording of IQ samples. Capable of complete sampling up to 2.56 MS/s, and even further at 3.2 MS/s at the cost of losing samples over the USB interface, this cheap dongle is an applicable receiver for this research with its inbuilt amplification and filtering prior to sampling. It is not used for primary experimentation in this research for the sole reason that it is only an 8-bit receiver and this would result in the dynamic range restrictions of Chapter 3 to be unattainable. However, it was very useful in verifying other parts of the system and more information about the device can be found in [74].

4.4 Antennas

4.4.1 Repeater Antennas

The repeater antennas are situated as explained previously in Chapter 3, with both at the top of a 40 metre water tower. One is horizontally polarised to transmit to the receiver, and the other is located several windows around on the same level to receive the vertically polarised signal from Crafers. The tower is shown in Figure 4-6.

***Figure 4-6**: Ground view of the 50 metre tower where the repeater antennas are installed. Antennas are positioned on the top floor's windows and are separated by the concrete structure with two windows between them.*

The repeater uses two Polar Model 225 antennas [75]. These are Yagi-Uda antennas built for use at 204.64 MHz. Yagi-Uda antennas have a single driven element along the boom, and use the remaining elements as reflectors and directors to produce a directed broadside beam.

Despite being provided the far-field radiation patterns for the antennas centred at a different frequency (148-174 MHz as per the datasheet), further simulations of the field patterns were performed for the actual antennas used. Using the freely available Numerical Electromagnetic Code version 2 (NEC2) by Gerald Burke in 1981 [76], implemented in a modern software (4nec2) [77], the software uses Methods of Moments (MoM) to calculate radiation patterns [78] [79]. MoM separates the conducting wire elements of an antenna structure into segments on which the currents can be determined. The procedure is known to generate an accurate representation of practical far-field radiation patterns with Green's function [80] , but struggles with near-field interactions. Therefore, without any way of accurately, and more importantly, independently verifiable method of modelling the Yagi-Uda's near field-pattern, it was simpler to mitigate any potential issues by keeping the antennas out of the way of any other potentially interfering materials (including another antenna in the case of the repeater). The near-field region is typically considered 2λ (two wavelengths) which in this case is 2.93 metres. The far-field simulation is shown in Figure 4-7 (note in a Yagi-Uda only one element is active, the rest are isolated parasitic elements).

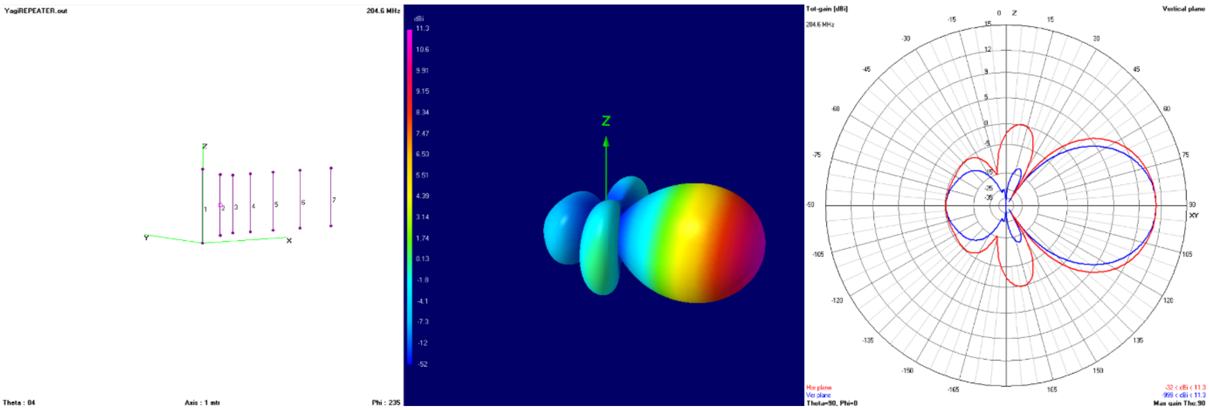

(a) (b) (c)

Figure 4-7: *Numerical Electromagnetics Code (NEC) wire model of 7-element Yagi-Uda antenna. (Left) Physical structure. (Middle) 3D radiation pattern on same axis as wire model. (Right) Azimuth and elevation.*

These antennas have a characteristic impedance of 50 Ω matching the rest of the system, which causes minimal reflected power, thus maximising the transmitted power. A measure of this match is called Voltage Standing Wave Ratio (VSWR) [81]. A VSWR of 1 equates to no mismatch loss (i.e. perfectly impedance matched), and higher VSWR indicates higher mismatch losses. Testing a VHF antenna's VSWR without a specialised environment or anechoic chamber is impossible due to ground wave reflections and other interfering signals outdoors, so adapting the manufacturer's specifications gives the expected VSWR plot shown in Figure 4-8.

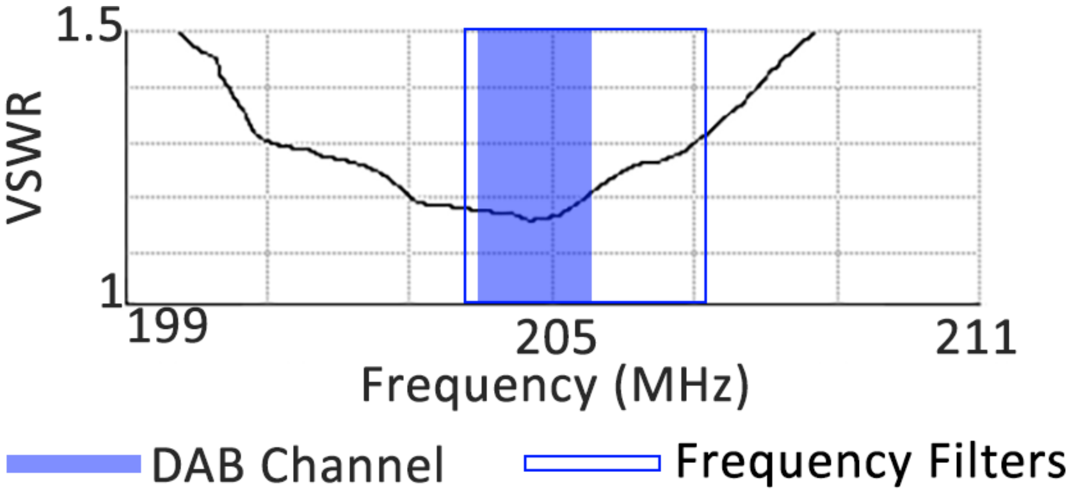

Figure 4-8: Voltage Standing Wave Ratio (VSWR) of both antennas comprising the repeater as a function of operating frequency, with the Adelaide-only DAB channel 9B bandwidth highlighted.

Now the VSWR represents the mismatch from the antenna: $VSWR = \frac{1+|\Gamma|}{1-|\Gamma|}$, where Γ is the reflection coefficient. For a network analyser using s-parameters, it is known as S_{11}. Inverting the equation can obtain the reflection coefficient. The worst case of the VSWR for the chosen antenna is shown in Figure 4-8 to be 1.3 for frequency filtering used. The reflected power coefficient is $RP = \Gamma^2$, since the VSWR is in terms of voltage and it is preferred to work with power. For the VSWR of 1.3, 1.71% power (or a transmission loss of <0.075 dB) is reflected due to impedance mismatch. This is an extremely good VSWR, not requiring any gain compensation amplifiers nor impedance transformers.

Initial drafts of experimental procedures used an 8 metre tower at the same site. The 8 m tower would therefore allow a maximum of 8 m vertical separation between the antennas, which was potentially not sufficient. Antenna separation refers to the physical distance between two nearby antennas and is important to avoid excessive interaction between the electromagnetic near fields of each element's radiation. If the antennas are not sufficiently isolated from each other, they become coupled and can cause feedback loops, oscillations, and even destroy attached amplifiers. Standard repeaters commonly increase the range of propagation of a signal away from its source; that is, it transmits the signal in the opposite direction that it gets received and minimally affect the antenna at its rear. However, the repeater in this project simulates a radar target, and the signal is returned in a similar direction to its arrival. As such, inadequate isolation can also cause desensing of the receiving antenna. The project cannot change the frequency of operation either, therefore increasing the antenna separation and switching polarisation are the only practical means to increase antenna isolation in the repeater system. At a minimum, each antenna should be in the far field of the other so the radiation patterns can be anticipated. At 204.64 MHz, and defining the far-field as 2λ, this puts the minimum separation at 5.86m. Vertical separation provides higher isolation than horizontal separation over the same separation distance for vertically polarised dipole antennas [82]. For this reason, increasing the potential vertical separation of antennas is particularly desired.

Using the graphs derived from experimentation in [82], at 205 MHz it was expected to have at least 50 dB isolation with 8 m separation. While retransmit power is relatively low for a receiver at 200 mW, in order to prevent any issues, the location for repeating antennas was moved to provide the 25 m separation needed for more than 75 dB isolation. A further 20 dB isolation was obtained through cross polarisation of repeating antennas. Further tweaks to position each antenna in the other's null can be done in situ.

Other extreme solutions using expensive echo-cancellation units were considered, but the use of the concrete on the tower was able to provide ample de-coupling between the antennas.

4.4.2 Receiver Antennas

The receiving antenna was set up at Kings Rd alongside Parafield Airport (see Figure 4-9). It was capable of receiving both the repeated horizontal signal from Kettering Rd and the direct signal vertically polarised from Crafers.

Figure 4-9*: The receiving antenna's 3 dB bandwidth (cropped as shown) field of view centred on the repeater direction, located alongside Kings Rd, Parafield, SA.*

This antenna is a Yagi-Uda antenna [83], with a similar design to the ones used at the repeater, but comprises of only three elements, so as to receive signals from a wider direction. See Figure 4-10 for radiation properties of the Yagi-Uda antenna used at the receiving site.

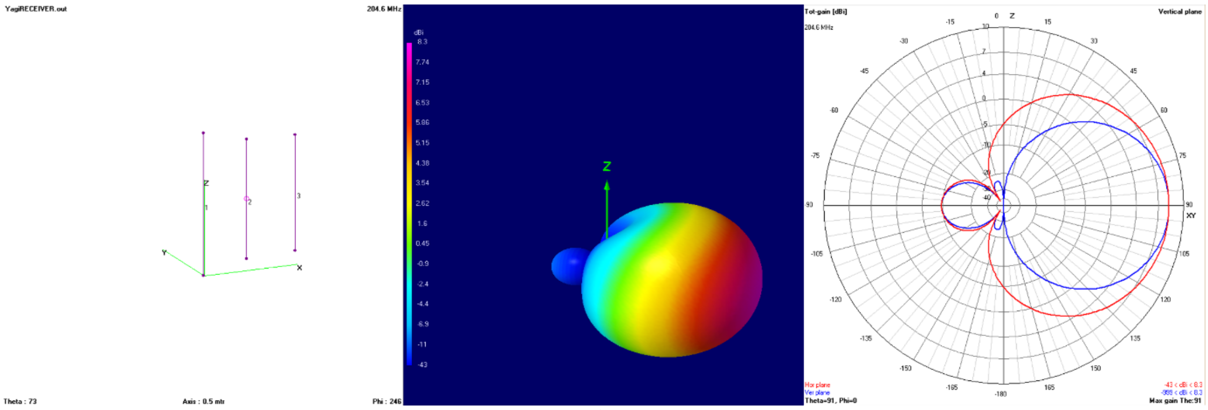

(a) (b) (c)

Figure 4-10*: Numerical Electromagnetics Code (NEC) wire Model of 3-element Yagi-Uda antenna. (a) Physical structure. (b) 3D radiation pattern on same axis as wire model. (c) Azimuth and elevation.*

The receiving antenna was mounted on a wooden tripod, 1 m above the ground.

4.5 RF Cabling

All cabling carrying RF signals were chosen specially for use in high performance radio systems. The vast majority of cabling is LMR-400 [84]; which has characteristic impedance of 50 Ω, low loss of 6 dB per 100 m, and has 85% velocity of propagation. Other minor cabling between components used the more flexible LMR-100.

4.6 Computer

The computer is used to process and record received samples from the ADC (both the 16-bit and the RTL-SDR). The machine runs off a quad-core i5-4300U CPU clocked at 2.9 GHz with 16 GiB addressable memory (8 GiB physical RAM +8 GiB virtual memory). A virtual operating system was created running Windows 8.1 32-bit using MATLAB 2007a for all hardware programming. Received samples recorded to a hard drive controlled by the host machine, and automatically uploaded via secure FTP or a private cloud client.

Readers familiar with computing technology will realise this setup is almost 10 years of age at the time of writing. This is due to 32-bit legacy FPGA code and no developer support for 64-bit systems. There is no essential requirement to have a fast PC for data acquisition. A fast PC is instead required for the other tasks including propagation analysis and subsequent data investigation.

Getting data from this computer in the field requires network connectivity. Mobile data or a wireless hotspot device was required. The ZTE MF90-4G [85] device ran on the Telstra network was chosen for outdoor reliability and coverage. However, using a hotspot device creates a new routing layer, specifically NAT (Network Address Translation) with no access to De-Militarised Zones (DMZ) or port forwarding. This eliminates the possibility of using Microsoft's own Remote Desktop Protocol (RDP). A NAT tunnelling program is required. Licensing costs of popular options including TeamViewer and LogMeIn Hamachi were quite high, but there was a free alternative called Chrome Remote Desktop. While very simplistic and offering no configurable options (such as reducing graphical quality), Chrome Remote Desktop provides a reliable way to remotely transfer recorded data away from the remote machine.

4.7 Deployment Enclosures

The ADC/FPGA was stored in its own metal enclosure. Amplifiers and filters were stored in their own metal enclosures. The primary reason for metal casing instead of plastic casing was to remove external signal interference and avoid potential issues where thinly shielded wires may act as an antenna. The secondary reason for the enclosure was protection from dust with equipment sitting indoors or weather in the case of outdoor use. Holes drilled to allow input and output of the components were sealed with silicon and amalgamating tape to prevent any water damage.

4.8 Hardware Summary

This chapter has described all the hardware used in experimentation. Justifications for each equipment choice have been presented and each piece of hardware has been tested for its intended purposes with performance characteristics of the devices being recorded. Further details of hardware are available in the references and appendices.

The simulations that were run prior to testing the hardware as part of the hardware validation mirror an idealised version of the experiments. Nevertheless, its inclusion into the design stage allowed iterative development of receiver and repeater hardware that would perform as expected. Advanced simulations using probabilistic modelling would be expected to give higher replication of results but due to the results of simulations already matching expectations, probabilistic modelling was not required for the system.

With the hardware designed, built, and assembled, the experiments according to the radar method of Chapter 3 are realisable, with the measurement of the time delay of a radio wave being presented in the following chapters.

5 Signal Delay to Refractivity Introduction

By means of the hardware introduced in the previous chapter, the measurement system records a stream of data. Figure 5-1 shows an example of the spectrum of such data that was recorded at the UofA in October 2016 atop the Schultz roof (at an altitude of 70 m). This data stream captures both the direct signal and the repeated signal, with the latter at a much lower power level than the former. To isolate and reveal the time difference between these two signals, the signal recording needs to be processed based on the DAB signal model.

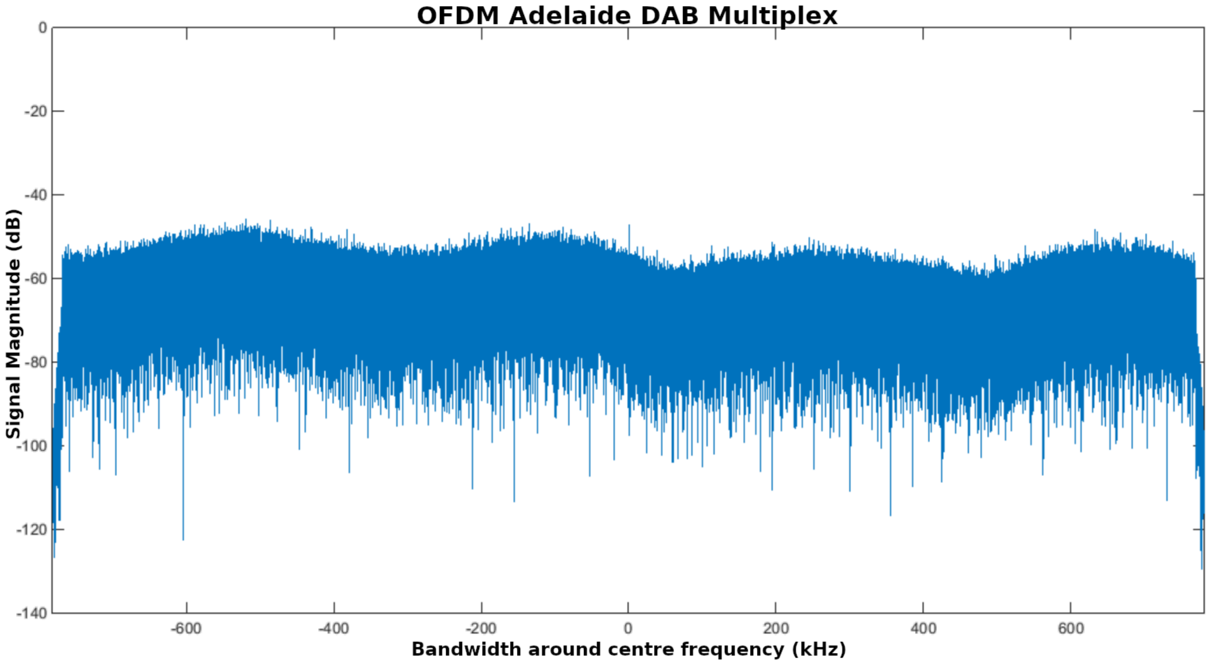

Figure 5-1*: A channel 9B Digital Audio Broadcasting (DAB) received signal recorded atop the Schultz Building, The University of Adelaide, SA.*

5.1 The DAB Signal Model

DAB in Australia uses the updated DAB+ standard. This, in turn, is based on the European standard [86] with a slight modification. Denoted as T-DAB+ for terrestrial applications, the Australian standard [87] uses MPEG-4 High-Efficiency Advanced Audio Coding Version II (HE-AAC v2), instead of the previously used MPEG-1 Audio Layer 2 (MP2) audio codec in the original DAB standard. T-DAB+ in Australia utilises Mode 1 of the ETSI DAB Standards [88] in Band III. Each capital city is allocated a local multiplex channel, with all transmitters also broadcasting a national multiplex. In Adelaide, South Australia, the local multiplex is channel 9B (204.64 MHz).

In terms of the Open Systems Interconnect (OSI) model, the DAB standard operates on three layers (see Figure 5-2): physical layer, data layer, and presentation layer.

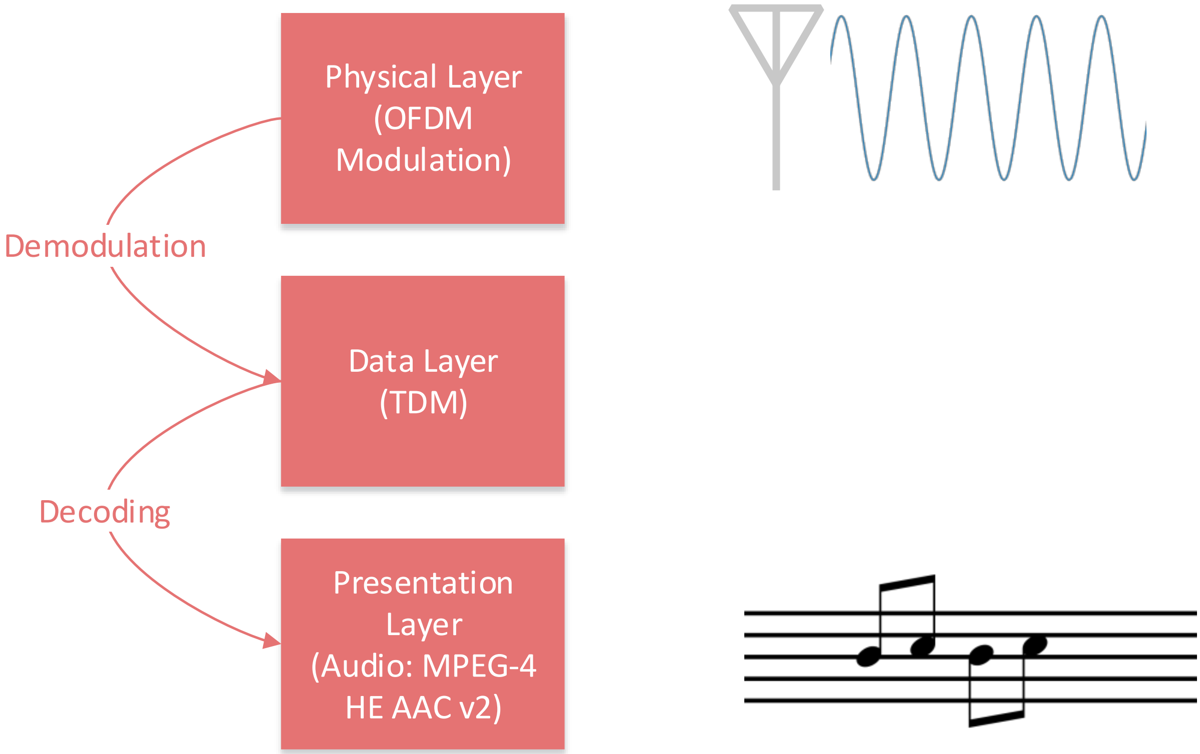

***Figure 5-2**: The three OSI layers defined by Digital Audio Broadcasting (DAB) standards.*

5.1.1 Physical Layer

The physical layer is responsible for carrying data from the transmitter to receiver over radio waves. Orthogonal Frequency-Division Multiplexing (OFDM) is employed to reduce multi-path interference and improve spectral efficiency over the previous FM standard. OFDM uses multiple orthogonal sub-carriers within the allocated spectrum bandwidth. For DAB, 1,536 subcarriers are present spaced by 1 kHz as shown in Figure 5-3. Each sub-carrier can be demodulated independently by taking the Discrete Fourier Transform (DFT) of a 1 ms block.

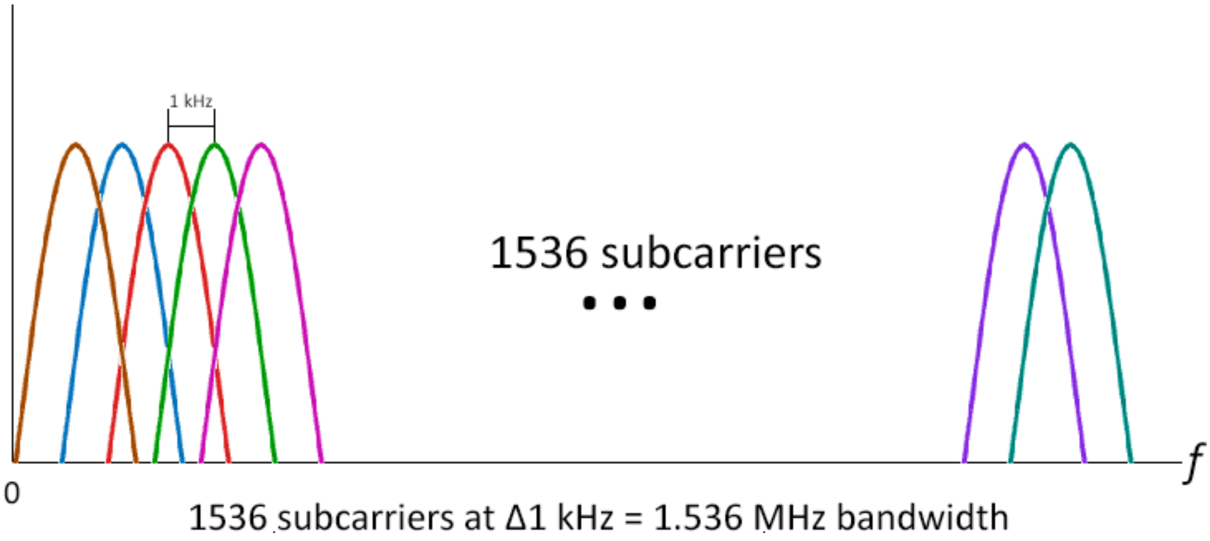

Figure 5-3*: A look at the physical Digital Audio Broadcasting (DAB) transmission in the frequency domain.*

Terrestrial propagation suffers from multipath effects and so, to maintain multipath robustness, a guard band is added in the time domain. This guard band was chosen so that the received signal could handle delayed copies of the same signal without causing any Inter-Symbol Interference (ISI). The DAB+ standards specify a guard band of 246 µs long, which is equivalent to multipath differences of 74 km being acceptable. This guard band is also useful in single frequency networks with multiple transmitters where it prevents nearby transmitters causing interference. This, however, is not relevant in the Australian DAB system.

To uphold orthogonality, and prevent Inter-Carrier Interference (ICI), each OFDM symbol is preceded by an equivalent length cyclic prefix. Each DAB transmission frame is 96 ms long, made up of a synchronisation channel (null and phase reference), Fast Information Channel (FIC, containing Fast Information Blocks about MSC composition), and a time-interleaved Main Service Channel (MSC). Each symbol is of length 1,246 µs. These symbols are generated using Differential Quadrature Phase Shift Keying (D-QPSK) and frequency interleaving. Further information about the Fast Information Channels and other frame composition information is beyond the scope of this writing, but is available in [89].

A representation of the DAB transmission frame (Mode I) in the time domain in shown in Figure 5-4.

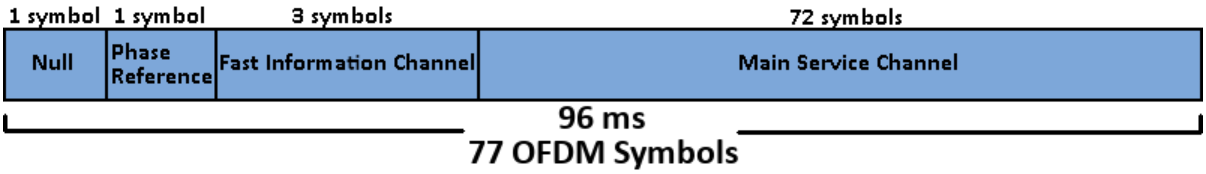

***Figure 5-4**: Time domain representation (not to scale) of a single Digital Audio Broadcasting (DAB) transmission frame*

5.1.2 Data and Presentation Layer

The data layer contains an encoded representation of the DAB payload. While a DAB signal contains small amounts of Programme-Associated Data (PAD), the vast majority of the data represents an audio signal. The data encoding layer is interesting in its own right, however is not relevant to this current research as no demodulation is performed.

5.2 Potential Delay Measurement Approaches

Five algorithms have been considered to uncover the delay of the repeated signal and are outlined individually in the remainder of this section:

5.2.1 Null Symbol Tracking

Between each DAB transmission frame is a null symbol as depicted in Figure 5-5.

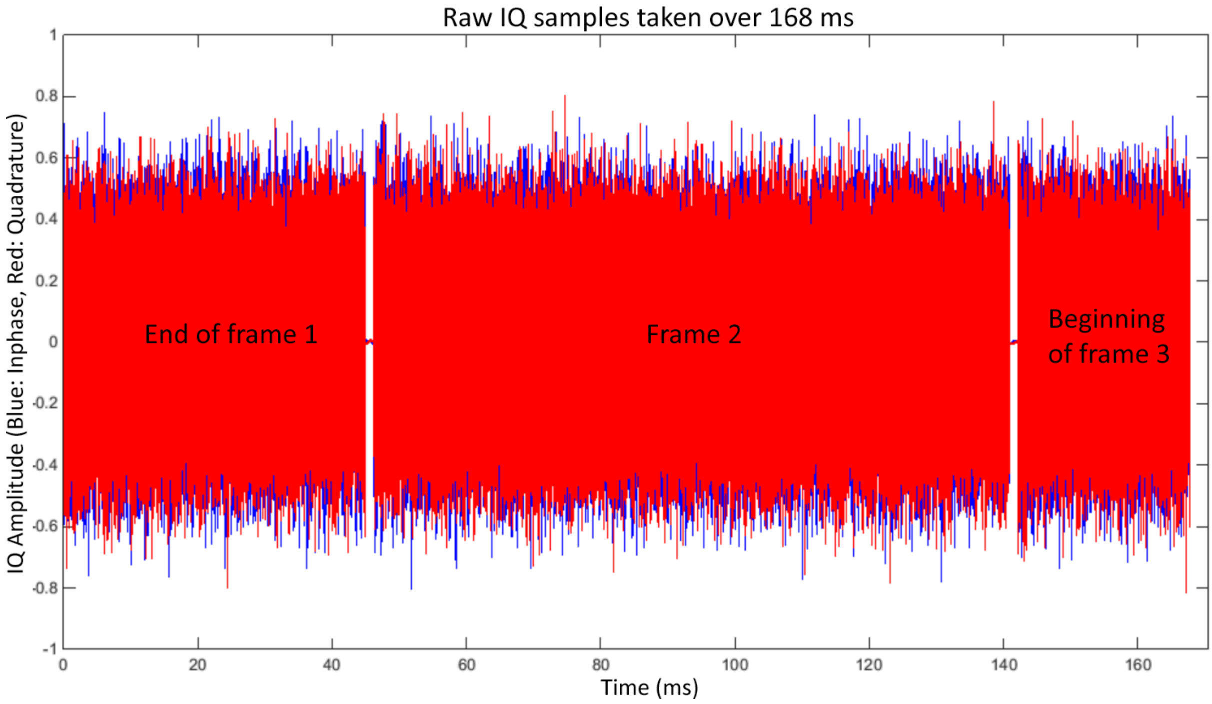

Figure 5-5: Raw Inphase/Quadrature (IQ) samples depicting three partial Digital Audio Broadcasting (DAB) transmission frames separated by two null symbols.

The null symbols are quite clearly seen with a sharp cut-off at ≈45 and ≈141 ms. These null symbols last for exactly 1.297 ms. With an ADC sample rate F_s, the length of a null symbol in samples can be expressed by $\frac{1.297^{-3}}{(1/Fs)}$. Algorithmically, null symbol detection must look at when the sample amplitudes are much lower than the average sample amplitude of the envelope of the signal [90].

When a DAB signal is repeated and the receiver records the data of two signals, where one is delayed, then provided adequate analogue filtering, the detected null symbol's Inphase Quadrature (IQ) length is no longer than $\frac{1.297^{-3}}{(1/Fs)}$. The presence of a repeated signal causes an encroachment of IQ amplitude within the null, and detecting the length of this encroachment reveals the time delay.

This method is straightforward to implement as it uses raw IQ samples to estimate the signal delay. However, it heavily relies on the sharp edge cut-off for a null symbol, and thus impractical for anticipated multipath signals.

5.2.2 Cross Correlation Amplitude

Cross correlation amplitude is the sliding dot product of a discrete signal over a second discrete signal, resulting in amplitude peaks at lags whenever the signal correlation is high. This can be mathematically represented as (Equation 5-1):

$$\sum_{i=-N}^{N} f^*[i]\, g[i+s] \tag{5-1}$$

where f and g are the 2 discrete signals and ($f = g$ for autocorrelation),

N is the number of samples,

s is the sample shift.

Equation 5-1 results in a vector of length $2N - 1$ with real and imaginary components due to the IQ signal. With autocorrelation, two maxima are present, the one at the zero lag, and one at an unknown lag due to the repeater. Normalisation is typically required to properly detect peaks and results in a plot such as in Figure 5-6.

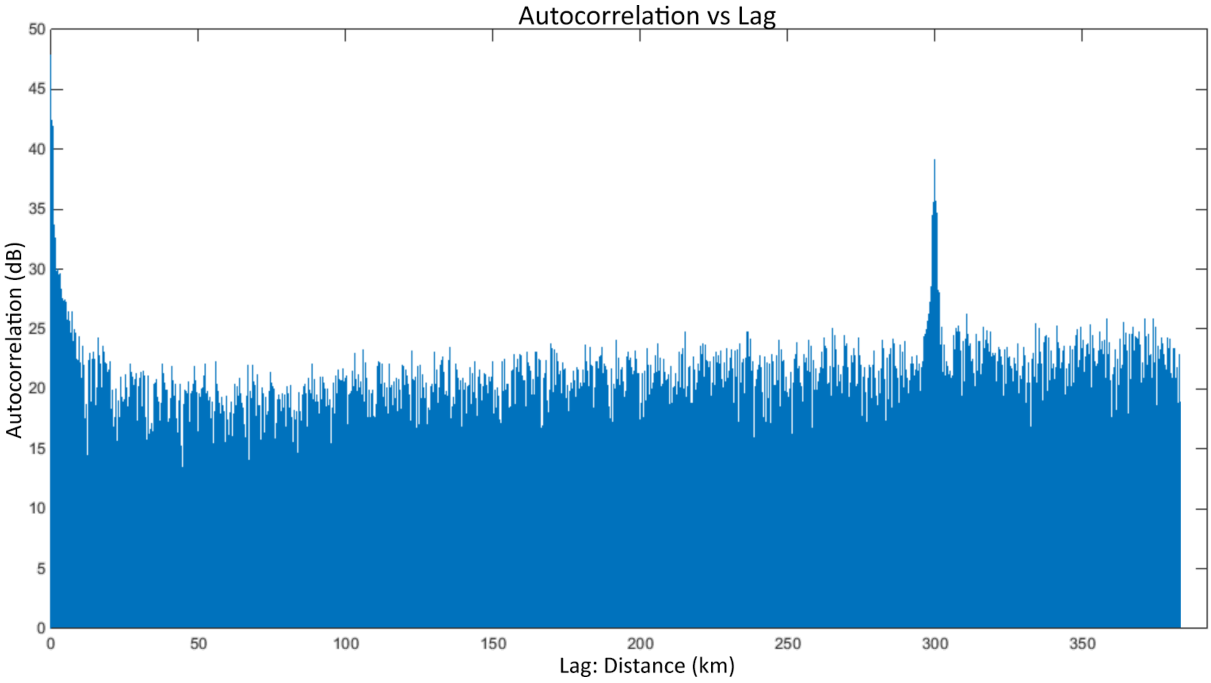

***Figure 5-6**: Autocorrelation result showing a distinct lag (effectively a copy of the signal) around 300 km away.*

This method does not require signal demodulation but is not applicable to short ranges for which a lag can be hidden in the main peak's sidelobes as the time resolution is limited to the sampling period. In analysing the autocorrelation, the method only needs to examine the lags for a few samples around the expected delay of the repeater. The variations due to changes in the refractive index are quite small and there is a danger that it could be mistaken for multipath from repeater returns.

5.2.3 Cross Correlation Phase

The cross correlation amplitude can only determine the delay down to the length of a sampling interval. Consequently, the true peak can be offset from the peak in the discrete autocorrelation by a non-zero amount δt. Fortunately, if the true peak is offset, the phase $\delta\varphi$ of the discrete autocorrelation at the peak will be non-zero and allow estimation of δt. For a simple single DAB subcarrier, the relationship between $\delta\varphi$ and δt is linear i.e. $\delta t = \delta\varphi/\omega$, where ω is the frequency. For a full DAB signal, however, the relationship is quite complex. Fortunately, the subcarriers are orthogonal and this makes the relationship tractable. Let ω_1, ω_2, …, ω_M be the subcarrier frequencies then, at the peak in the discrete autocorrelation, the autocorrelation takes the form

$$A\sum_{i=1}^{M} \exp\left(j\omega_i\,\delta t\right) \qquad \text{5-2}$$

where A is real.

The increment between the subcarrier frequencies will be constant and so the above expression can be summed as a finite length geometric series. From this, it is found that the delay offset can be calculated from the phase by assuming a single frequency that is the average ω_{av} of the subcarrier frequencies. The delay offset can therefore be calculated as $\delta t = \delta\varphi/\omega_{av}$.

5.2.4 Pilot Symbol Tracking

This method requires demodulation of the signal to reveal the phase reference symbol. Within each DAB transmission frame, immediately after the null symbol, is the phase reference symbol. This synchronisation symbol potentially enables dependable phase tracking of the signal. However, demodulation adds extra complexity to the receiving system, and affects any real-time processing concerns.

5.2.5 Phase Comparison Technique

Another possibility was to compare the phases of the direct and repeated signals. This is potentially problematic due to the fact that the DAB signal is broadband and phase will vary across frequencies. With the two receivers, one that receives the direct signal s_1 and the other that receives the repeated signal s_2, the Fourier transform was taken of the sampled signals before comparing their phases. The phase difference between the two signals will depend on frequency since the phase is a product of frequency and time. The phase difference between the signals will be $\omega\delta t$ and δt can be obtained from the phase difference at any frequency. However, a better estimate of δt can be obtained by estimating at all available frequencies and taking the average. This is advantageous, as it will remove much of the noise.

The problem with this approach is that the repeated return will be heavily contaminated by DSI and this will mean that the phase estimates for the repeated signal will be very inaccurate. This approach, however, has the potential to be effective if the DSI can be removed sufficiently.

5.3 Testing the Delay Measurement System

For current purposes, the most practical approaches to delay measurement are provided by the phase comparison and correlation approaches. This section compares the suitability of the two methods.

5.3.1 Phase Comparison Technique

Firstly, to test direct phase comparison for the measurement of delay, simulated conditions of the real experiments are created by inserting a copy of an off air signal with an artificially delayed copy. This was achieved by splitting the received DAB signal from an antenna and introducing an additional cable length into one of the branches combing them at the input to the receiver as can be seen in Figure 5-7. This delay signal simulates the repeater return.

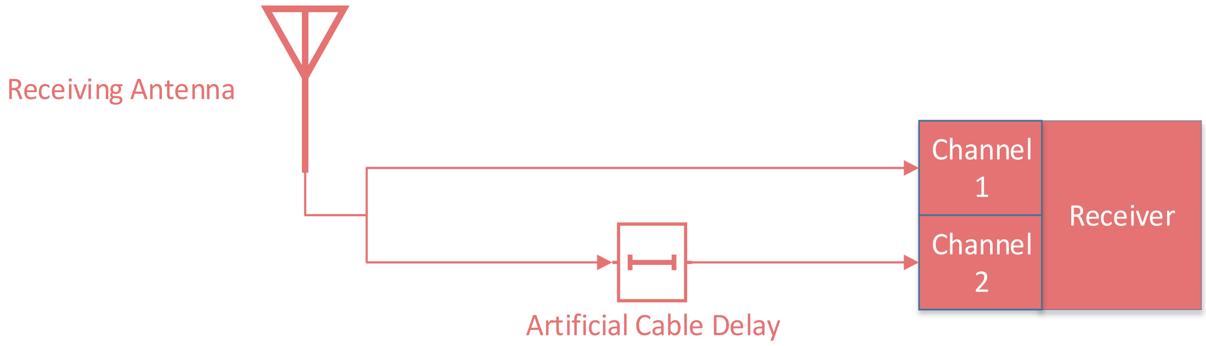

Figure 5-7*: Experimental simulation of propagation delay imitated by an artificial cable delay.*

The signal is angle compared against the delayed copy of itself enabled by the two-channel complex IQ data, and is then unwrapped to remove discontinuities. Given the OFDM signal and 1536 subcarriers, there are 1536 separate components to the phase delay, and thus 1536 1-length Fast Fourier Transform (FFT) bins. This results in lag as a function of the signal's frequency. Applying linear regression through all these components and taking the slope of the line will determine an average absolute delay of the repeated signal across all frequencies.

Examples of two different delays after performing the above processing steps are pictured in Figure 5-8, where there are two artificial delays introduced to the system. The first, in blue, is a 500 m cable with a Velocity Factor (VF) of 82%. The velocity factor is the speed at which the signal propagates through the cable as a percentage of the speed of light in a vacuum. In red, is a 70 m cable with 66% VF. Taking the slopes of these two plots yields 1.97E-06 and 3.08E-7 for blue and red respectively with units of seconds. Quick calculations of the expected delay with known velocity and distance yield identical results to three significant figures, thus validating the phase correlation method.

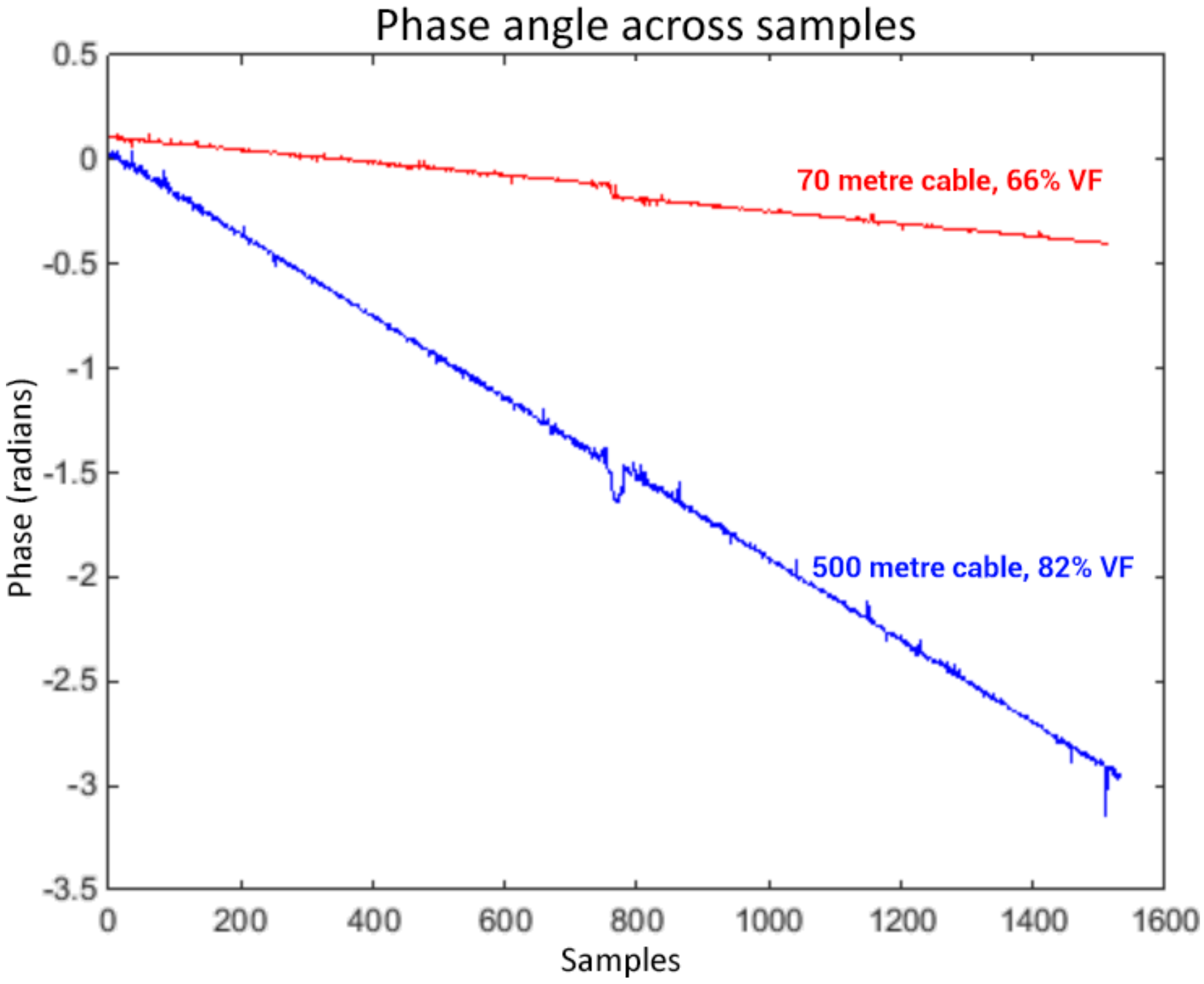

***Figure 5-8**: Phase Angle measurement with two different artificially introduced delays, (blue) a 500 m cable with 82% VF and (red) a shorter 70 m cable with a slower Velocity Factor (VF). The jumps in slope are caused by signal-to-noise ratio (SNR) degradation but have not affected the slope estimations.*

It is worth distinguishing that this method is quite capable of returning expected results despite two signals of highly varying power, however, noise in the signal (due to inadequate frequency filtering or DSI) can affect reading directly from the signal slopes with spurious noise alone the lines. The examples shown in Figure 5-8 are reasonably unblemished due to the artificial delay being implemented after the receiving filters in shielded coaxial cables. However, Figure 5-9 illustrates the aforementioned detrimental effect of noise on phase measurements.

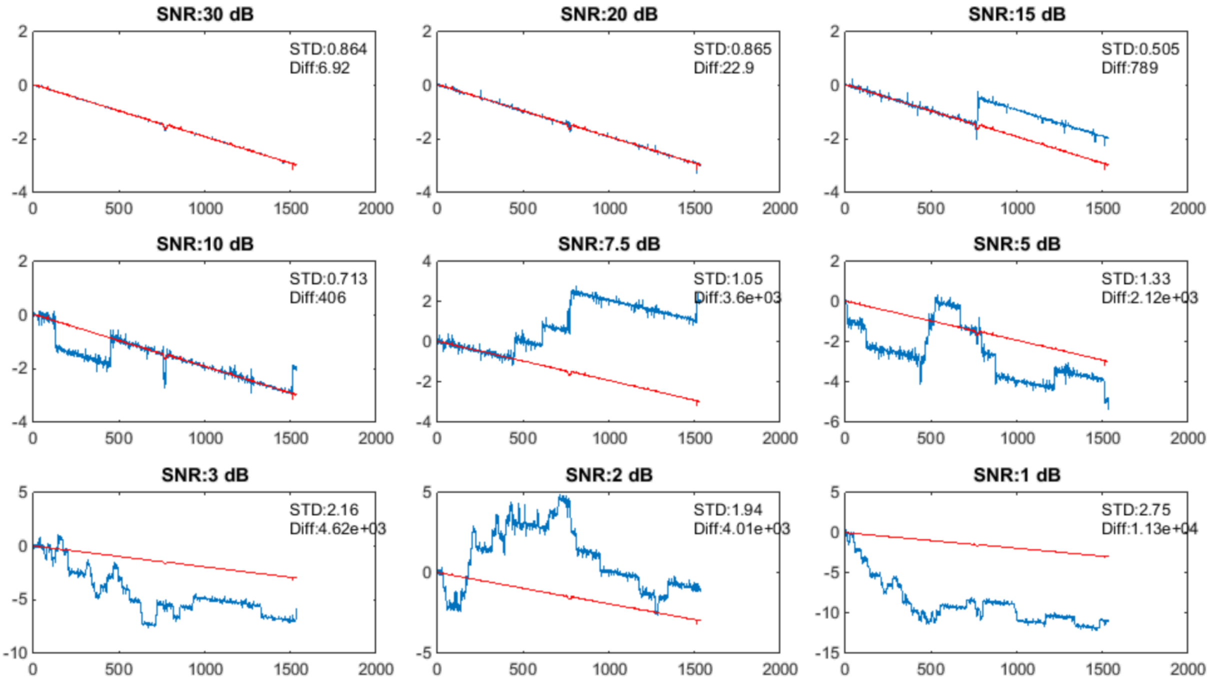

Figure 5-9*: Effect of various Signal-to-noise (SNR) of the received signal on timing measurement showing that as the SNR decreases, the (blue) phase angle makes it more difficult to determine the (red) slope.*

It is important for the approach to retrieve the slope of the lines accurately. The blue line is the angle corresponding to the respective SNR signal, while the red line is the resolved signal slope. As the SNR decreases, so too does the likelihood of retrieval of the slope, and ultimately the delay of the signal. At least 15 dB SNR allows easy computation of the slope, but below 5 dB SNR makes computation highly prone to error.

Phase comparison works to reveal the hidden signal's delay with these clean signals as shown above, but in the current work, DSI severely contaminates the phase of the repeated signal to the point that this technique is insufficient with real-world propagation. Therefore, efforts were concentrated on the correlation approach.

5.3.2 Cross correlation Phase

It is possible to test the phase cross correlation technique independently against the same simulated delay set up as earlier. Phase correlation is a more real-world applicable method as it is resistant to the phase contamination from DSI.

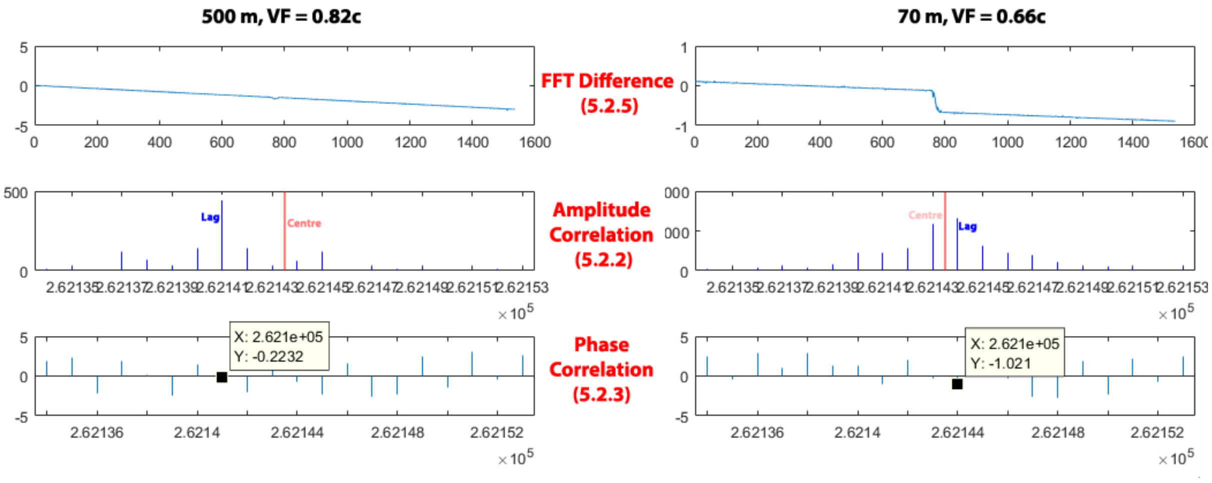

__Figure 5-10__: Using the phase extension of cross correlation as a way to uncover time delay. (Left) Cable length 500 m .82c and (right) 70 m .66c.

The cross correlation displacement of the -3rd and 1st sample bins (corresponding to amplitude correlation peaks in Figure 5-10) are obtained for the 500 m and 70 m cables respectively, with corresponding phase displacements of -0.2232 and -1.021. Given that the centre frequency for the DAB channel is 204.64 MHz, the time offsets resolve to be -4.6E-8 and -2.12E-7 s respectively. Adding these offsets to the sample bin lags of the cross correlation gives 1.99E-6 and 4.3E-7 seconds, which is in agreement with the results obtained via FFT phase comparison technique.

Of interest, the peak heights Figure 5-10 are of great importance to the method, and it demonstrates the reason for why DSI needs to be minimised to maintain visible main peaks above any other superfluous peaks in the cross correlation.

5.4 Converting Time Delay to Refractivity

From the repeater time delay t, it was possible to calculate the average refractive index over a path. Assuming the medium to be non-dispersive, the average speed for propagation c was calculated from the expression $v = \frac{c}{t}$, where distance in velocity is the distance that the signal has travelled. To a first approximation this is the geometric distance, but a slightly improved estimate was achievable using the methods described in Chapter 2. The tool used previously known atmospheric information to determine an estimate of the true distance travelled instead of the geometric distance. Once an estimate for the speed of propagation was obtained, the refractive index will be given by $N = \frac{c_0}{c}$, where $c_0$is the speed of light in a vacuum.

It should be noted that the actual measurement of the system was the difference between the time delay for the direct and repeated paths. As a consequence, the time delay needed to be adjusted for the delay of the direct signal. In addition, there was a systematic delay in the repeater equipment (cables, amplifiers, filters, etc.), but this could be calibrated out of the measurement. The measured delay in the repeater electronics was observed to be 250 ns at 204.64 MHz, measured by means of an Agilent 8714ET RF Network Analyser.

5.5 Time Delay Calculation Summary

This chapter has presented several approaches to finding the timing delay information from recorded data. Each method listed has its own advantages and disadvantages, but a few have strengths suited for this research using real propagation environments. The limitations of several methods stem from additional hardware complexities – ADC sample rate in the case of raw IQ delay and amplitude correlation, and demodulation of the signal for phase symbol tracking. Comparing the phase angle is a discriminating approach only useful in a controlled environment due to any hint of DSI knocking out phase at the receiver. The most robust method of obtaining the timing delay between two signals lies in the phase offset of the amplitude correlation. This method was favoured for being robust and relatively capable in disregarding the effects of DSI. Furthermore, it was independently compared to the alternative methods and has been found to produce the expected results and was the method of choice going forward.

6 Results

This chapter displays the findings using all the previous chapters' justifications, equipment, and techniques. Firstly, an overview of system procedure is presented and later the experimental results are shown.

6.1 Procedure

Figure 6-1 shows a high-level overview of the methodology in performing each experiment.

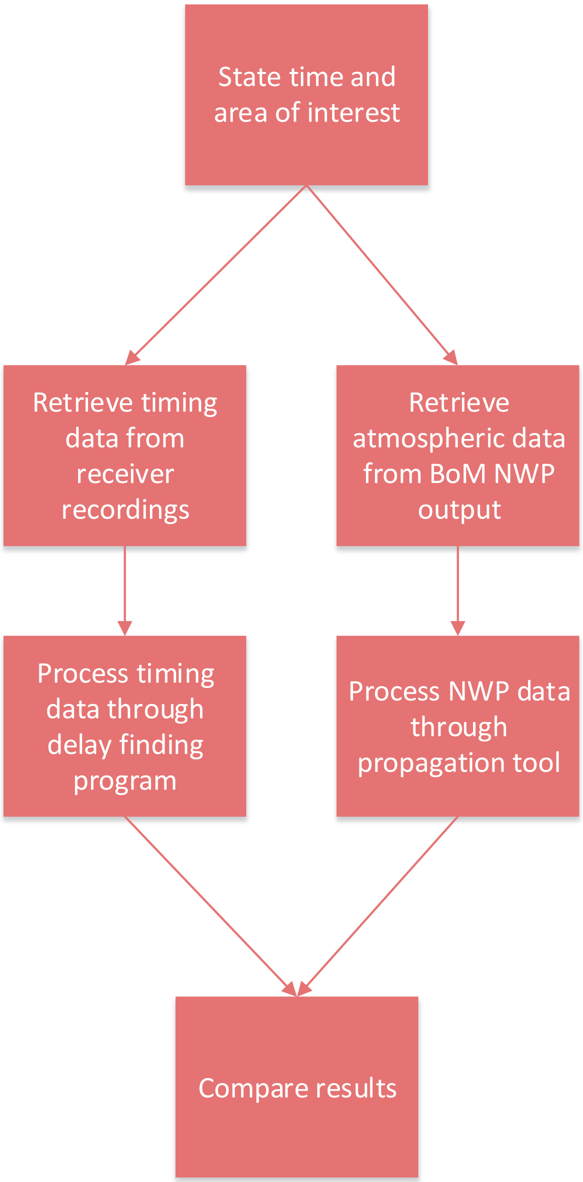

Figure 6-1: *High level overview of methodology for performing the each experiment.*

Further details of the procedure can be located in Appendix D.

The remainder of this chapter will deal with the major step of processing results in order to see what useable information can be obtained from the timing measurements.

6.2 Preliminary Results

A trial of the experimental procedure was run on the 27-28th October 2016 using a USB powered ADC in an RTL-SDR [74] receiver. The device has 7 ENOB (Effective Number Of Bits) which is approximately 42 dB of available dynamic range. The receiver was set at a location outside of Parafield Airport on Kings Rd (Figure 3-4). A 5-second recording was made every hour, for 24 hours, and repeated 3 times for consistency. Figure 6-2 shows the typical autocorrelation (window limited to the autocorrelation peak and first lag) for each recording.

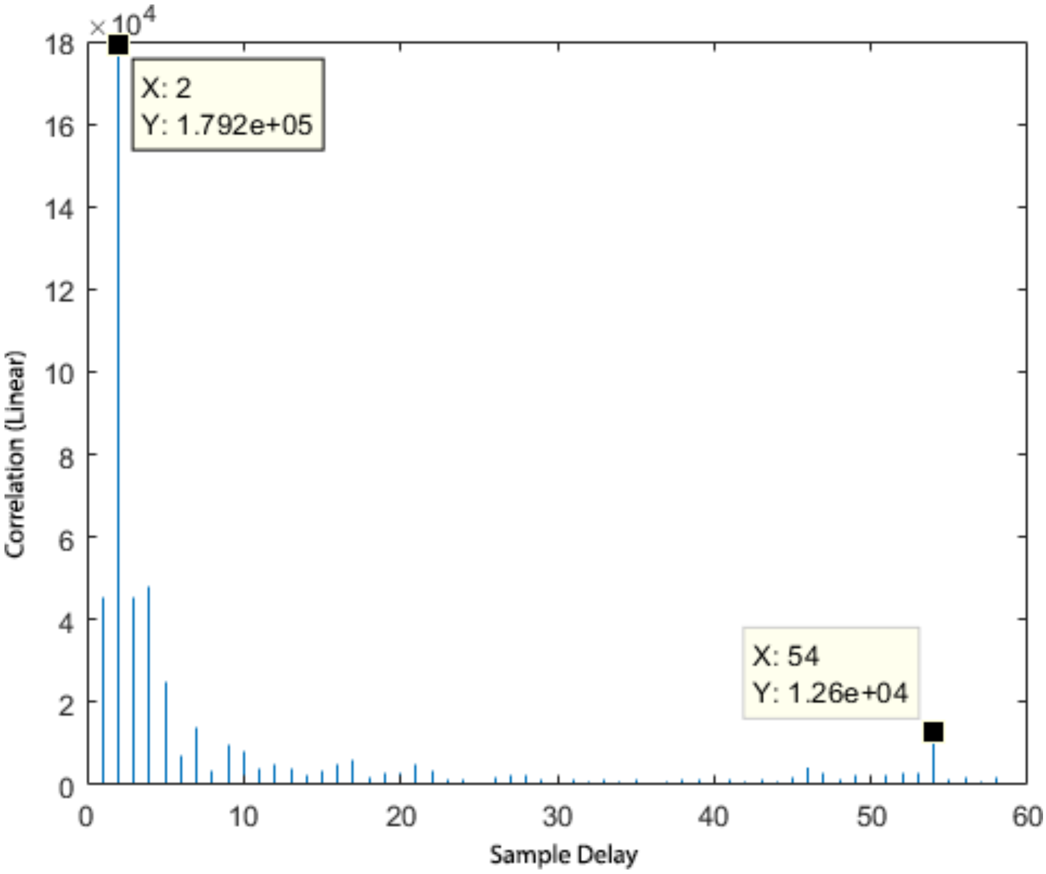

***Figure 6-2**: Preliminary results from the experimental procedure to validate the methodology. Autocorrelation at the receiver showing the first lag 52 samples away from the main peak. Results obtained at Kings Rd, Parafield, South Australia.*

Geometric distance estimates the radio wave time of flight difference between the direct and repeated path as 3.41 microseconds. With a sampling rate of 1.536 MSPS, it was expected to observe a lag 52.42 samples from the autocorrelation peak. The Figure 6-2 recording shows that the well-defined lag agrees with this estimation. The sample rate of 1.536 MSPS also specifies that each peak bin contains the path equivalent of 195.18 m. To further improve the resolution, the phase cross correlation methods discussed in Section 5.2.3 were then applied to each measurement (see Figure 6-3).

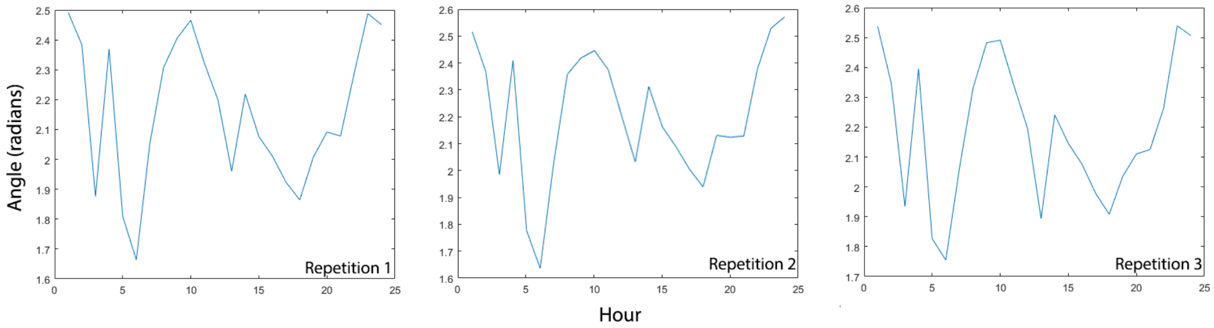

***Figure 6-3**: Phase cross correlation method outlined in Section 5.2.3 measurement repetition 1/2/3 respectively.*

Each repetition follows a clearly identifiable pattern across the 24-hour period with only minor variance. The exact cause of this particularly non-smooth diurnal phase change is only revealed when compared to independent weather observations at the time.

BoM data was used to provide an estimate of the key quantities of temperature, pressure, and water vapour over the flight path and is shown in Figure 6-4.

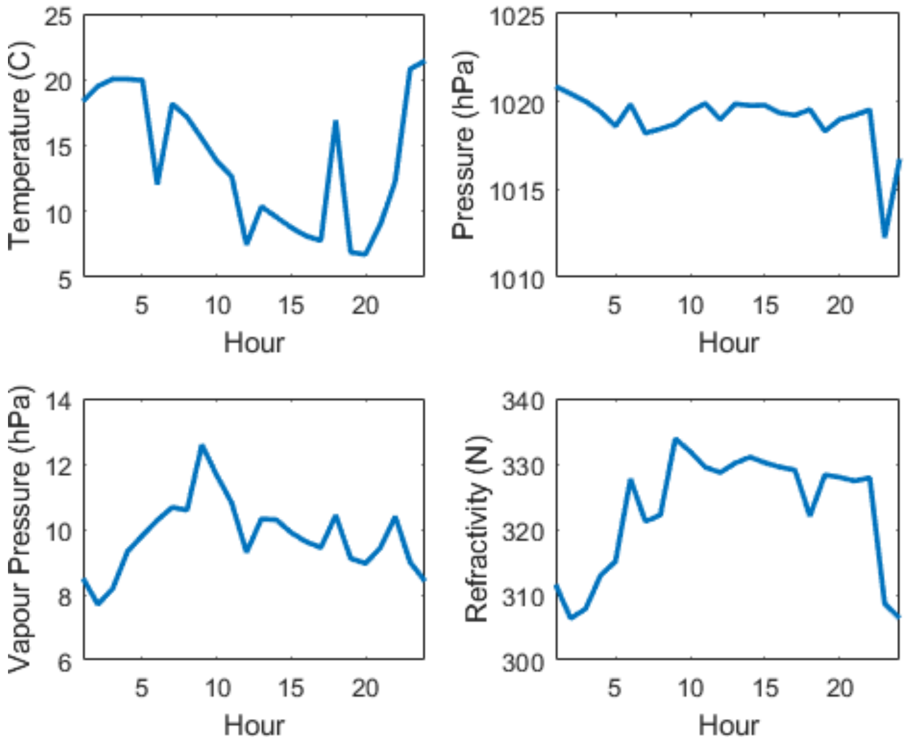

***Figure 6-4**: Observed weather quantities (temperature, pressure, vapour pressure) and calculated path refractivity taken at the same time as preliminary measurements.*

The most important chart in Figure 6-4 is the calculated refractivity over time, which directly relates to the phase cross correlation measurements. It can be seen that the measurement plot has some similar spikes to the observations nearby hour for hour within the microclimate of this short distance. However, due to various factors which will be explored later in the thesis, a qualitative relationship could not be definitively established. This preliminary test gave good indication the goals of the thesis could be attained by the methods presented therein; however, a higher resolution ADC was needed to further identify the connection.

6.3 Primary Results

Displayed here is all of the pertinent information from each primary measurement day at the same location as used in preliminary experimentation. The 24-hour measurement days span across several months (17th August 2017 until the 7th October 2017) to obtain both diurnal and seasonal changes. Analysis over a longer period could not be done due to the procedural feasibility and administrative hardships in the lead-up to each experimentation. Even obtaining the 5 days presented in this section required extensive preparation, and some degree of good fortune with weather. It was also a physically demanding undertaking for a sole experimenter. It was planned to obtain five measurements per hour, every hour for 24 consecutive hours; and gaps in the data indicate where this was not possible. Information contained here can be replicated by taking the recorded data and scripts as provided, which have both been submitted along with this thesis. Only results using the 16-bit ADC have been presented; the alternate RTLSDR ADC data and additional test days can be found in the extra material.

Brief descriptions of each day were noted and are shown here for quick reference – note times are given in 24 hour Coordinated Universal Time (UTC) plus Australian Central Standard Time (ACST) offset:

- 17-18th August 2017. Start Time: 12:30+09:30. Windy day with light showers during the night.
- 1-2nd September 2017. Start Time: 11:00+09:30. Light winds with heavily increasing rain during the night.
- 14-15th September 2017. Start Time: 10:30+09:30. Easing winds with very light showers.
- 21-22nd September 2017. Start Time: 10:00+09:30. Light rain with light winds, cloud cover.
- 6-7th October 2017. Start Time: 11:30+10:30. Dry, warm, spring day.

6.3.1 Phase at the First Lag

Phase at the first defined lag peak, shown both wrapped and unwrapped. Recall that each hour had 5 sequential measurements, giving 120 points over an entire day.

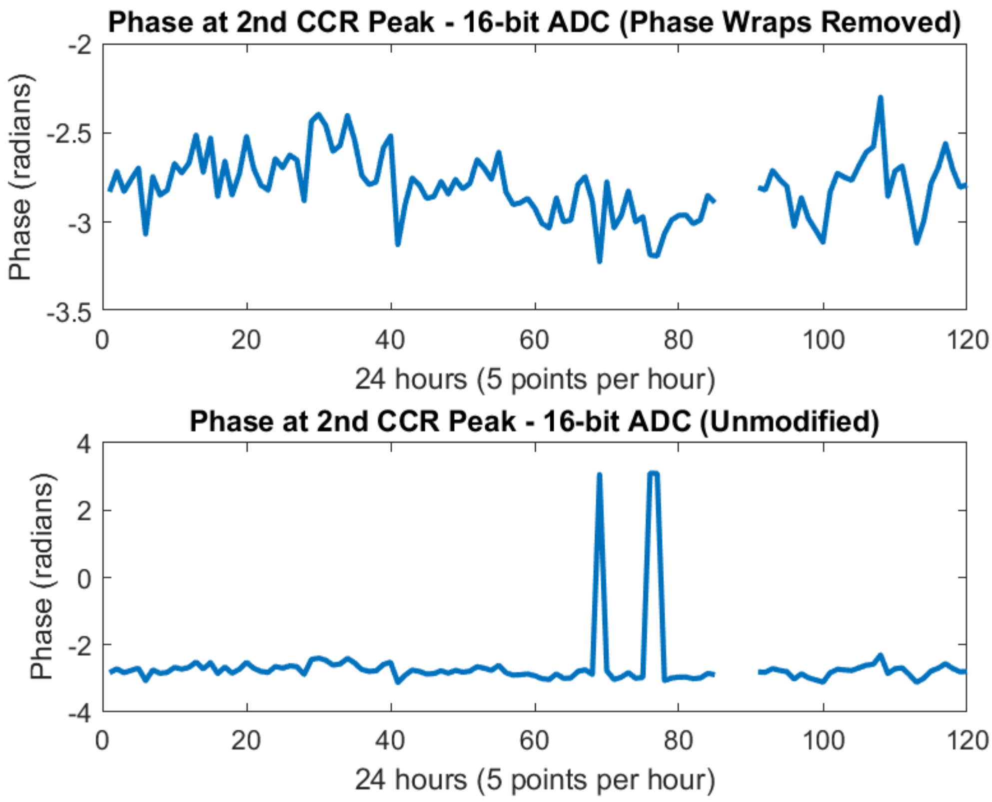

Figure 6-5*: Phase at the cross correlation peak – 17-18th August 2017. Gaps in data indicate no recordings available.*

Figure 6-5 showing cross correlation at the peak indicates several wrapped phase measurements and subsequent unwrapping. The wrapping events do not persist over multiple measurements on the same hour.

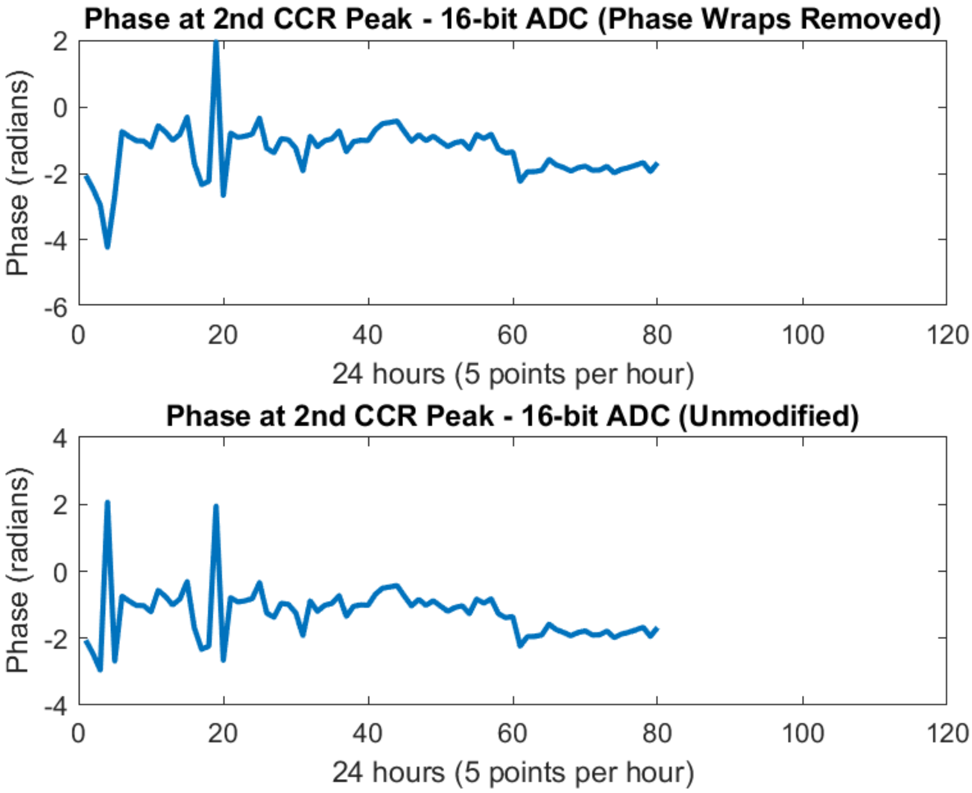

***Figure 6-6**: Phase at the cross correlation peak – 1-2nd September 2017. Gaps in data indicate no recordings available.*

Phase measurements in Figure 6-6 indicate wrapping events again, this time in the first hour of recording. Even after unwrapping, in the first hour of recording the phase can be seen to change by 2 radians across the sequential measurements. Note on this day rain increased during measurement recording, and the severe rain halted experimentation at 2 am 2nd September.

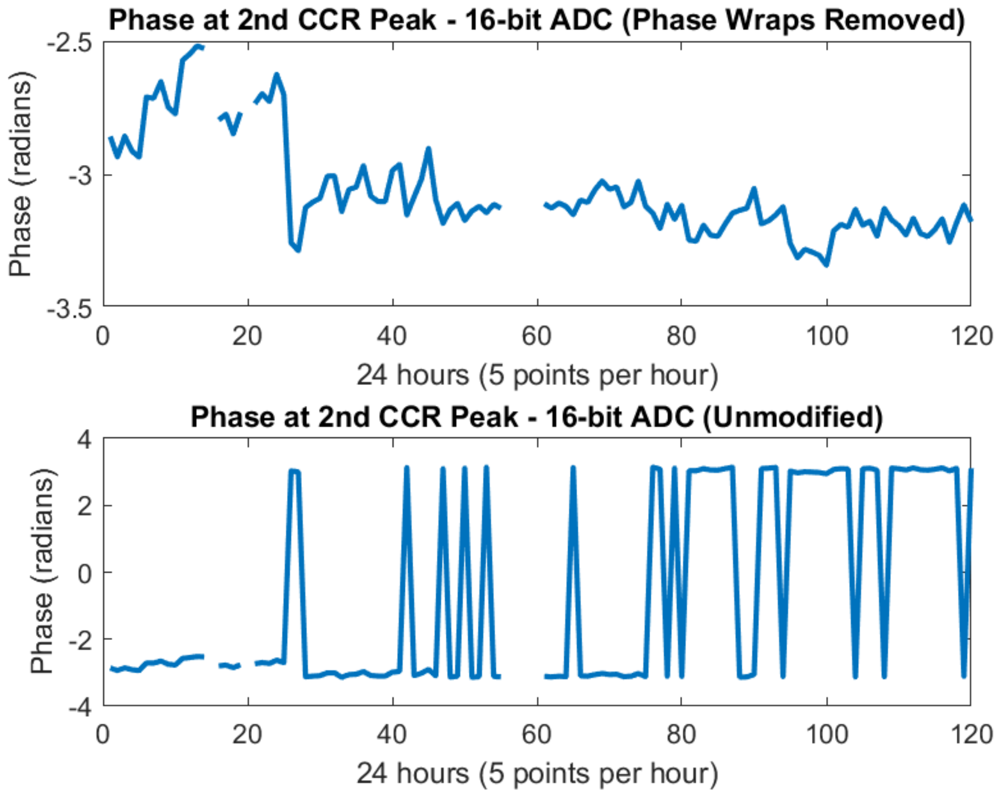

***Figure 6-7**: Phase at the cross correlation peak – 14-15th September 2017. Gaps in data indicate no recordings available.*

Figure 6-7 shows repeated phase wrapping events across the entire time period. These wrapping events are repeated in the sequential measurements in the later hours of recordings (80th – 120th points). A large jump in phase remains after unwrapping the phase after the 5th hour of recordings (25th point) and centres around a mean of -3.2 radians for the remainder of the measurements.

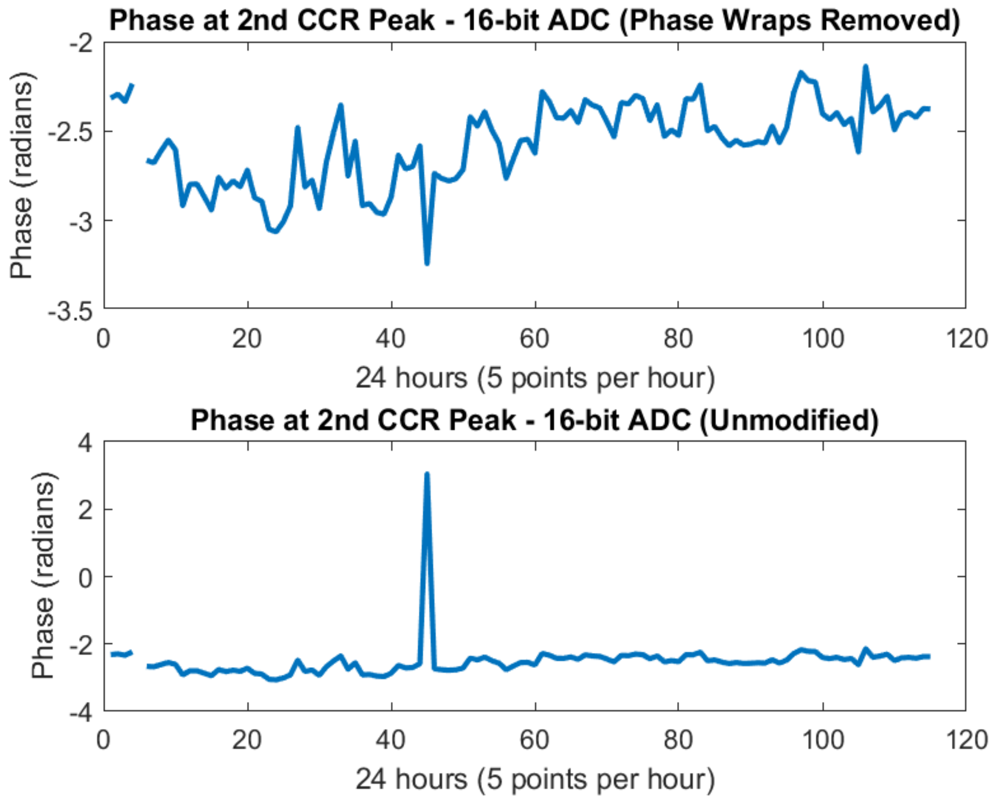

***Figure 6-8**: Phase at the cross correlation peak – 21-22nd September 2017. Gaps in data indicate no recordings available.*

Figure 6-8 shows what looks like a relatively stable day according to radio wave propagation, with a slow but steady trend upwards in the phase offset after an initial decrease in the early hours.

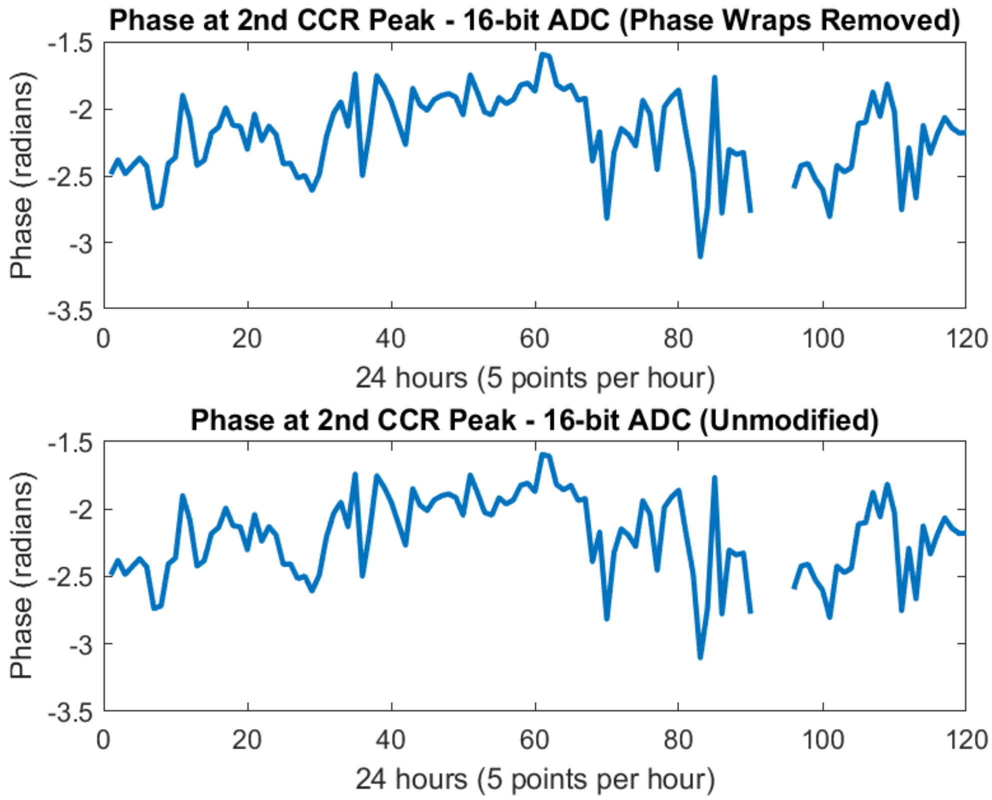

***Figure 6-9**: Phase at the cross correlation peak – 6-7th October 2017. Gaps in data indicate no recordings available.*

Figure 6-9 shows this day curiously being the first measurement day to experience no phrase wrapping. This was taken on the calmest, driest, day.

6.3.2 Averaging the Hourly Data

Mean, mode, and median of the five results obtained each hour. These averages help to visually see hourly changes easier, and hopefully smooth out any peculiarities in the sequential hourly recordings. The average is presented as mean, mode, and median to avoid potentially improper smoothing and embellishment of data.

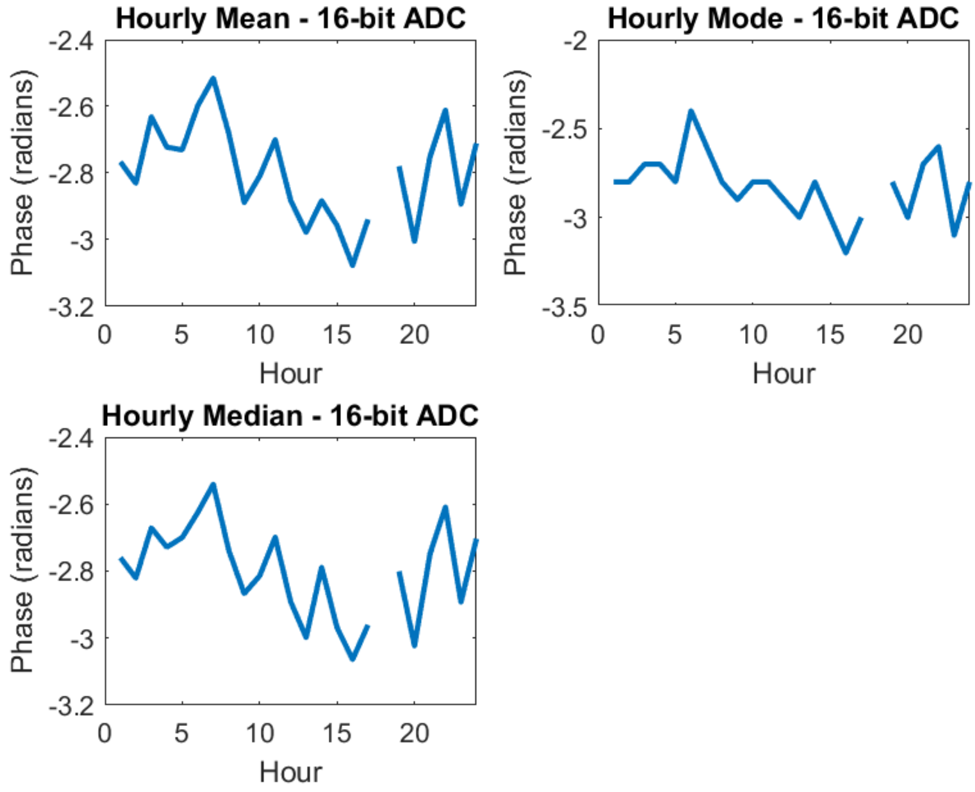

***Figure 6-10**: Hourly averages of the phase at the cross correlation peak - 17-18th August 2017. Gaps in data indicate no recordings available.*

Figure 6-10 shows averages of the five measurements per hour into one, with the mode losing definition in several peaks due to significant figure truncation. The phase trend is characterised by an early rise, then fall, ending with another rise. The fall can be seen from hour 6 until hour 18, curiously lasting half a diurnal cycle.

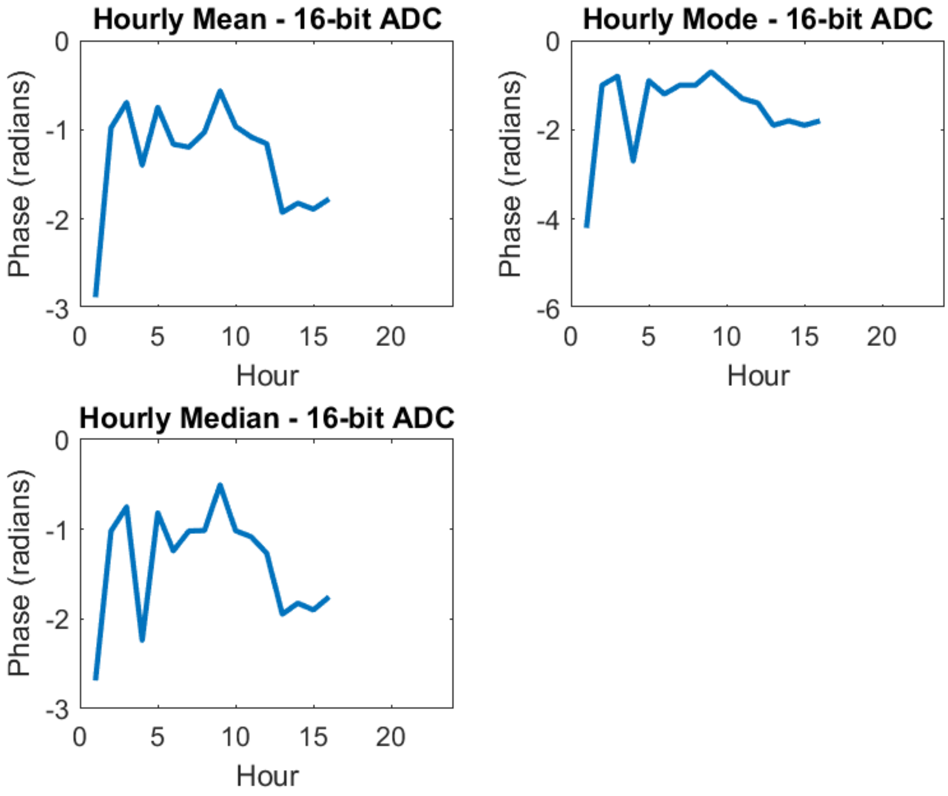

Figure 6-11*: Hourly averages of the phase at the cross correlation peak - 1-2nd September 2017. Gaps in data indicate no recordings available.*

The averages in Figure 6-11 possibly hint at the severe weather about to occur (sharp dip in phase around the 14th hour). Measurements were stopped at this time due to severe rain. The first hour retains outlandish variations, as originally seen in Figure 6-6.

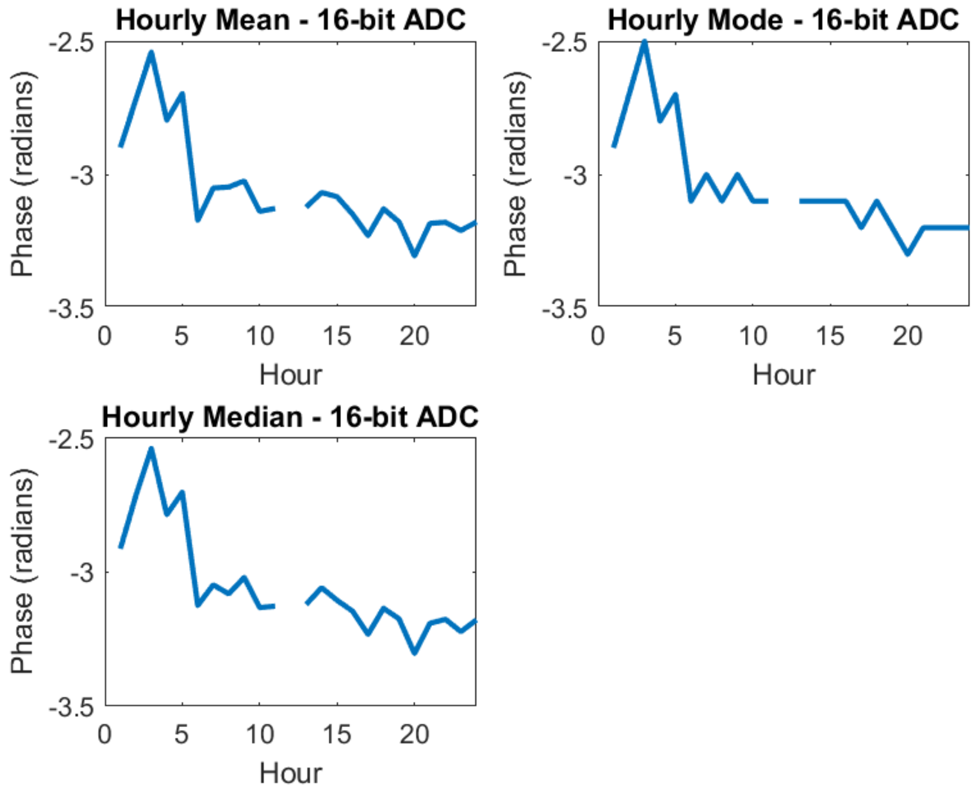

__Figure 6-12__: Hourly averages of the phase at the cross correlation peak - 14-15th September 2017. Gaps in data indicate no recordings available.

Figure 6-12 shows that the phase offset decreases sharply after 5 hours and stays low for the remainder of the experimental day. All three averages show very similar trends.

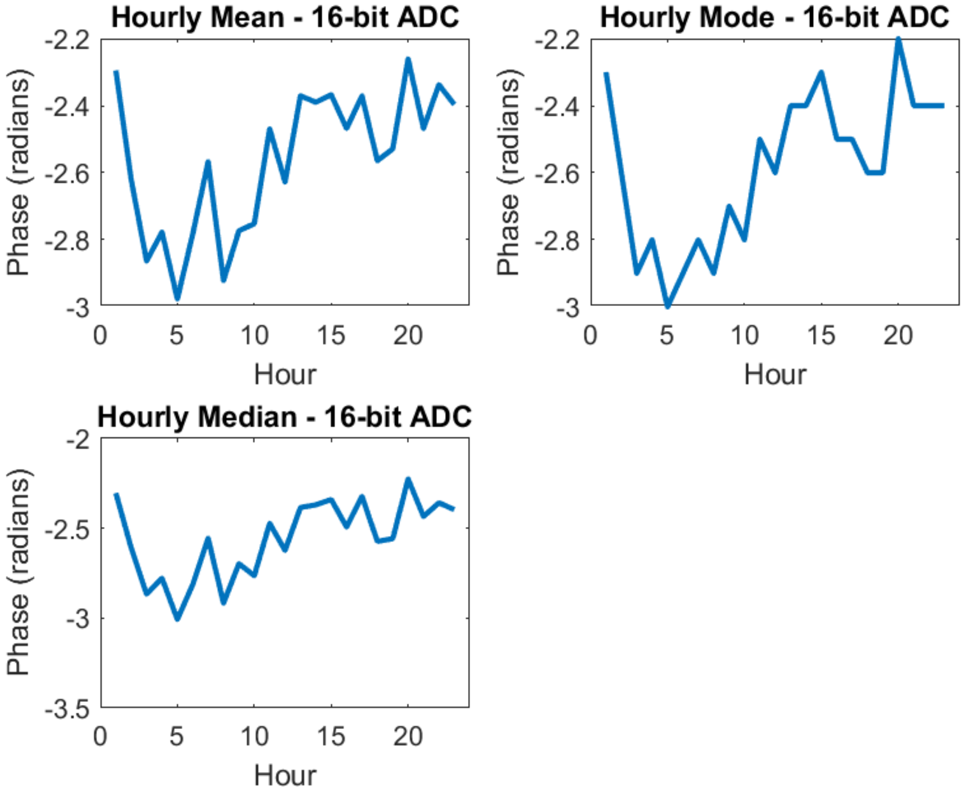

Figure 6-13*: Hourly averages of the phase at the cross correlation peak - 21-22nd September 2017. Gaps in data indicate no recordings available.*

Figure 6-13 shows a sharp drop in phase early on, and then steadily rises over the rest of the experimental day. A dip is noticed around the 18th and 19th hours. The mode hides the local peak at the 7th hour.

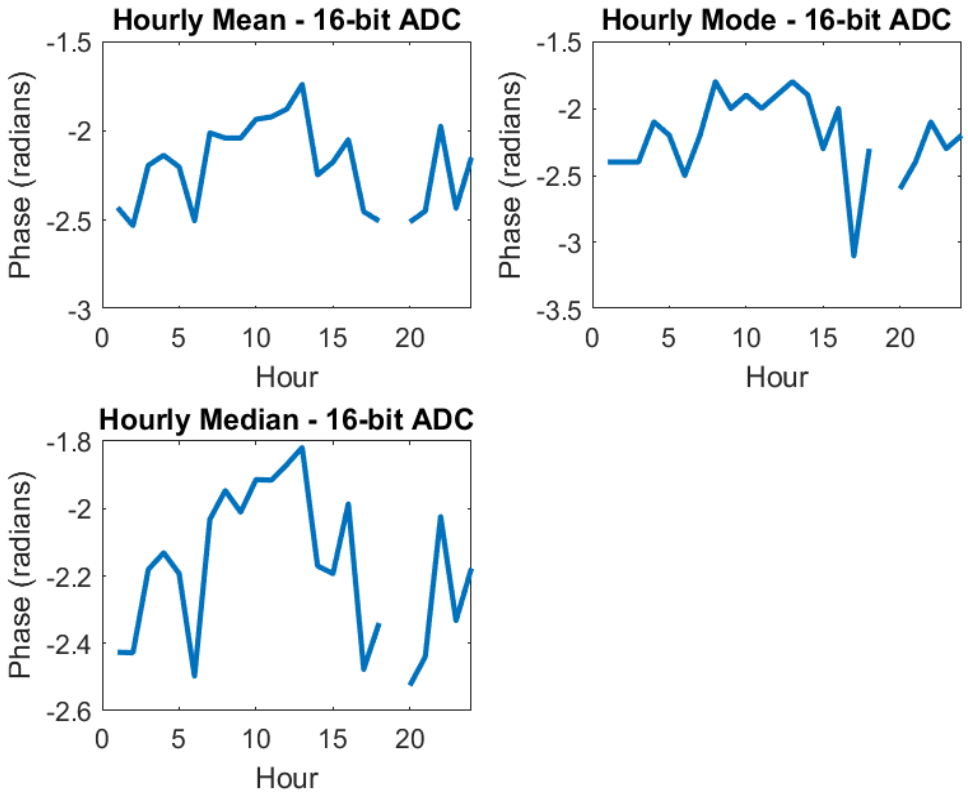

***Figure 6-14**: Hourly averages of the phase at the cross correlation peak - 6-7th October 2017. Gaps in data indicate no recordings available.*

Figure 6-14 shows a rise then a fall, followed by a rise and fall again, over the period. Once again the shape of the mode looks the most different compared with the mean and median averages.

6.3.3 Expected Phase from BoM NWP

Path averaged atmospheric refractive index given by BoM NWP translated to expected phase (via Section 1.4.1). This data is subject to effects of smoothing from the NWP's grid interpolation. To uncover the link between radio wave propagation and weather, it is hoped that the plots in this section show some sort of relationship to the radio measurements presented in Sections 6.3.1 and 6.3.2.

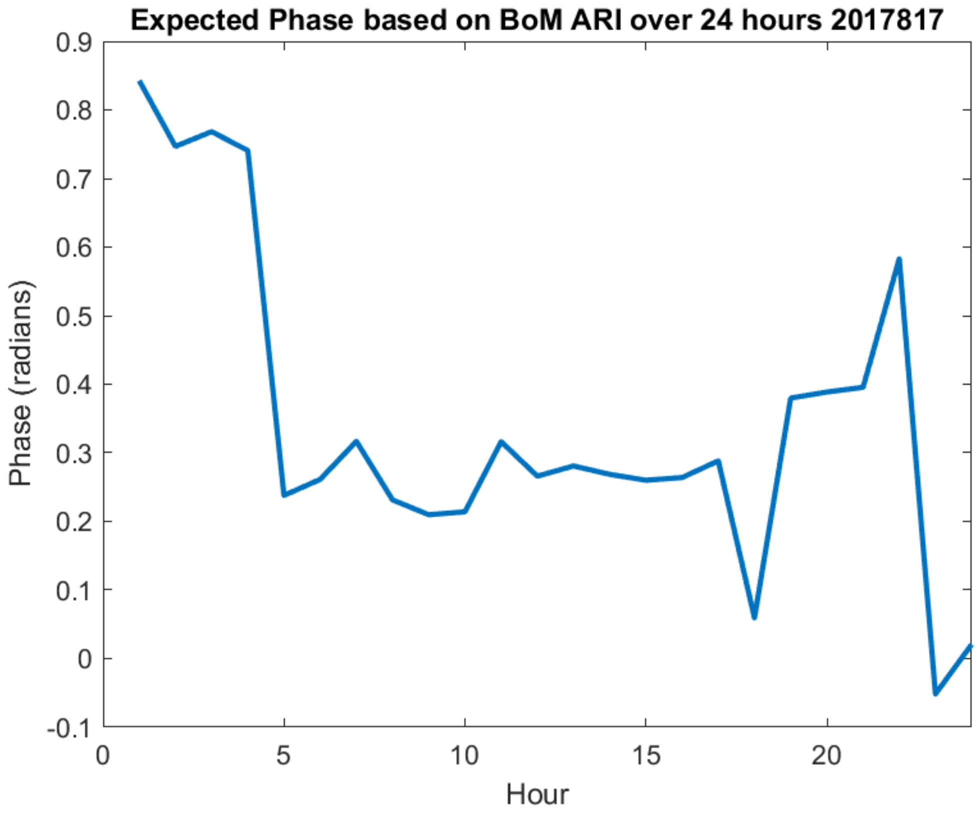

***Figure 6-15**: Hourly anticipated phase over the radio path from BoM interpolations - 17-18th August 2017. Gaps in data indicate no recordings available.*

Figure 6-15 shows the anticipated phase having two peaks during the mornings of each day, which the observed phase also contains (6th and 21st hours), albeit shifted by a couple of hours for the first.

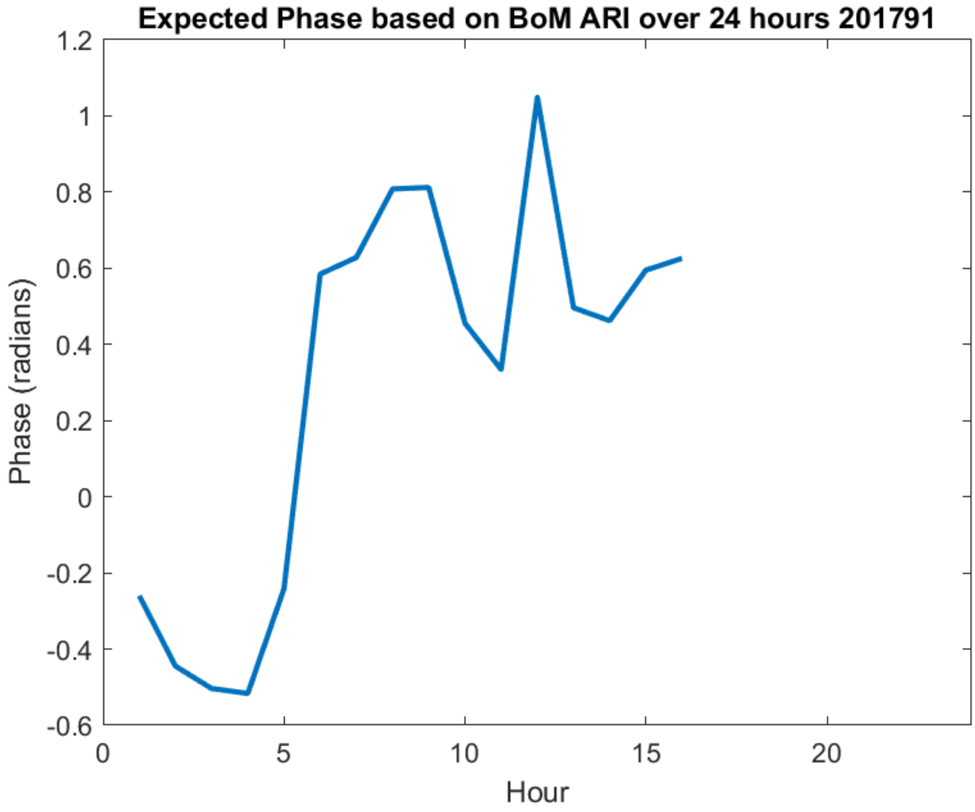

__Figure 6-16__: Hourly anticipated phase over the radio path from BoM interpolations - 1-2nd September 2017. Gaps in data indicate no recordings available.

Figure 6-16 showing phase wrapping at the 7th hour (above 2π). Similar shape to the averaged phases of this day (see Figure 6-11). The missing final hours of the day make it hard to draw any further conclusions from this day, but the larger changes in phase (varying phase of approximately 1.5 radians) also occur in the experimental data.

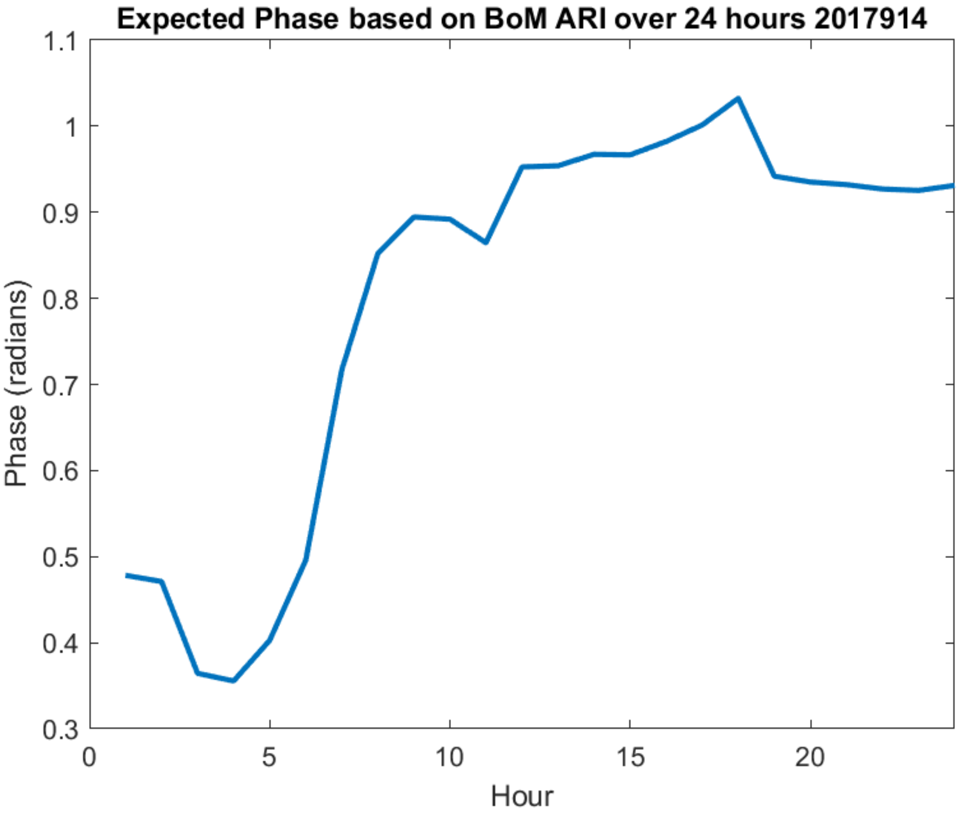

***Figure 6-17**: Hourly anticipated phase over the radio path from BoM interpolations - 14-15th September 2017. Gaps in data indicate no recordings available.*

Figure 6-17 illustrates that after the 6th hour, the BoM NWP predicts an event followed by stabilisation. Average recorded phases (see Figure 6-12) also predict an event at the 6th hour, however the direction of the phase is opposite. The range of the phases across the diurnal cycle are also quite tight (approximately 0.7 radians), which again is seen in the experimental data.

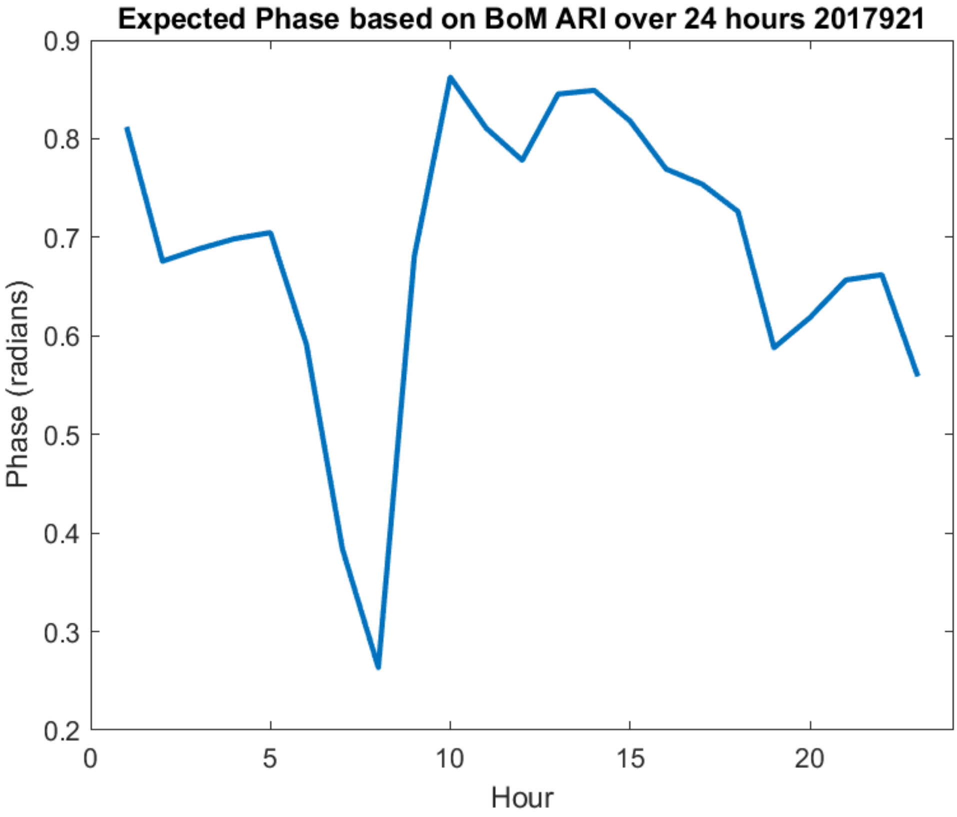

***Figure 6-18**: Hourly anticipated phase over the radio path from BoM interpolations - 21-22nd September 2017. Gaps in data indicate no recordings available.*

Figure 6-18 shows a sharp dip occur at the 5-8th and 18th hours, with only the dip occurring at the 18th hour being present in the radio wave recordings.

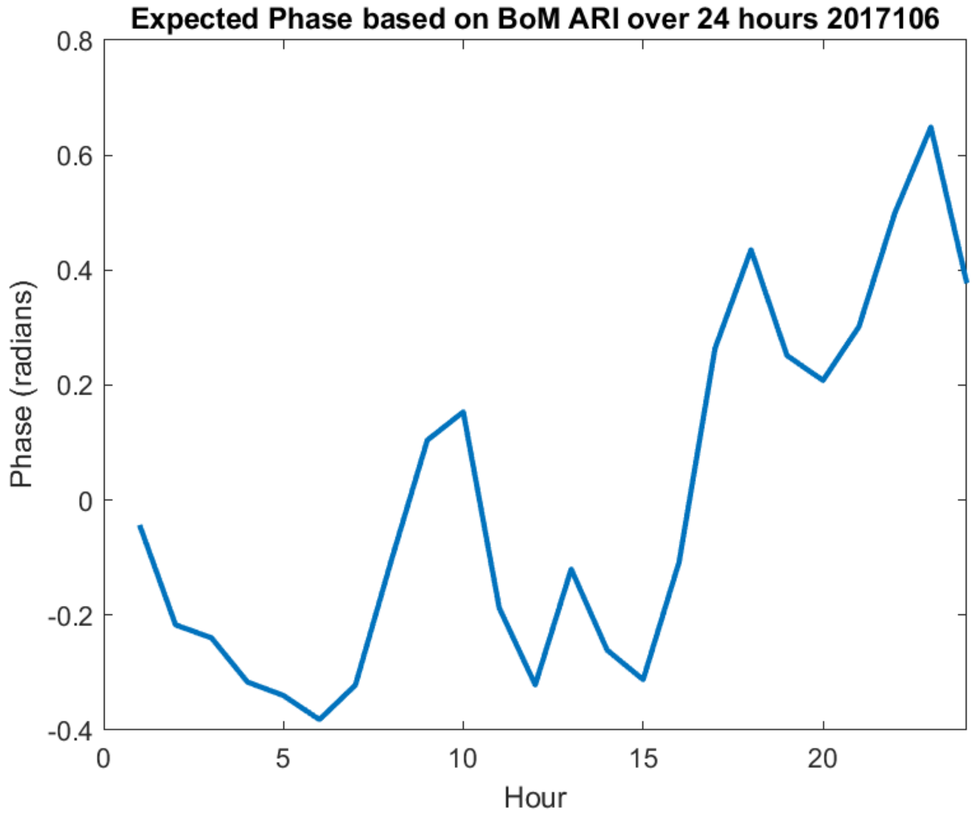

Figure 6-19: Hourly anticipated phase over the radio path from BoM interpolations - 6-7th October 2017. Gaps in data indicate no recordings available.

Figure 6-19 also shows a rise and a fall followed by a rise; however, the final rise is much higher than measured by radio waves. There is no apparent correlation with the recorded data shown in Figure 6-14.

6.3.4 Path Averaged Refractivity vs Parafield Observations

Parafield airport point atmospheric refractive index versus BoM NWP output over the radio path (same shape as 6.3.3 figures but translated into different units). Comparing these two data sources give a some measure of confidence in the validation data, but may also highlight discrepancies in point observations versus the processed NWP output of the radio path. For reference, the lower tropospheric air over ground can have refractivity values of around 230-400 N.

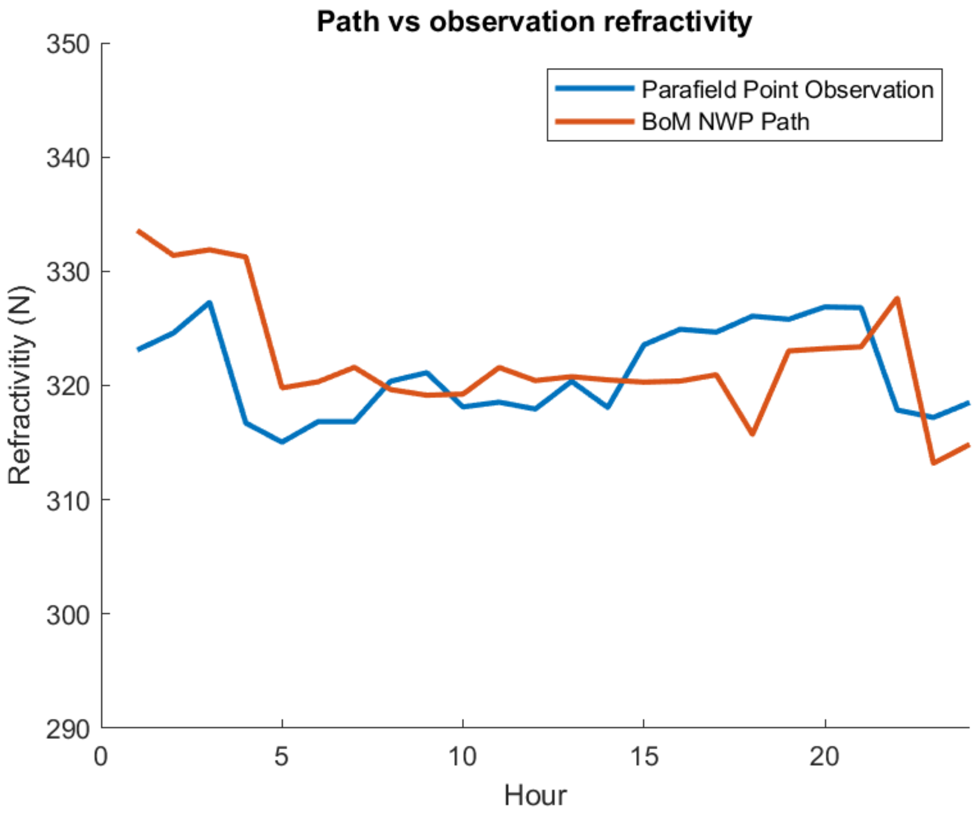

Figure 6-20: *Hourly observed refractivity at single point near the receiver - 17-18th August 2017. Gaps in data indicate no recordings available.*

Parafield airport weather observations in Figure 6-20 having similar rises and falls shown in the NWP output. The values of the refractivity, N, are also of similar magnitudes (considering the typical range of N values).

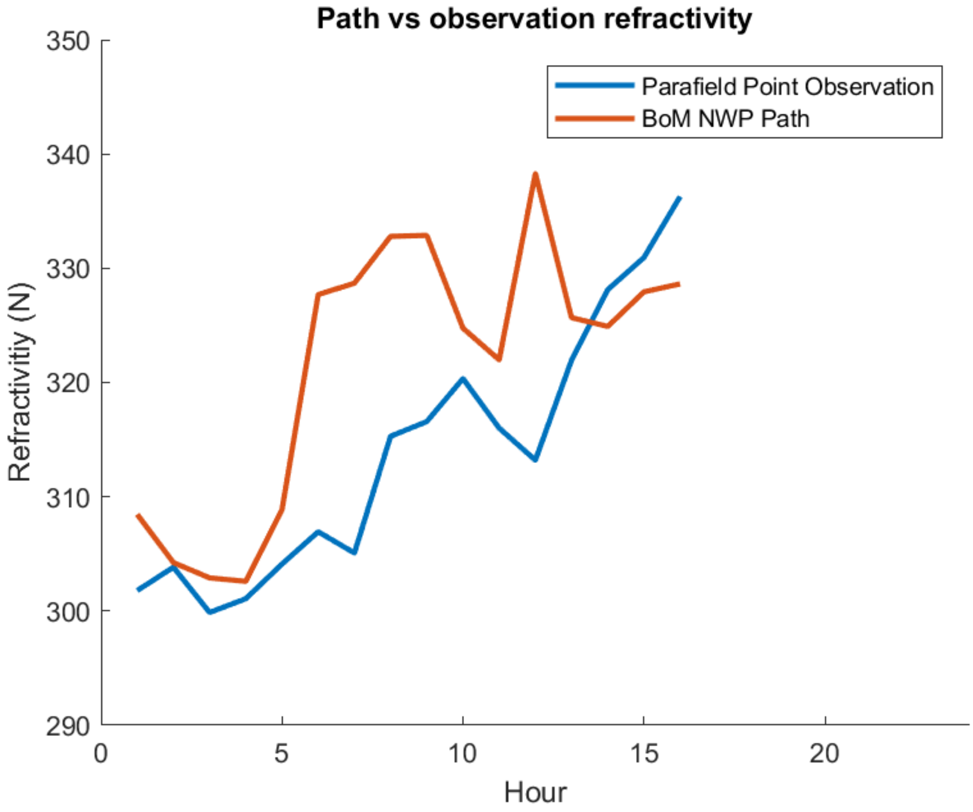

***Figure 6-21**: Hourly observed refractivity at single point near the receiver - 1-2nd September 2017. Gaps in data indicate no recordings available.*

Figure 6-21 shows a steady increase in the refractivity, possibly due to increasing rain and severe weather as measurements went on. Refractivity values between the two plots deviate principally during the 6th-10th hours.

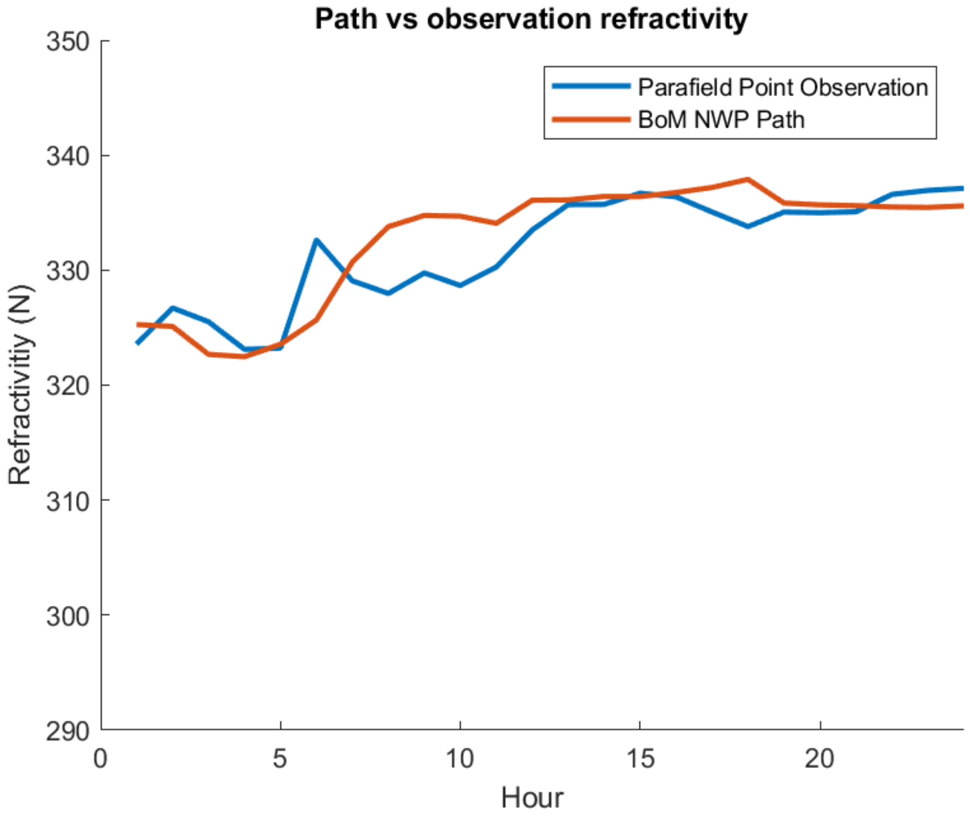

***Figure 6-22**: Hourly observed refractivity at single point near the receiver - 14-15th September 2017. Gaps in data indicate no recordings available.*

Figure 6-22 agrees with the slowly increasing refractivity over time for both point and path. Refractivity values are almost matching across the hours.

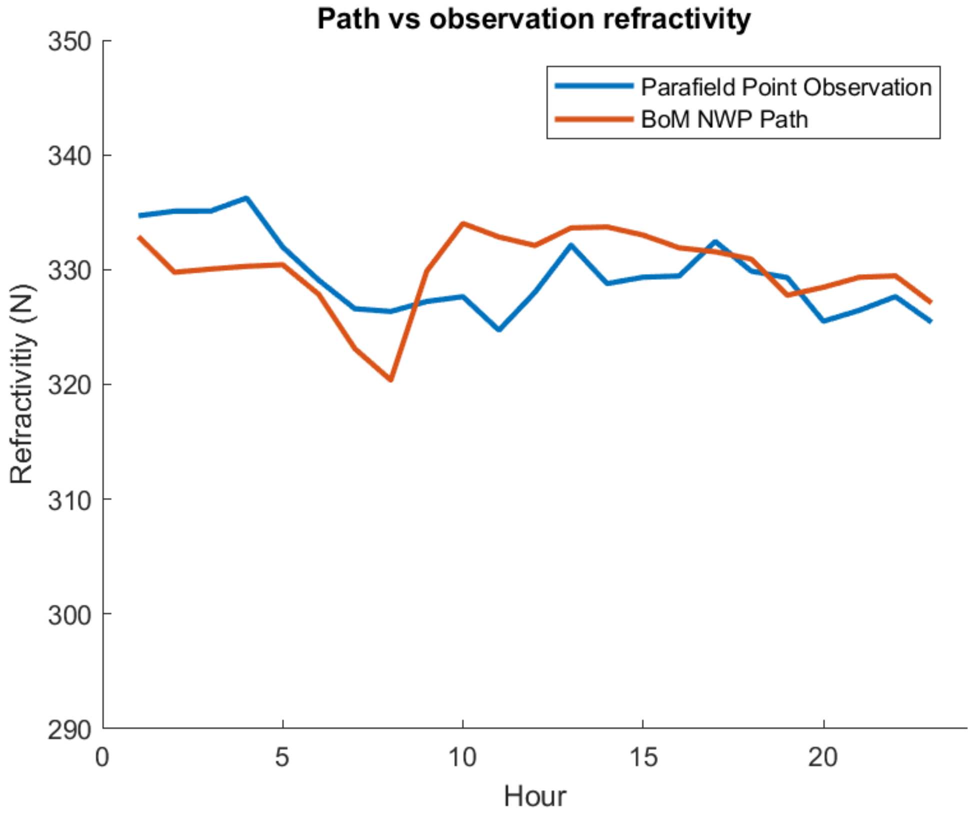

***Figure 6-23**: Hourly refractivity at single point near the receiver (blue) and along the radio path (red) - 21-22nd September 2017. Gaps in data indicate no recordings available.*

Figure 6-23 observes variations between the point and path, but still follows a similar global trend and absolute refractivity value.

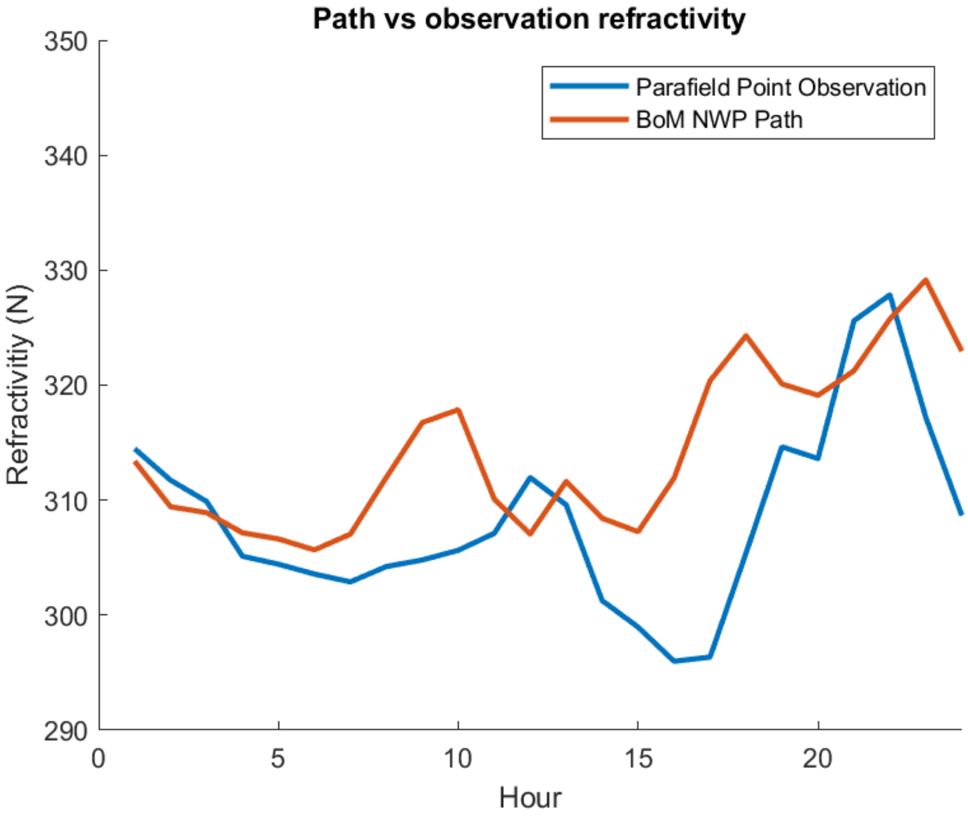

Figure 6-24: *Hourly refractivity at single point near the receiver (blue) and along the radio path (red) - 6-7th October 2017. Gaps in data indicate no recordings available.*

Figure 6-24 shows roughly the same weather recorded as anticipated by the NWP, with generally lower refractivity near the receiver.

6.4 Results Comments

The results presented were collected using only the 16-bit receiver, and not the 8-bit RTLSDR receiver to minimise visual clutter. The 8-bit RTLSDR measurements illustrate a similar picture to what is presented in this chapter, and the data is available for the reader attached to this thesis.

Of interest, the results of the refractivity over the radio path has a trend very similar to the refractivity observations taken at a point nearby the receiver (see Figure 6-20 to Figure 6-24). Some slight left and right shifting can be seen on the dates where measurements were taken on the half of a UTC hour (1st and 21st September 2017), as these dates were half an hour shifted from NWP time outputs. The other minor differences observed between the

Parafield observations and BoM NWP output arise due to three possible factors: point observations compared to path averaged weather data, the physical distance of separation i.e. several hundred metres between the point and path, and observation versus prediction. Notwithstanding, the data does illustrate similarities between these independent weather information sources.

The expected phase (see Figure 6-15 to Figure 6-19) was calculated using the path refractivity data that included the temperature, air pressure, and vapour pressure. This is a linear operation (Equation 1-2). Each day analysed shows strong sense of related peaks and troughs, increases and decreases. However, these figures do have a clear relationship with the phase of the radio waves (Figure 6-10 to Figure 6-14).

These radio wave measurement results were unanticipated. Following the literature and theory, a method was devised and tested, and by all accounts should have captured the relationship between radio wave propagation and weather.

Looking to the validation data, whilst the localised measurements and the BoM data show broadly related trends across a 24 hour period, they have differences that are of the same order as the total variation of this period. The BoM data can be regarded as providing a mean, so the local measurements can be regarded as representative of the fluctuations about this mean. From this, it is apparent that for short propagation paths in these measurements, fluctuations in phase due to local variations in weather will dominate (see Figure 6-25). It is clear from this that much longer paths are required for observations to be representative of the BoM data.

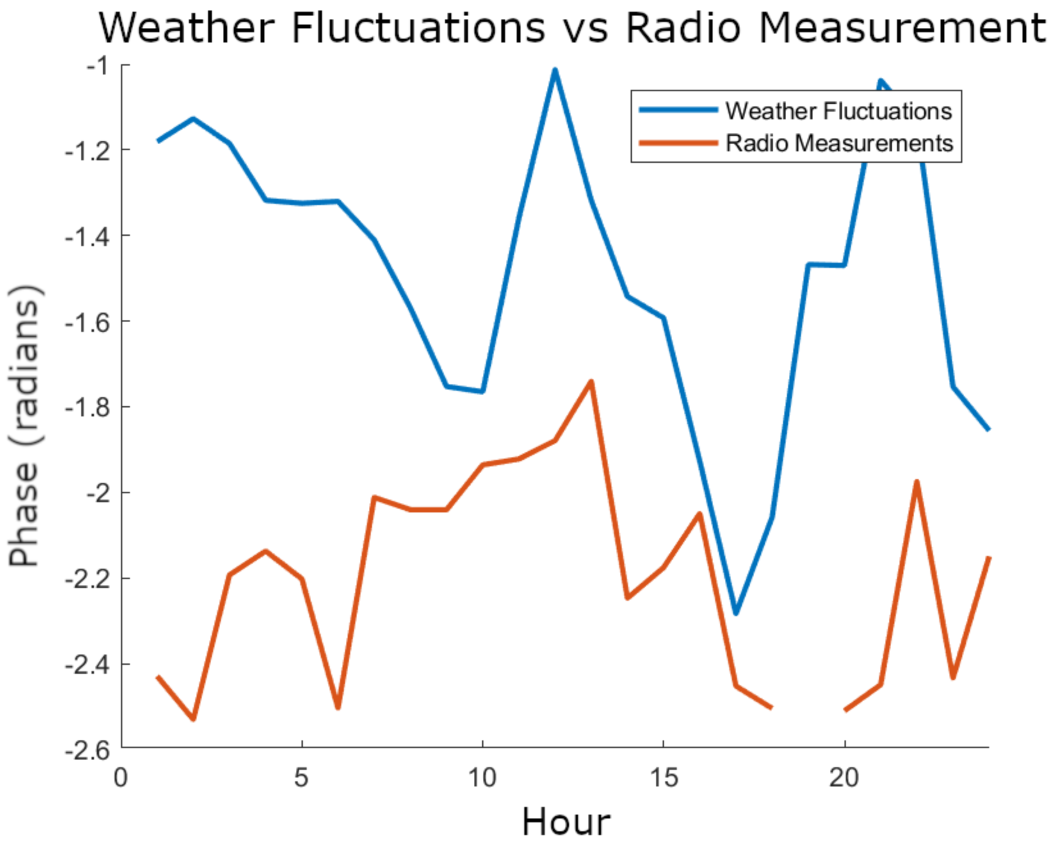

***Figure 6-25**: The difference (blue) between phase fluctuations derived from the mean weather and local weather measurements, when compared to (red) radio measurements over 24 hours - 6-7th October 2017.*

Figure 6-25 shows that dominating local weather effects follow a pattern also observable in the radio wave recordings. This demonstrates an evident link between local weather effects and radio wave propagation – with the caveat that it was not what was intended to be measured, and so is not able to be independently validated.

6.5 Results Summary

This chapter has presented a portion of the results obtained from using only the 16-bit ADC during experimentation, however the results were not what was expected. Results do not visibly follow the trends presented in BoM NWP output, nor Parafield observations. Whilst there has been shown to be a link between the local weather fluctuations and radio measurements, this was not anticipated to be as much of a major influence on the results as it appears. Consequently, this research was not, and likely could not, be prepared for its impact.

This thesis hoped to find an independently verifiable link between radio wave propagation and the weather. By comparing timed radio wave propagation to that of the BoM NWP output, it was anticipated for a much stronger relationship to exist than has been observed in this experimental research. The discussion in Chapter 7 will explore reasons why this is the case.

7 Discussion

Perhaps the most interesting result comes from not being able to derive weather trends from the radio path. Whilst the phase is in broad agreement, and does not directly contradict expected results, it is evident that neither the BoM NWP nor the Parafield observations provide an accurate estimation of the phase fluctuations along the propagation path. Instead, both do provide a measure of real time deviations from the BoM predictions. However, for longer paths, it is expected that these fluctuations will average out. With this in mind, the remainder of this chapter describes possible sources of error under the expectation that the deviations are caused by the microclimate.

7.1 Phase Reliance Methodology

This project was dependent on relative phase measurements as a reliable method to track changes in weather. To investigate phase measurement reliability, it is necessary to examine the five repeated hourly measurements. A representative example of this is shown in Figure 7-1, which shows the spread of the phase angle at the lag peak, taken at a rate of five measurements per hour, indicated by the coloured dots. These five measurements are separated by less than a second. As is evident, there is a definite trend to be seen and each vertically stacked hour exhibits relatively small deviations. The spread of each stack is due to random effects, which will be discussed later in this chapter.

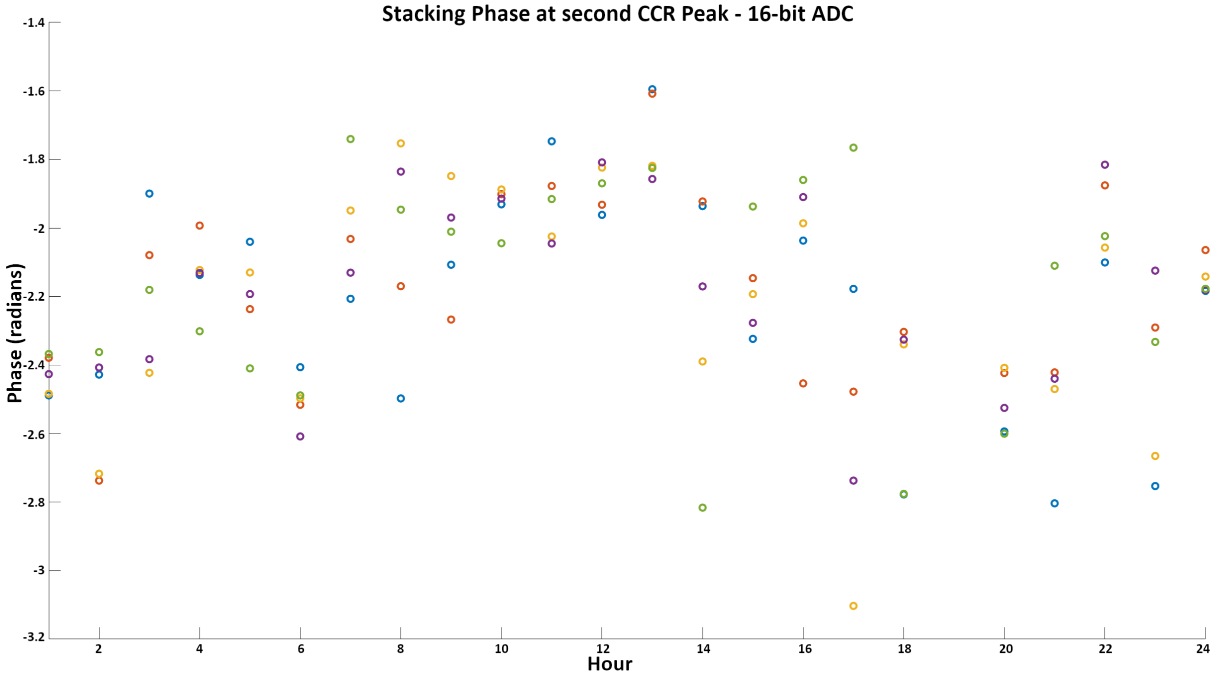

***Figure 7-1**: A representative example of vertically stacking the hourly phase measurements over an entire day (6th October 2017, 11:00 start). Repeated five times separated by less than a second when collected, and represented by the individual coloured dots.*

A deeper analysis of the stability within each measurement was performed by taking the entire length of IQ samples, 261144, and dividing it into 8 lots of smaller 32768 length batches. Within these 8 smaller batches, the phase was recalculated for each, and the minimum and maximum phases for the same day obtained (see Figure 7-2). From Figure 7-2, the minimum and maximum phases are typically only <0.5 radians apart (ignoring phase wraps) and follow the same trend. This establishes that the phase recorded on each measurement is stable and not affected by noise. Therefore the phase change is a stable measure of the weather, and it was the random weather effects that caused the results obtained in 6.3.

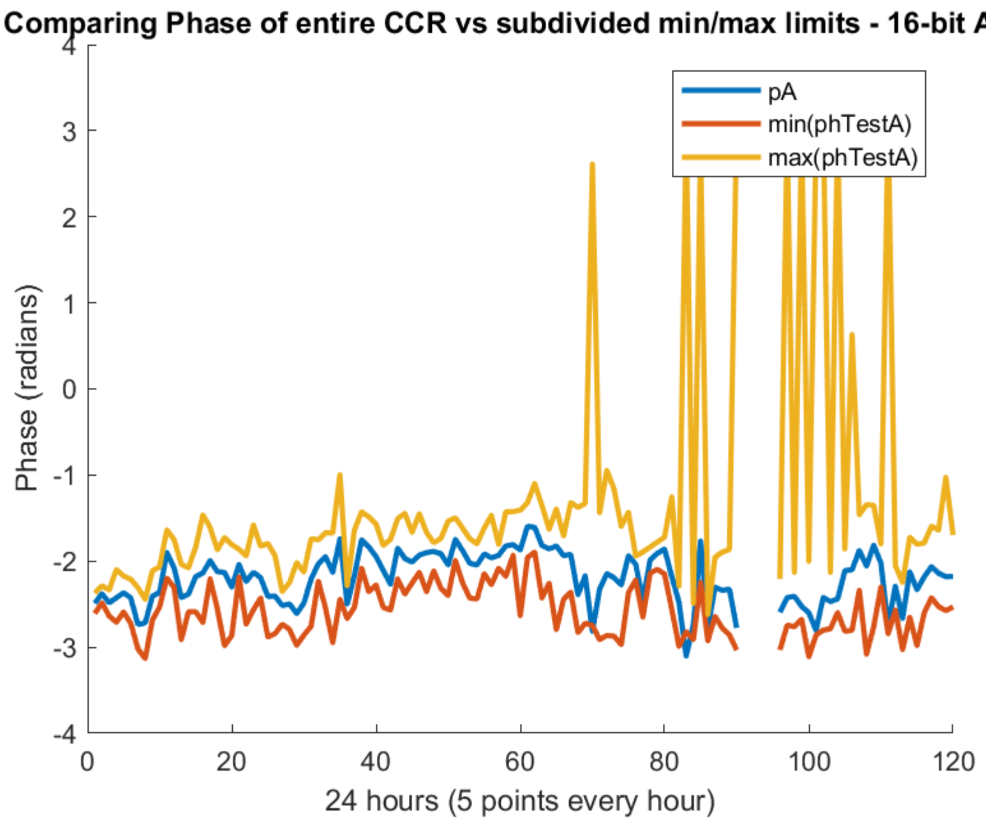

Figure 7-2*: Subdividing Inphase/Quadrature (IQ) samples and recording the minimum and maximum phase (spurious changes are due to phase wrapping).*

7.2 Sources of Random Error

7.2.1 Rain and Wind

Rain was present in various measurements with the exception of the measurements taken on 6 October 2017. Rain, as a form of precipitation, can cause attenuation and scattering on radio waves with more attenuation for shorter wavelengths. Rain is not a significant attenuating factor below 10 GHz [91], nor does it have an appreciable effect on phase-shifts below 5 GHz [92]. Consequently, since DAB has a frequency of 204.64 MHz, rain was not expected to be a significant factor.

Wind does not directly affect the propagation of the radio wave; but wind does cause fluctuations in refractivity (from temperature, pressure, water vapour shifts). Additionally, wind does affect the antenna direction, which is be a source of error and discussed in Section 7.2.3. Further investigation was performed to analyse the relationship between wind and phase variations. In Figure 7-3 through Figure 7-7, the maximum phase variations measured (via stacking method in Figure 7-1) are compared against the wind speeds recorded near the receiver.

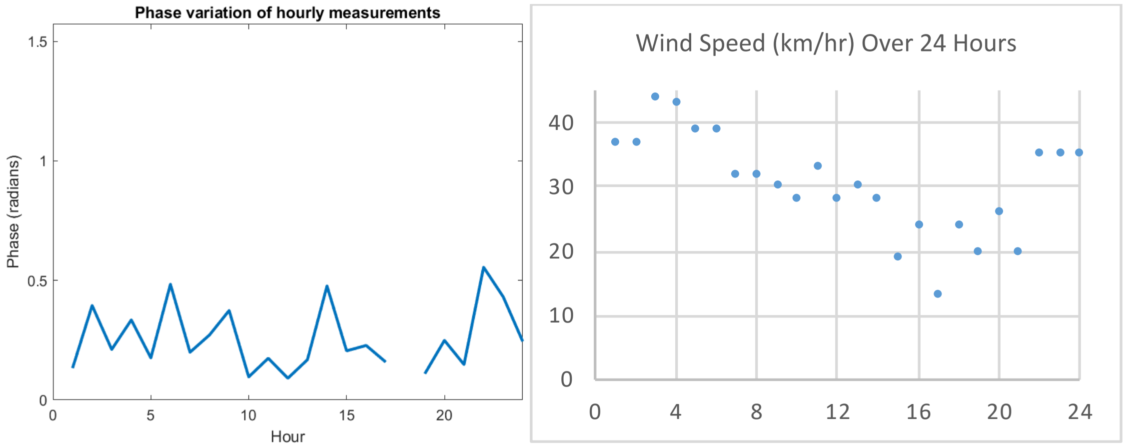

__Figure 7-3__: Changes over 24 hours of (left) phase variations vs (right) wind speed in km/hr – 17-18th August 2017.

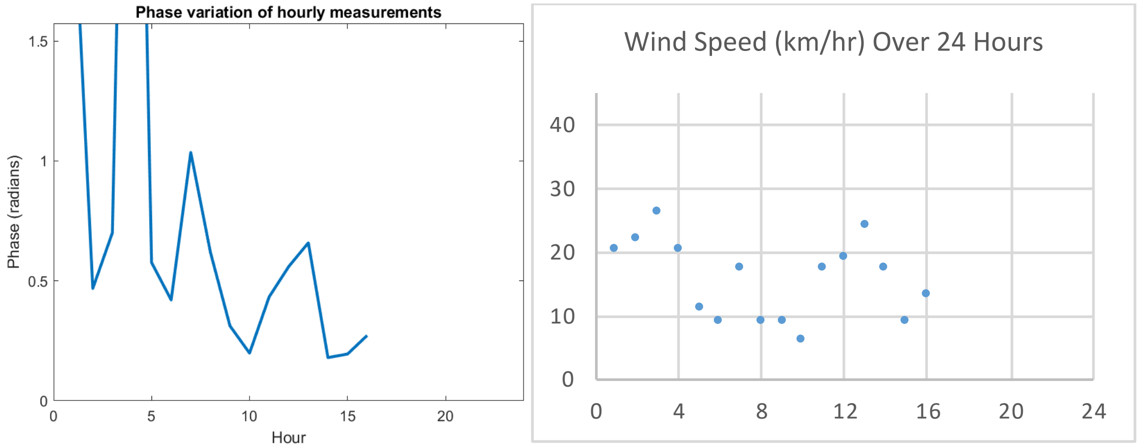

__Figure 7-4__: Changes over 24 hours of (left) phase variations vs (right) wind speed in km/hr – 1-2nd September 2017.

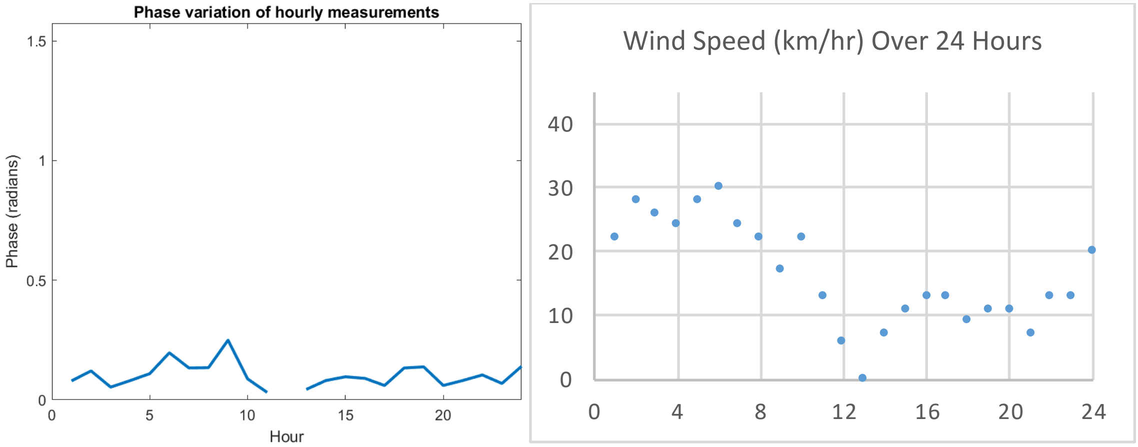

__Figure 7-5__: Changes over 24 hours of (left) phase variations vs (right) wind speed in km/hr – 14-15th September 2017.

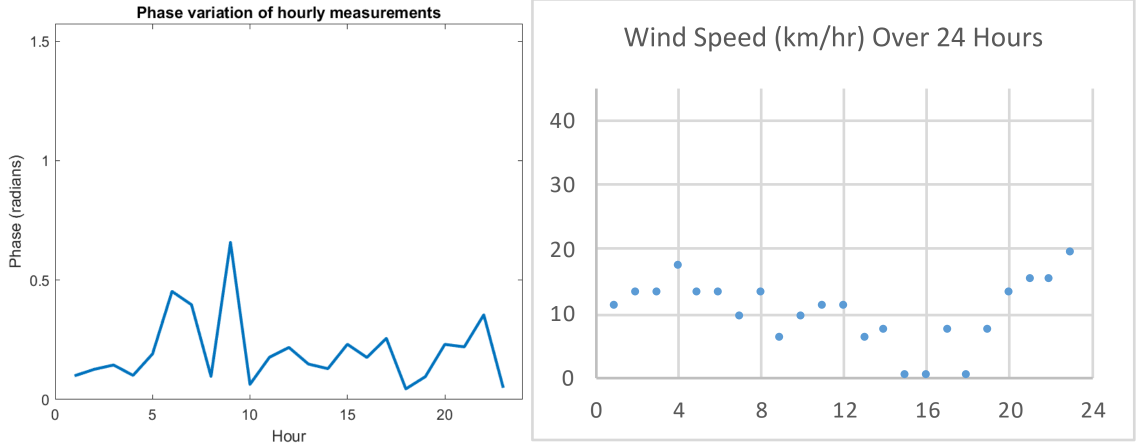

__Figure 7-6__: Changes over 24 hours of (left) phase variations vs (right) wind speed in km/hr – 21-22nd September 2017.

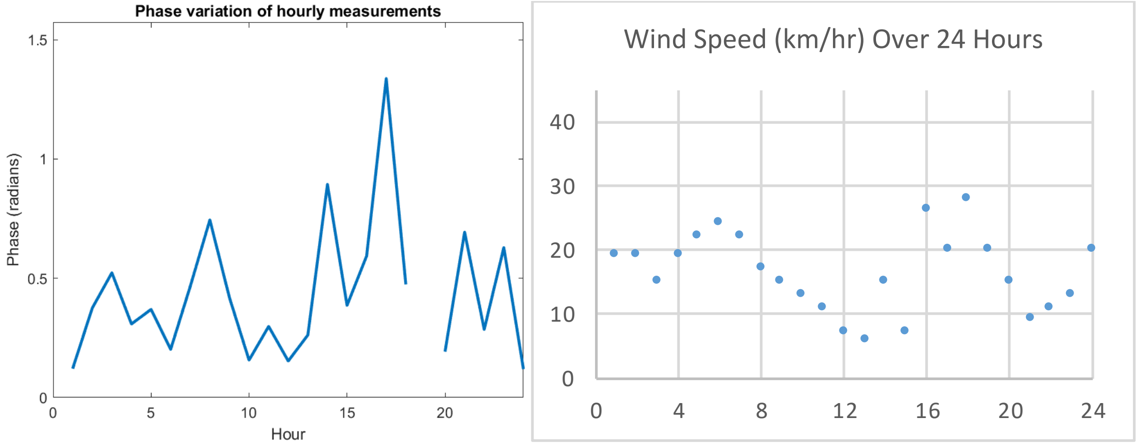

__Figure 7-7__: Changes over 24 hours of (left) phase variations vs (right) wind speed in km/hr – 6-7th October 2017.

Figure 7-3 through Figure 7-7 all use consistent ranges, and as can be seen, a stronger wind did not cause a larger variation of phase. The windiest day, 17th August 2017, had small amounts of phase variation, whereas calmer days like 1st September 2017, had seemingly wild variations in phase. The conclusion from this data is that the wind speed did not have an effect on propagation directly, and was only affected by the local atmosphere's refractivity makeup (temperature, pressure, water vapour).

7.2.2 Air Pollutants (Emissions)

Emissions are an unavoidable source of random error. Emissions are formed as a result of stationary sources (e.g. factories) and mobile sources (e.g. cars). Stationary sources of emissions over the path of interest make up the bulk of air pollution. Unfortunately, the contents of the stationary pollutants could not be identified and subsequently evaluated for the effects on results as the factories were unresponsive when required documentation was requested.

7.2.3 Antenna Drift

The two illuminating transmitting antennas described in Section 4.4.1 were checked during 40 km/hr wind for 'bucking' (horizontal and vertical movement). As magnetic compasses would not work in the water tower to orient the antennas during installation, a camera was placed above the antenna and compared against an enlarged quarter-compass diagram drawn on the ground below. This also facilitated in capturing the vertical deviations of the antenna, and the minimum and maximum shift was recorded. A similar approach was used for the vertical dimension. The intended bearing was set at 187.64 degrees, with a pitch of -0.71 degrees below the horizon. Maximum displacement at the end of the boom was measured at ±1.25 degrees horizontally and ±0.5 degrees vertically. Unlike the transmitting antenna, the receiving antenna (described in Section 4.4.2) on the ground only measured boom displacements of ±0.5 degrees horizontally and ±0.25 degrees vertically. These displacements caused fluctuations in the path and therefore phase shifting for the received signal. With the bearing and pitch known from the antenna installation, it was straightforward to translate to a Cartesian grid aligned with the intended antenna position. Thus, to obtain a 2D representation (see Figure 7-8), trigonometry was applied from this position and compared to the maximally displaced antenna position.

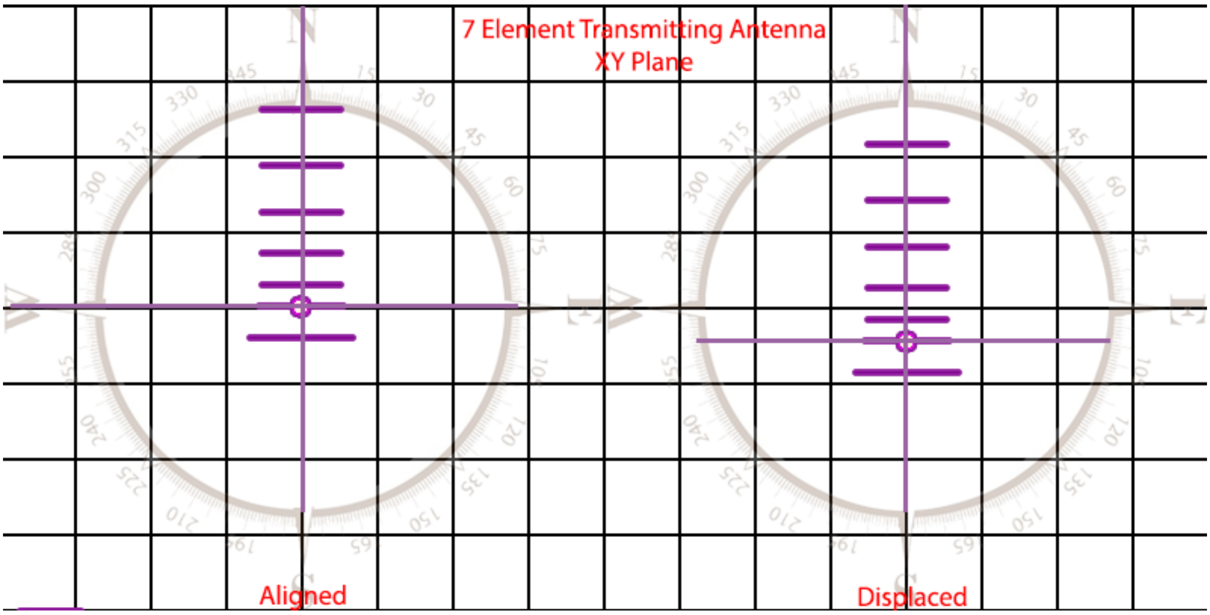

Figure 7-8: Analysing antenna position deviations from (left) as-mounted to (right) wind effected displacement, shown in the XY plane.

Using this method, and summing errors for the single receiving antenna, plus the two antennas comprising the illuminator, a worst case estimate is calculated for the phase across different wind speeds, as shown in Table 7-1.

Wind Speed (km/hr)	0.000	10.0	20.0	30.0	40.0
Phase Difference (radians)	0.000	0.086	0.172	0.23	0.343

Table 7-1: Wind speed effecting maximum displacement of repeating and receiving antennas and thus phase received (all values have been presented to 3 signficant figures).

At the worst deviation, the phase changes by 0.343 radians. The phase variation range calculated from the plots of Figure 7-3 through Figure 7-7 has been collated and shown in Table 7-2.

Date	20170817	20170901	20170914	20170921	20171006
Average Variation (radians)	0.257	0.837	0.103	0.203	0.435

***Table 7-2**: Average phase deviation observed from 17th August 2017 to 6 October 2017.*

The random deviations due to antenna bucking are in the same order as the phase variations recorded in measurement data, and therefore antenna drift evidently contributes as an unpredictable and unaccountable source of error.

The transmitting antenna for both direct and indirect paths is on a tower 145 m high. Whilst there is only 4.34 degrees between the illuminated and direct path from the transmitter, further phase change can be caused by the sway of the tower. Estimates from the Southern Cross Austereo (SCA) engineers that installed the antennas put this at ±1 degree both horizontally and vertically, depending on the wind speed (as shown in Table 7-3).

Wind Speed (km/hr)	0.000	10.0	20.0	30.0	40.0
Phase Difference (radians)	0.000	0.135	0.270	0.404	0.539

***Table 7-3**: Wind speed effecting maximum displacement of all antennas including transmission tower (all values have been presented to 3 signficant figures).*

7.3 Systematic Errors

7.3.1 BoM Data

The analysis of the NWP data for anticipated phase shifts (third figures in 6.3) used version APS1, ACCESS-C model for city analysis. This provided a resolution of approximately 4 km. The NWP models are run four times daily. More details can be found in [93]. At the time of writing, this was the highest resolution output available. However, the 4 km grids are not suited for searching within. The resolution is not sufficiently high to capture local weather effects and the result is overly smoothed gridded data. Further, the BoM National Computation Infrastructure (NCI) servers provide two sets of data, analysis (an) and forecast (fc). Unfortunately, the analysis data is exceedingly incomplete. The reasoning is that the forecast data at t = 0 hours encompasses the analysis. As mentioned, the NWP is run four times a day, specifically at 0000, 0600, 1200 and 1800 hrs UTC. The remaining 20 hours are calculated via the NWP forecast simulation. So whilst the t = 0 hours is of the shortest outlook and highest accuracy, t = +1 hours to t = +5 hours naturally suffer increasing with degrading accuracy.

The project avoided interpolating through time by obtaining measurements on the hours that the NWP was run (i.e. 0000, 0100, etc. UTC). However, the radio wave path required interpolation. This was accomplished by using bilinear (surface grid only) or trilinear (surface grid plus height data) interpolation.

The reality is the NWP output is established from a collection of sparse observations, fitted via global interpolation to a 4 km grid, and this project interpolates a path upon this gridded interpolation. For this reason, each day in Section 6.3 shows independent local observations at a point at Parafield airport. This point is situated several hundred metres away from the radio path, but provided an independent observation of the weather when compared to the NWP output. In all cases, the Parafield airport observational trends strongly agreed with NWP output despite not being at the same location.

7.3.2 Non-Collinear Paths

The time delay obtained in Section 6.3 gives the time between:

a) Transmitter -> Receiver, and,

b) Transmitter -> Repeater -> Receiver.

If the transmitter, receiver, and repeater are all collinear, then the time delay recorded is equivalent to a round trip between the receiver and the repeater and the time of flight over the path can be found by halving the time delay obtained. However, if the sites are not collinear, they will suffer a Cosine Error, similar to police speed radar instruments [94]. In this case, the refractivity profile is distorted slightly due to the horizontal displacements.

From Figure 3-4, the path was as near direct as topography allowed and only 4.34 degrees separated the direct and illumination paths. A closer examination at the midpoint area of the direct and illuminated paths is presented in Figure 7-9.

Figure 7-9: *Closer look at the repeated path displacement (image taken using Google Earth).*

As observed from Figure 7-9, the radio wave travels from the MidPtEnd to the Elizabeth Water Tower to the Adelaide Warbirds location. The BoM path refractivity is taken along the middle path, i.e. Elizabeth Water Tower to Midpoint. This discrepancy was unavoidable; however, its effect was minimised as the NWP output of 4 km grids contains this entire area, and causes a smoothed refractivity profile in this area.

7.3.3 Amplifier Delay Jitter

Upon reflection, the repeater chain was reanalysed. Initially measured and recorded as a constant 250 ns (5.4), the active elements in the repeater chain were remeasured for their group phase delays. Tested again on the same network analyser, the Agilent 8714ET RF, the delay was remeasured over a period of time. The previously 250 ns measured was an instantaneous value, but when remeasured over the period of 30 seconds, the range 249-251 ns was observed. These 2 ns variations would account for phase shifts of up to 1.26E-8 radians – not large enough to make an appreciable difference in the results.

The goal of this work included measuring the change in temperature over time. Amplifiers have different characteristics at different temperatures. So the repeater's 2 ns (measured in lab conditions) would increase in variation not only due to the diurnal weather changes, but also due to running permanently and also inside an enclosure. The datasheets of the Gali 74s and 84s used in the repeater chain do not specify the delay versus temperature curves, and replicating and measuring the running conditions is impractical. Conservatively estimating a factor of 100 of variation in delay results in phase shifts of 1.26E-6 radians, which is still much less than the variations seen in Section 7.1. Consequently, the active elements at the repeater did not appear to constitute as a source of error in the observations.

7.3.4 Path Distance

The path analysed is 5.25 km. This is much shorter than the original intention of the project which was hosting a receiver at UofA and having a 20 km path (this was unsuccessful as topography between illuminator and receiver attenuated the signal below the detection levels of the 16-bit receiver). Having a longer path would have lessened detrimental consequences due to local weather phenomenon, and would have provided potentially more discernible phase results at the cost of there being a wider region over which the refractivity was calculated. Using the propagation tool developed in Section 2, the path's vertical deviation due to atmospheric effects along the 5.25 km path was 0.0003 m or 0.2% of a cycle in calm conditions. Consequently, this research discovered that the path used is too short to reflect other data sources, but instead captured the localised refractive index changes.

7.4 Discussion Summary

This section has looked at the various causes of differences in results obtained from propagation observations when compared to estimates derived from BoM data sources. These differences affect the core hypothesis of the work – that is the measurable relationship between radio wave propagation and tropospheric weather. This thesis notes that the primary factor in these differences is local weather events that are not captured in BoM's NWP output and that longer paths are needed to average out these local weather effects.

8 Future Ideas

Learning from the outcomes of experimentation, future ideas are proposed to augment and extend the current work. Primary obstacles in this work were caused by the realities of obstructive terrain and unintended multipath. This section presents two possible improvements.

8.1 Hardware Enhancements – Broadband Phase Shifter

The Broadband Phase shifter (BPS) was designed early on to combat DSI. Employing a BPS will allow further path distances to be tested. It allows additional DSI to be removed before the ADC and hence lowers the dynamic range that is required by the ADC. This beamforming option is implemented through two antennas, one pointing towards the repeater and one towards the transmitter. As shown in Figure 8-1, a single computer controlled phase shift and amplitude adjustment is used to null out the direct signal [64].

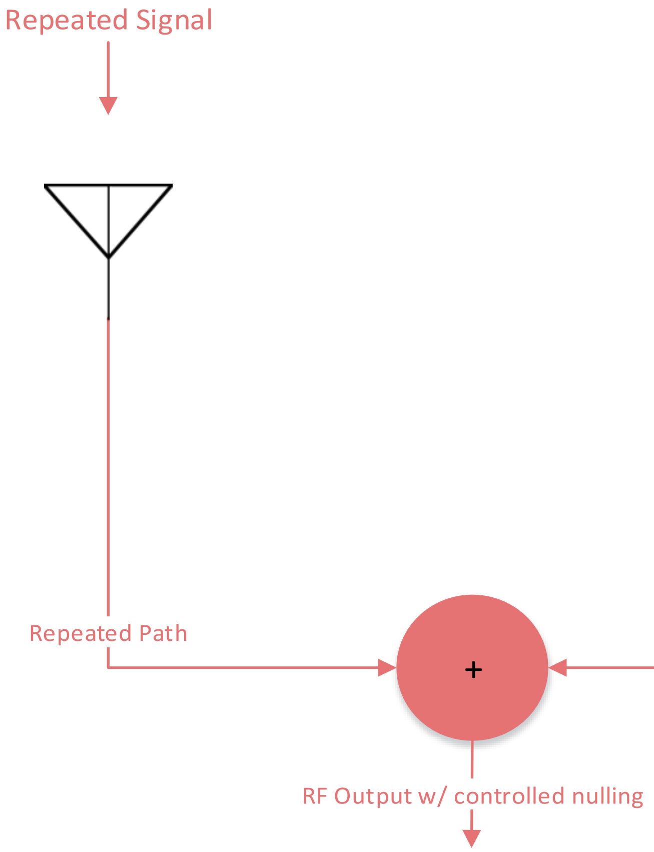

Figure 8-1: *Broadband Phase Shifter (BPS) controlling direct incident signal.*

The phase and amplitude adjustments are linked to a computer algorithm that analyses the received input and optimises the nulling based on certain metrics. The quantities to be optimised are the autocorrelation of the direct signal and the cross correlation of the direct and repeated signals (note that the signals are separated by a delay that is dependent upon the propagation path length). The goal of the BPS automated algorithm is to reduce the autocorrelation component as much as possible whilst maintaining a good signal to noise ratio on the cross correlation component. From an antenna radiation standpoint, this is akin to steering the main lobe towards the weaker signal, and steering nulls towards the stronger direct signal.

8.1.1 Broadband Phase Shifter

The BPS implements a variable coefficient phase attenuation to electronically steer the effective antenna radiation pattern and therefore control the power level of the received signal. Figure 8-2 illustrates an early prototype of the components necessary for a BPS.

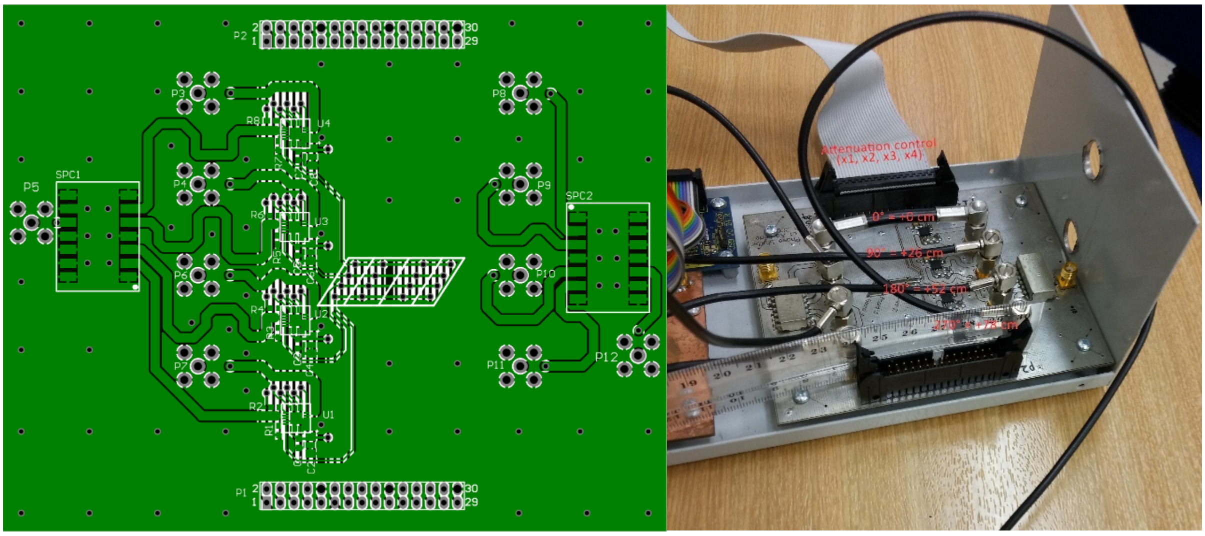

(a) (b)

Figure 8-2: Broadband Phase Shifter (BPS) implementation. (a) PCB view of the BPS. (b) Finished product of BPS after cable length measurements.

The BPS is comprised of a 4-way passive splitter (JS4PS-1W+) [95] at the input to separate the incoming RF into four phase lines; 0°, 90°, 180° and 270°. The phase line change is set by precise cable lengths for the channel at 204.64 MHz calculated from equations described in [96], resulting in lines of length +0, 26, 52, 78 cm respectively. RG-174 was used to support bending the cable within enclosures. Its dielectric insulator is made of solid polyethylene (PE) giving it a velocity factor of 66% of the speed of light [97] [98], thus allowing shorter cable construction. Each phase line is controlled by a variable attenuator (DAT-31R5-PP+) [99] receiving instructions via a PC host in form (x1, x2, x3, x4). The phase lines return to a 4-way passive combiner (JS4PS-1W+), enabling a full 360° control at less than 1° increments. If desired, the BPS could be used simply as a blanket attenuator by fully removing the signal allowed through three of the four phase lines. For further details about design choices, see [64].

Figure 8-3 shows some results from the prototype BPS unit for two sets of input: blue at (0, 32, 32, 32) dB attenuation, and orange at (32, 32, 32, 0) dB. Other mixed combinations of (x1, x2, x3, x4) are possible, but those shown in Figure 8-3 illustrate the functioning of the phase shifter.

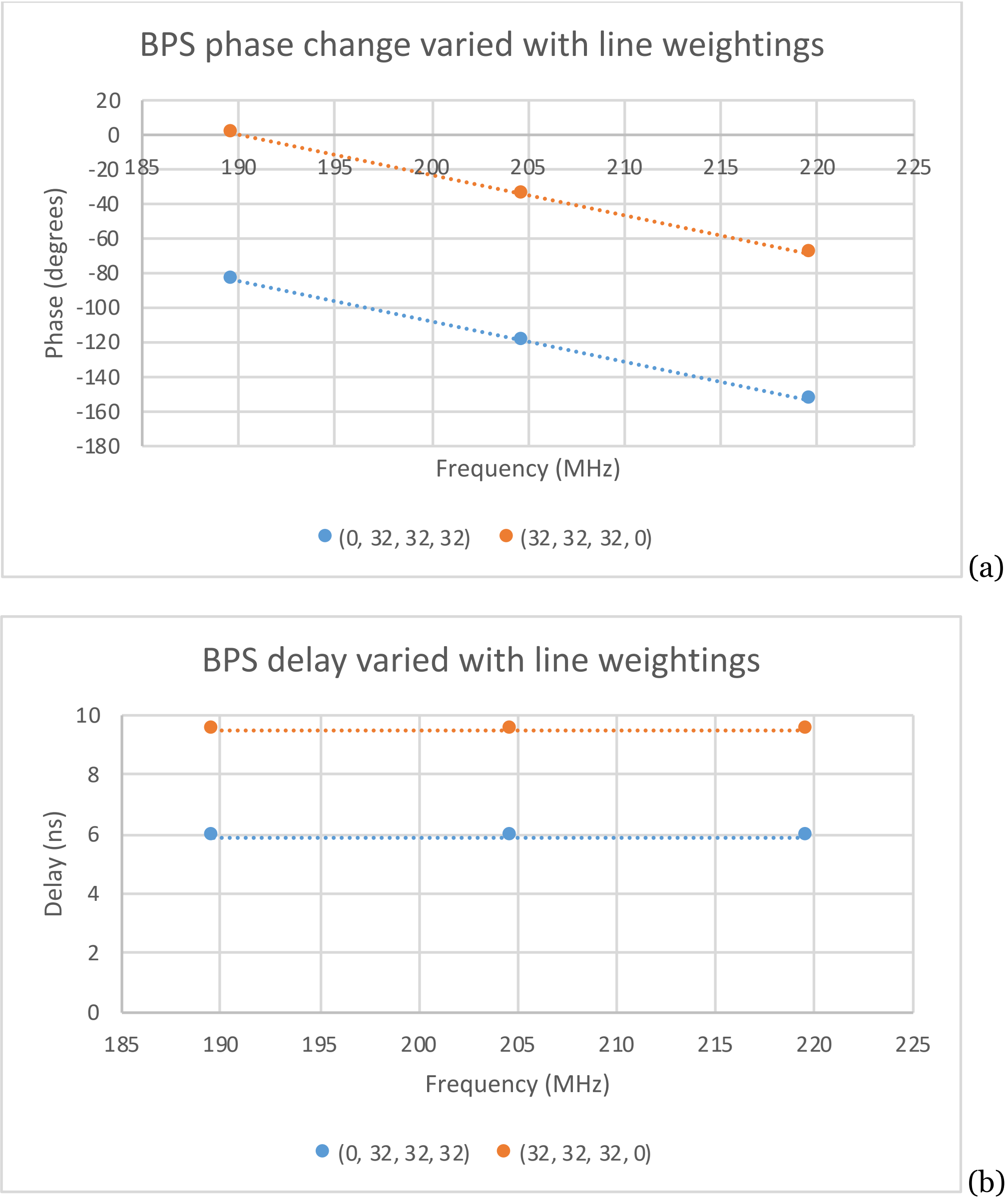

Figure 8-3*: Demonstration of the Broadband Phase Shifter (BPS) at different inputs. (a) Phase, (b) Delay.*

The delays shown in Figure 8-3a indicate the maximum difference of about 4 ns between the minimal and maximal length lines.

8.1.2 Combiner and Controlled Amplifier

The combiner is responsible for merging two separate antenna signals into one (e.g. merging one antenna trained on the direct path and the other on the repeated signal). After combination, the signals are controllably amplified to enable undistorted detection of both paths in the analogue to digital converter and with the highest possible level for the weakest signal.

A JPS-2-1 [100] is used to combine the two signals with a low insertion loss of less than 0.25 dB. A DVGA2-33PP+ [101] is a Digital Variable Gain Amplifier (DVGA) controlled in 0.5 dB steps from -12 dB to +19 dB. This is used to provide amplification of the signal prior to it being taken to the digital domain, but only up to a level which avoids the signal clipping. Figure 8-4 shows the board designed to implement combiner and controlled amplifier.

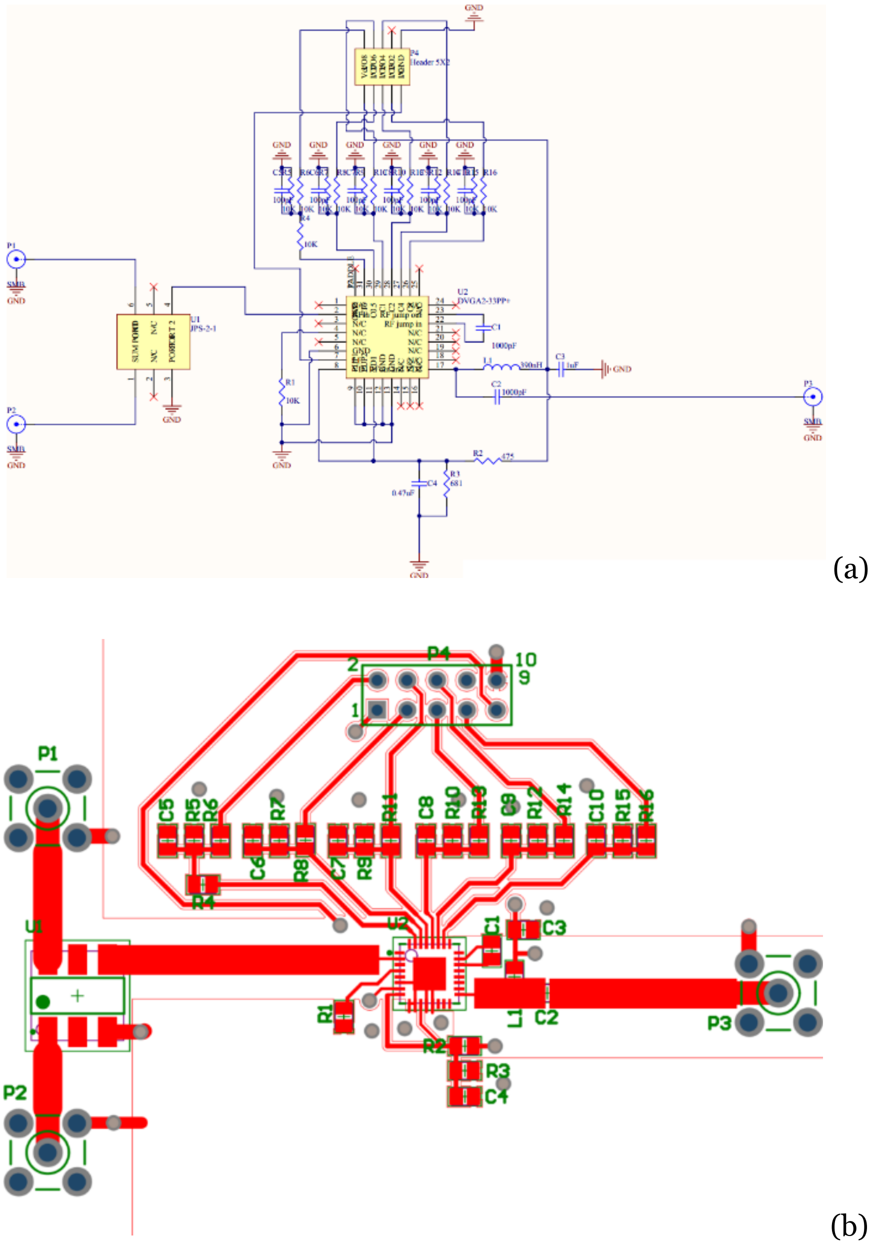

***Figure 8-4**: Design of step amplifier with combiner PCB (a) schematic and (b) PCB footprint.*

The board depicted in Figure 8-4 takes care to use microstrip lines of sufficient width to maintain a 50 Ω characteristic impedance to reduce loss due to mismatch. The board is double sided, with the bottom layer being a ground plane with through board holes.

Testing the DVGA/splitter board required two signal generators and a spectrum analyser. The Device Under Test (DUT) is connected and controlled via the USB controller. For the test shown in Figure 8-5, both signal generators were set 2 MHz apart, and at -40 dBm. The DVGA amplitude was set to zero to minimise influences on the test, but still provided its noise characteristics.

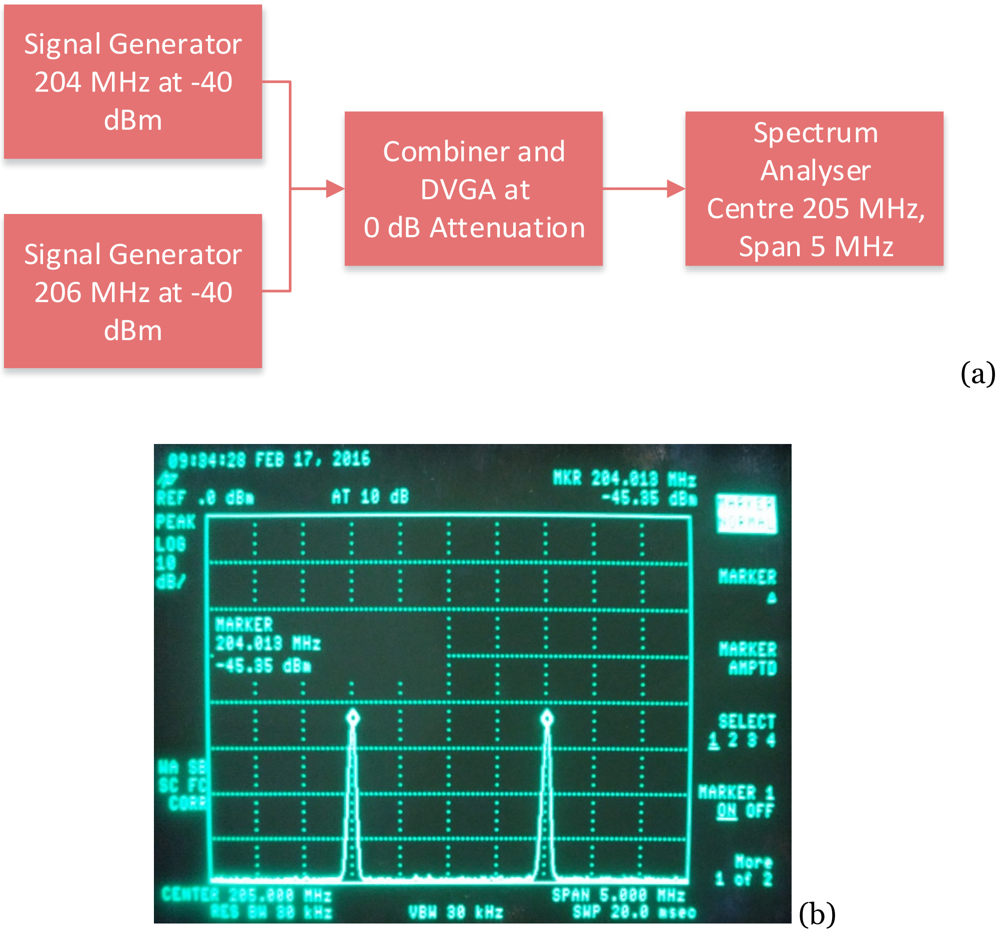

Figure 8-5: *Testing the Digital Variable Gain Amplifier (DVGA) with two signal-generated inputs. (a) Test set up with combiner and varying attenuation. (b) Output of board splitting (reversing combination) at the 0 dB gain.*

The device performs as expected, providing almost 50% input power (expecting -43 dBm, and achieving -45 dBm) for the two split signals. The 2 dB discrepancy is explained by the insertion loss of the components (≈0.75 dB) and cables (≈1 dB).

8.1.3 USB Controller

Continuous feedback to the BPS and DVGA is facilitated with a USBIO24 R Digital I/O Module [102]. This device processes decisions made on the PC into suitable electronic signal lines for the PCB's containing the devices to be continually adjusted. It is used for its simple serial input and powered solely by the USB 5V supply, shown in Figure 8-6.

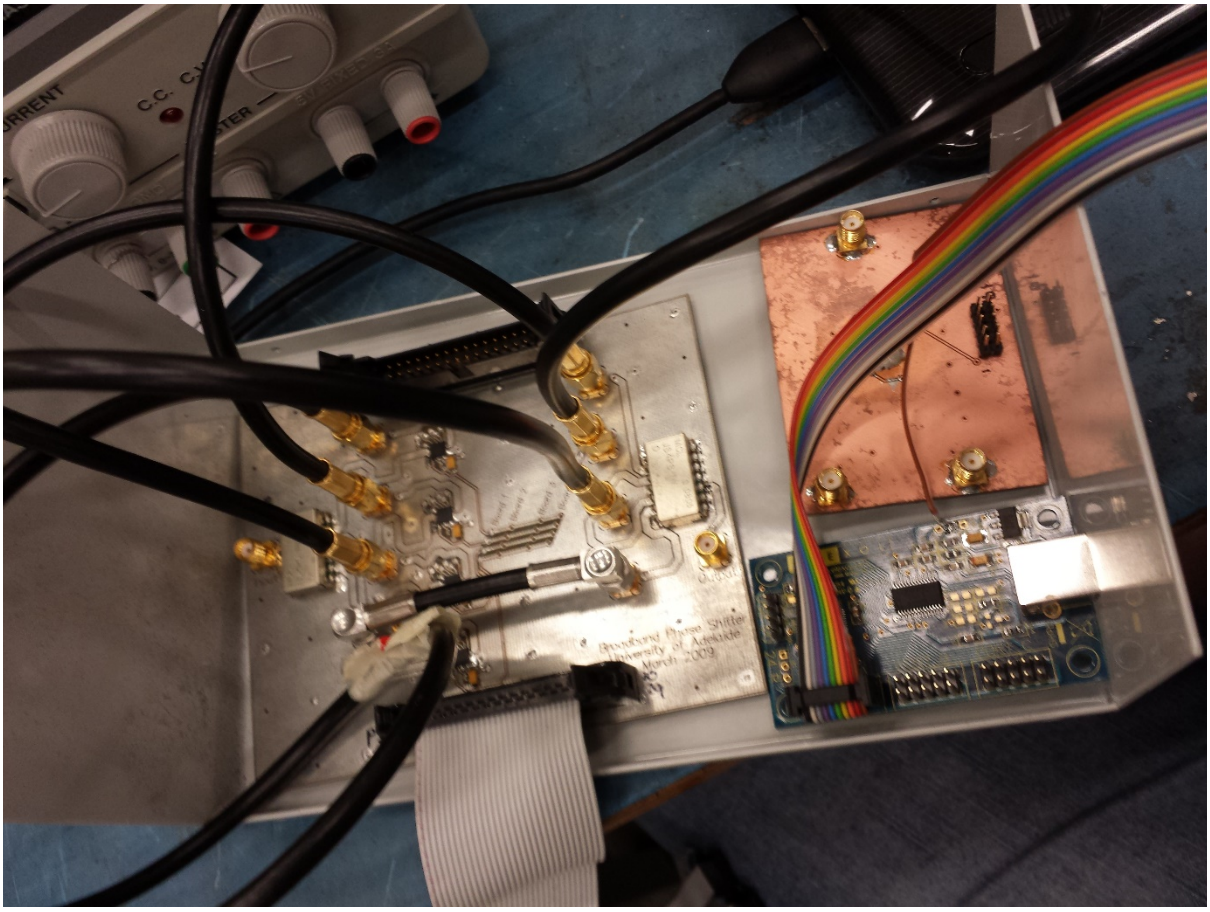

***Figure 8-6**: Broadband Phase Shifter (BPS), combiner/Digital Variable Gain Amplifier (DVGA), and USB Input Output (USBIO) are insulated by a metal casing (lid not pictured) suitable for long term-term use.*

8.2 Frequency Multiplying

The general idea behind the method presented in this thesis is that it compares copies of the same transmitted signal. However, this brings with it the major problem of DSI. Instead of the repeater retransmitting the received signal on the same frequency ($f_{in} = f_{out}$), an extension is retransmit the signal on a different frequency. Regular frequency translation requires an oscillator, which introduces timing issues in the relative measurements. Simply doubling (herein denoted X2 or $2f_{in}$), tripling (X3 or $3f_{in}$), or other integer factors of the base frequency only requires a passive device and hence permits the system to avoid further timing complications. Furthermore, the approach also avoids the problem associated with interference from feedback in the repeater.

The previously discussed repeater implementations use single frequency amplifiers, which can cause feedback if the input is not sufficiently isolated from the output. Whilst cross polarisation, antenna separation, and structural isolation have already been utilised to enhance isolation in the repeater set up, separation in frequency could greatly increase the achievable isolation. With suitable filtering, the repeater can now retransmit at higher powers and hence reduce the dynamic range problems of the single frequency system.

The choice of frequency tripling specifically is derived from the nature of spectrum allocation in Australia. Shown in Figure 8-7 is the Australian RF spectrum assignments (edited for VHF/UHF only) from the ACMA [103].

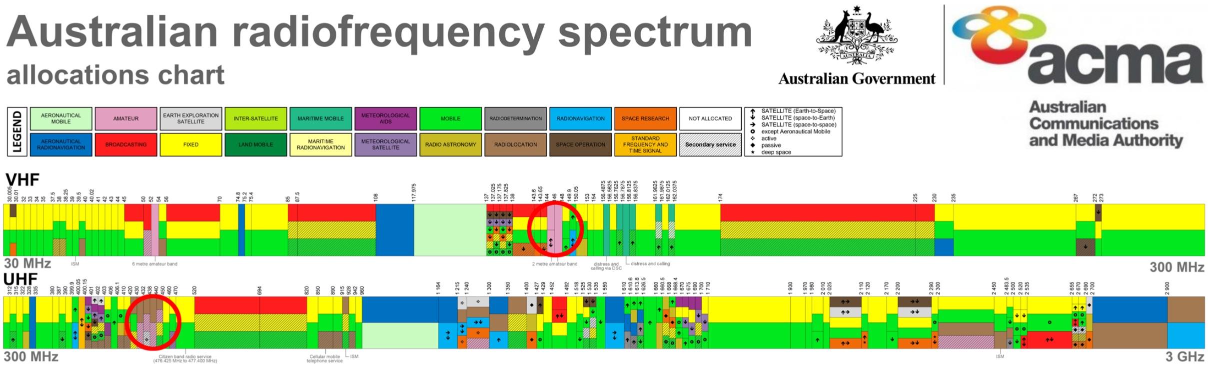

Figure 8-7: Spectrum Allocation in Australia provided by the Australia Communications and Media Authority (ACMA – unmodified, full size poster available at https://www.acma.gov.au/theacma/australian-radiofrequency-spectrum-plan-spectrum-planning-acma, saved in 2014). Circled are two potential bands suitable for frequency multiplication (70 cm and 2 m wavelengths).

There are two amateur bands shown in Figure 8-7 within the VHF/UHF spectrum at 70 cm and 2 m wavelengths, which through adequate frequency filtering could facilitate specifically using frequency tripling. Several transmitters of opportunity exist within the amateur bands (repeaters and beacons) and could be utilised (along with dedicated amateur broadcasts).

8.2.1 How it Works

Frequency multipliers are non-linear devices that generate the desired harmonic frequency of its input whilst suppressing other harmonics, including the fundamental harmonic. Principally, the multiplier is a comb generator with attenuation at all frequencies other than the desired output. When used for retransmission, however, these devices will provide good filtering to remove out of band harmonics.

8.2.2 Design for Frequency Tripler at Repeater

In designing a frequency tripler for the repeater of DAB terrestrial services, there are many suitable products on the market capable of this task in both coaxial and surface mount options. Surface mounting is preferred as the form factor is minimised. A suitable component is the RMK 3-92+ from Mini-Circuits [104]. This multiplier has 14 dB conversion loss and accepts input power from 12-17 dBm. The RMK 3-92+ is a passive device requiring no power, and a PCB design is shown in Figure 8-8.

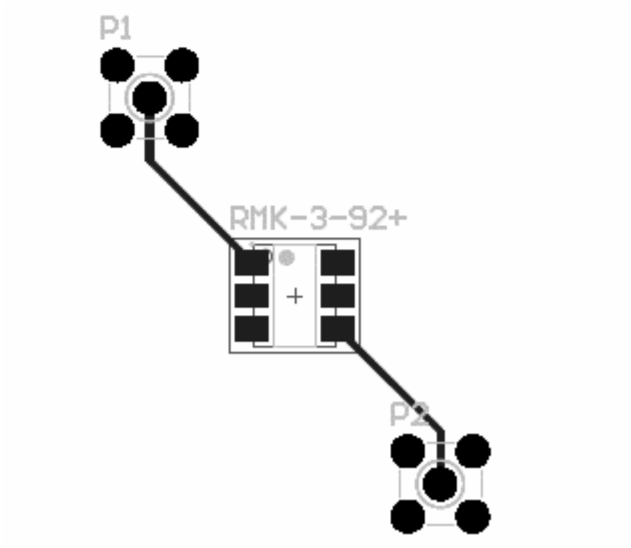

Figure 8-8: Basic PCB footprint for the X3 frequency multiplier only uses a single integrated circuit with input and output.

The PCB design in Figure 8-8 features a simple design with SMA output and inputs using two ports of the multiplier (the remaining pins are grounded). However, the strict limits of input power (12-17 dBm) specified by the RMK 3-92+ datasheet necessitate fine control over the input power. The conversion loss of the device may also dictate amplification post-multiplication.

Fortunately, the DVGA discussed in 8.1.2 can be repurposed for this required precise amplification at the multiplier input. Anti-alias filtering at the repeater is unchanged. The transmitting antenna would need to be replaced with a different model Yagi-Uda, (preferably by the same company, Polar Electronics), which is suitable for the new transmitting frequency. The repeating chain would be adjusted as shown in Figure 8-9.

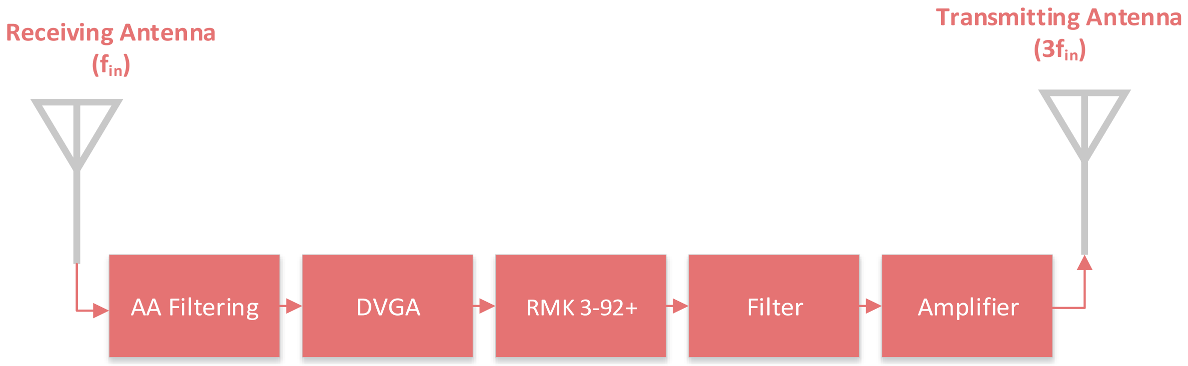

***Figure 8-9**: Repeater chain modified to include frequency multiplication.*

This new repeating chain differs from the basic diagram shown in Section 4.1 due to a change in transmitting antenna and the addition of a frequency multiplier (and a following amplifier and filter). The DVGA can be calibrated in-situ to suit the received signal power level, but with only 5 dBm tolerance at the input; a more robust approach with live feedback is required to deal with input power fluctuations. A low powered, small, and transportable computer is required that reads the multiplier's input and adjust amplification accordingly. Figure 8-10 illustrates the feedback mechanism.

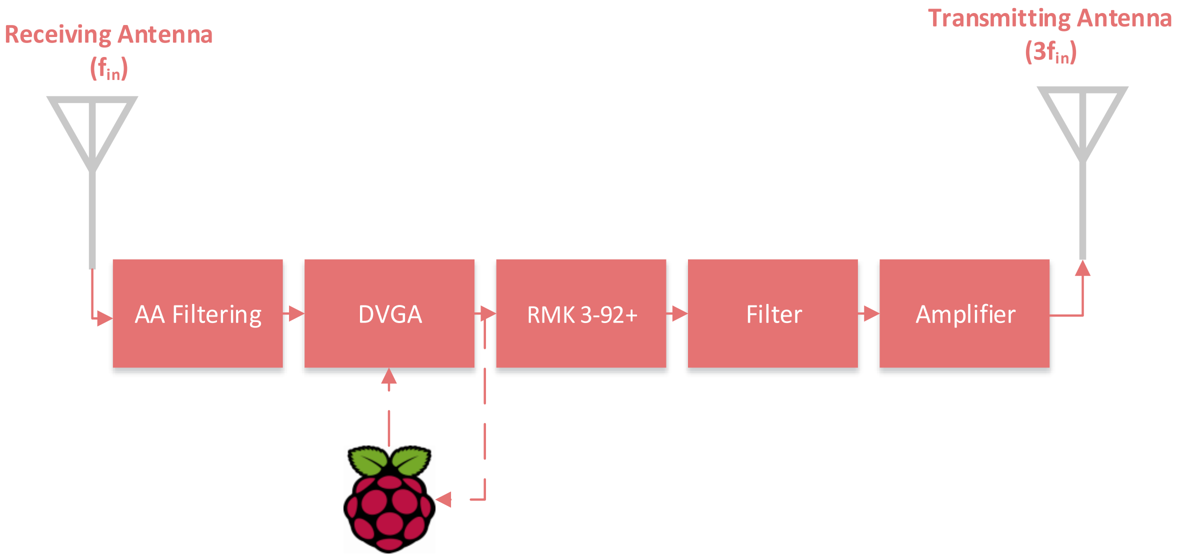

***Figure 8-10**: Repeater chain including frequency multiplication introduces a Raspberry Pi Zero to facilitate control of signal amplification.*

A Raspberry Pi Zero is a low powered device (≈80 mA) with General Purpose Input Output (GPIO) pins, required to read from the input wire of the multiplier, as well as a USB interface to control the DVGA gain. The Raspberry Pi Zero runs off a Debian distribution with mainline Linux kernel. It is possible to run MATLAB embedded ARM code, but more likely Python scripts, which interface with the DVGA's USB control. It is reprogrammable and versatile in a small form factor. These scripts read the voltage values of the GPIO pins (wired to the multiplier input) at an interval of 0.25 seconds and adjust the gain by referencing a custom predefined curve which aims at keeping the input signal of the multiplier between the minimum and maximum values defined in its datasheet.

8.2.3 Receiver Considerations Due to Frequency Tripling

The new transmission frequency of the repeater means modifications to the receiving equipment are required. To maintain the phase relationship required in the relative measurements, the direct signal needs to be tripled, and two synchronised channels of the ADC require new frequency filtering centred at the tripled frequency. The receiving antenna is also replaced with the same Yagi-Uda antenna at the repeater, suitable for the shift in frequency. Figure 8-11 shows how the receiving equipment changes to account for frequency tripling.

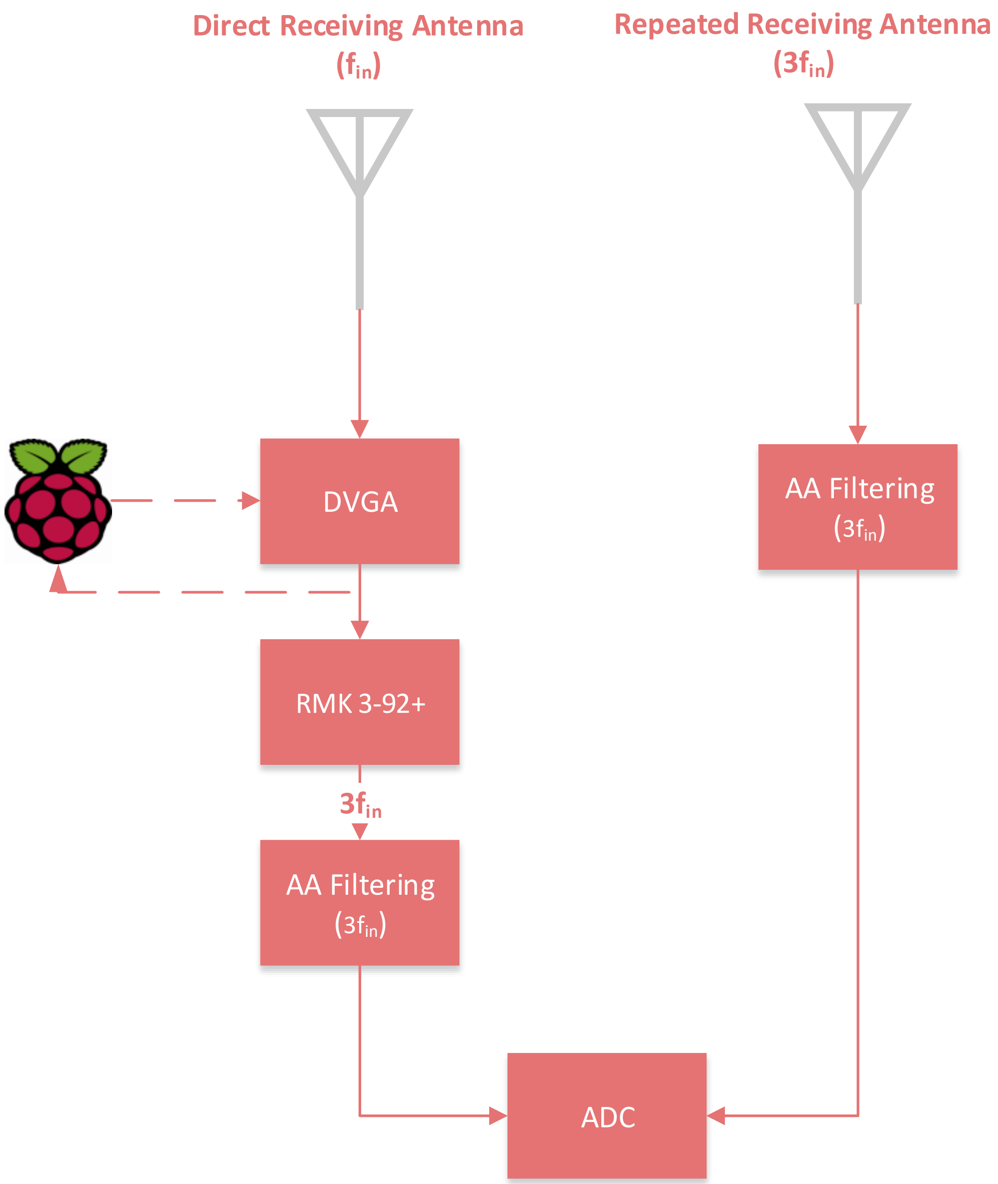

Figure 8-11*: Receiver changed to implement the frequency tripling changes.*

Note that at the ADC, the equipment in Figure 8-11 produces two signals of the same frequency, using the same passive tripler as in the repeater, and relative phase measurements can be made using the same procedure as for the original system.

8.3 Future Ideas Summary

This chapter has proposed two detailed approaches to combat issues encountered through the course of research. With these approaches alone, further path distances would be obtainable and topographical complexities mitigated.

9 Conclusion

This research has investigated whether VHF radio wave propagation can be used to infer information about the weather. This idea is based on the connection that exists between weather and the refractive index of air. GPSRO has previously shown the link for the upper atmosphere, and continues to be used to obtain refractivity profiles across large distances. This current work has continued the only very recently renewed effort on the tropospheric weather and radio wave propagation link. Building on previous works incorporating signals of opportunity, a unique approach was developed using a cooperative radar target within the context of a bistatic radar system.

During the research, the project has developed a new radio wave path propagation tool to investigate how true radio wave propagation is affected by refractive index variations in the lower troposphere based on Fermat's principle of least time. The scope of this tool may be further developed to account for emerging adjacent research areas, including passive radar systems. Of significance, this work has shown that variations in weather can cause measurable phase changes between the transmitter and receiver.

Based upon these observations, the second part of this project has been to see if observations of variations in phase can be used to infer information about the weather. The project has used a signal of opportunity, a DAB broadcast, and acknowledging timing limitations from previous endeavours, has used a radar technique that is based upon the principles of bistatic passive radar. To make this procedure possible required the development of an artificial radar target, the repeater. As with true passive radar, direct signal interference was a major problem and much of this work has involved the development of techniques for overcoming this significant problem. The equipment developed by this project has been used to take the measurements over short paths and experiments have shown that there are variations in the phase of the expected order. Unfortunately, it was evident that the localised weather and antenna sway contaminated results to such a degree that makes radio wave measurements over short ranges unsuitable for inferring weather. The resulting outcome was that the techniques devised during this research are more suited for longer paths, and the path analysed was too short to compare the radio path measurements against independent BoM data. Early modelling and simulations did not, and could not, consider the complete subtleties of the physical world, and therefore the importance of the longer path was not apparent. However, the radio measurements do contain localised weather effects not present in BoM data. Future refinements of this research's techniques will expectedly turn this result of incomparable datasets into a method to increase the fidelity of the NWP weather model incorporating these localised effects.

The work undertaken was fraught with delays and setbacks, with significant difficulties in obtaining data due to availability of suitable sites and ironically due to poor weather. However, the results and dissection of the results should prove invaluable to future researchers in the area.

This work of this thesis suggests that the use of radio propagation for inferring weather is certainly worth pursuing, especially using some of the ideas suggested in Section 8.2. However, much longer propagation distances than those that could be achieved in this work need to be used for obtaining further results. There is an undeniable link shown and recorded within the data that matches the hypothesis stating there exists a measurable influence that tropospheric weather has on terrestrial radio wave propagation. Using the experimental lessons learnt from this work's particular methodology, hardware, and topographical setup, future efforts in this research area will confidently be more successful.

References

[1] E. Hecht, Optics Fourth Edition, San Francisco: Addison Wesley, 2002.

[2] S. Padmanabhan, S. Reising, J. Vivekanandan and F. Iturbide-Sanchez, “Retrieval of atmospheric water vapor density with fine spatial resolution using three-dimensional tomographic inversion of microwave brightness temperatures measured by a network of scanning compact radiometers,” *Geoscience and Remote Sensing, IEEE Transactions on,* vol. 47, no. 11, pp. 3708-3721, 2009.

[3] E. F. K. Zhang, D. Silcock, Y. Wang and Y. Kuleshov, “An investigation of atmospheric temperature profiles in the Australian region using collocated GPS radio occultation and radiosonde data,” *Atmospheric Measurement Techniques,* vol. 4, no. 10, pp. 2087-2092, 2011.

[4] N. Crook, “Sensitivity of moist convection forced by boundary layer processes to low-level thermodynamic fields,” *Monthly Weather Review,* vol. 124, pp. 1767-1785, 1996.

[5] M. Bevis, S. Businger, T. Herring, C. Rocken, R. Anthes and R. Ware, “GPS meteorology-Remote sensing of atmospheric water vapor using the Global Positioning System,” *Journal of Geophysical Research,* vol. 97, pp. 15787-15801, 1992.

[6] O. Davies, C. Mitchell, P. Spencer, J. Nash, R. Watson and P. Watson, “Application of GPS phase delay measurements in radio science and atmospheric studies,” *IEE Proceedings - Microwaves, Antennas and Propagation,* vol. 151, no. 1, pp. 1-6, 2004.

[7] R. Ware, C. Alber, C. Rocken and F. Solheim, “Sensing integrated water vapor along GPS ray paths,” *Geophysical Research Letters,* vol. 24, no. 4, pp. 417-420, 1997.

[8] H. v. d. Marel, “Exploitation of Ground Based GPS for Numerical Weather Prediction and Climate Applications in Europe,” *Vistas for Geodesy in the New Millennium,* vol. 125, pp. 297-302, 2001.

[9] R. J. Watson and C. J. Coleman, “The use of signals of opportunity for the measurement of atmospheric refractivity,” in *Fourth European Conference on Antennas and Propagation*, Barcelona, Spain, 2010.

[10] S. Healy and J. Eyre, “Retrieving temperature, water vapour and surface pressure information from refractive-index profiles derived by radio occultation: A simulation study,” *Quarterly Journal of the Royal Meteorological Society,* vol. 126, no. 566, pp. 1661-1683, 2000.

[11] R. Anthes, “Exploring earth's atmosphere with radio occultation: contributions to weather, climate and space weather,” *Atmospheric Measurement Techniques,* vol. 4, pp. 135-212, 2011.

[12] J. Herbstreit and M. Thompson, “Measurements of the phase of signals received over transmission paths with electrical lengths varying as a result of atmospheric turbulence,” *Antennas and Propagation, IRE Transactions on,* vol. 4, no. 3, pp. 352-358, 1956.

[13] D. Gray, “Transit-time variations in line-of-sight tropospheric propagation paths,” *Bell System Technical Journal,* vol. 49, no. 6, 1970.

[14] C. J. Coleman, R. Watson and H. Yardley, “A practical bistatic passive radar system for use with DAB and DRM illuminators,” in *IEE Radar Conference*, Rome, Italy, 2008.

[15] The International Institute for Aerospace Survey and Earth Sciences, Principles of Remote Sensing, Enschede, The Netherlands: The International Institute for Aerospace Survey and Earth Sciences, 2001.

[16] J. B. Campbell and R. H. Wynne, Introduction to Remote Sensing, Fifth Edition, New York: Guilford Press, 2011.

[17] P. F. Kisak, Synthetic Aperture Radar, CreateSpace Independent Publishing Platform, 2015.

[18] P. Dong and C. Qi, LiDAR Remote Sensing and Applications, Boca Raton, FL: CRC Press, 2017.

[19] R. J. Jensen, Remote Sensing Of The Environment, Pearson Prentice Hall, 2007.

[20] R. Ware, C. Rocken, M. Exner, D. Feng, B. Herman, M. Gorbunov, K. Hardy, Y. Kuo, T. Meehan and W. Melbourne, “GPS sounding of the atmosphere from low Earth Orbit: Preliminary results,” *Bulletin of the American Meteorological Society,* vol. 77, pp. 19-40, 1996.

[21] A. Kliore, D. L. Cain, G. S. Levy, V. R. Eshleman, G. Fjeldbo and F. D. Drake, “Occultation experiment: Results of the first direct measurement of Mars' atmosphere and ionosphere,” *Science,* vol. 149, no. 3689, pp. 1243-1248, 1965.

[22] G. A. Hajj, B. Iijima, C. Ao, D. Kuang, E. Kursinski, A. Mannucci, T. Meehan, L. Romans, M. de La Torre Juarez and T. Yunck, “CHAMP and SAC-C atmospheric

occultation results and intercomparisons," *Journal of Geophysical Research,* vol. 109, no. D6, p. D06109, 2004.

[23] J. Wickert, C. Reigber, G. Beyerle, R. Konig, C. Marquardt, T. Schmidt, L. Grunwaldt, R. Galas, T. K. Meehan and W. G. Melbourne, "Atmosphere sounding by GPS radio occultation: First results from CHAMP," *Geophys. Res. Lett,* vol. 28, no. 17, pp. 3263-3266, 2001.

[24] C. Dunn, W. Bertiger, G. Franklin, I. Harris, G. Kruizinga, T. Meehan, S. Nandi, D. Nguyen, T. Rogstad and J. B. Thomas, "The instrument on NASA's GRACE Mission: Augmentation of GPS to achieve unprecedented gravity field measurements," 2002.

[25] J. Wickert, T. Schmidt, G. Beyerle, G. Michalak, R. Konig, S. Heise and C. Reigber, "GPS radio occultation with CHAMP and GRACE: Recent results," *Atmosphere and Climate,* pp. 3-16, 2006.

[26] R. Anthes, P. Berhardt, Y. Chen, L. Cucurull, K. Dymond, D. Ector, S. Healy, S. Ho, D. Hunt and Y. Kuo, "The COSMIC/Formosat-3 mission," *B. Am. Meteorol. Soc,* vol. 89, pp. 313-333, 2008.

[27] P. Wilczynski and K. C, "COSMIC-2: Weather Forecasting and Space Weather Monitoring in the 21st Century," *Earthzine,* 2010.

[28] W. G. Melbourne, E. David, C. Duncan, G. Hajj, K. Hardy, E. Kursinski, T. Meehan, l. Young and T. Yunck, "The Application of spaceborne GPS to atmospheric limb sounding and global change monitoring," JPL Publication, California, 1994.

[29] S. Ho, Y. Kuo, W. Schreiner and X. Zhou, “Using SI tracable global positioning system radio occultation measurements for climate monitoring,” *BAMS,* pp. 536-537, 2010.

[30] S. Healy, A. Jupp and C. Marquardt, “Forecast impact experiment with GPS radio occultation measurements,” *Geophysical Research Letters,* vol. 32, no. 3, p. L03804, 2005.

[31] C. Y. Huang, Y. H. Kuo, S. H. Chen and F. Vandenberghe, “Improvements in typhoon forecasts with assimilated GPS occultation refractivity,” *Weather and forecasting,* vol. 20, pp. 931-953, 2005.

[32] E. Kursinski, G. Hajj, J. Schofield, R. Linfield and k. Hardy, “Observing Earth's atmosphere with radio occultation measurements using the Global Positioning System,” *Journal of Geophysical Research,* vol. 102, no. D19, pp. 23429-23465, 1997.

[33] F. Pelliccia, F. Pacifici, S. Bonafoni, P. Basili, N. Pierdicca, P. Ciotti and W. J. Emery, “Neural Networks for Arctic Atmosphere Sounding From Radio Occultation Data,” *Geoscience and Remote Sensings, IEEE Transactions,* vol. 49, no. 12, pp. 4846-4855, 2011.

[34] S. Kawamura, S. Ohta, H. Hando, M. Yamamoto, N. Shiga, K. Kido, S. Yasuda, T. Goto, R. Ichikawa, J. Amagi, K. Imamura, M. Fujieda, H. Iwai, S. Sugitani and T. Iguichi, “Water vapor estimation using digital terrestrial broadcasting waves,” *Radio Science,* vol. 52, no. 3, 2017.

[35] E. Smith and S. Weintraub, “The constants in the equation for atmospheric refractive index at radio frequencies,” *Proceedings of the IRE,* vol. 41, no. 8, pp. 1035-1037, 1953.

[36] G. Thayer, "An improved equation for the radio refractive index of air," *Radio Science,* vol. 9, no. 10, pp. 803-807, 1974.

[37] S. Skone and V. Hoyle, "Troposphere modelling in a regional GPS network," *Journal of Global Positioning Systems,* vol. 4, no. 1-2, pp. 230-239, 2005.

[38] A. Flores, J. V. G. De Arellano, L. P. Gradinarsky and A. Rius, "Tomography of the lower troposphere using a small dense network of GPS receivers," *Geoscience and Remote Sensing, IEE Transactions on,* vol. 39, pp. 439-447, 2001.

[39] MET Office, "The UKV model - Kilometre-scale forecasting over the UK with the Unified Model," [Online]. Available: http://www.metoffice.gov.uk/research/news/ukv. [Accessed 20 November 2012].

[40] MET Office, "Met Office Numerical Weather Prediction Models," [Online]. Available: http://www.metoffice.gov.uk/research/modelling-systems/unified-model/weather-forecasting. [Accessed 12 November 2012].

[41] A. K. Ghatak, Optics 4th Edition, Madipur, New Delhi: Tata McGraw-Hill Education, 2006.

[42] Geo Engine, "NGA Raster Roam," 2005. [Online]. Available: http://geoengine.nga.mil/geospatial/SW_TOOLS/NIMAMUSE/webinter/rast_roam.html. [Accessed 23 11 2012].

[43] M. Hall, Effects of the troposphere on radio communication, The Institution of Electrical Engineers, London and New York, 1980.

[44] S. Ackerman and J. Knox, Meteorology - Understanding the Atmosphere, California: Thomson Brooks/Cole, 2007.

[45] R. Descartes and P. J. Olscamp, Discourse on method, optics, geometry, and meteorology, Indianapolis: Hackett Publishing Company, 2001.

[46] National Geospatial-Intelligence Agency, "NGA Raster Roam," 2005. [Online]. Available: http://geoengine.nga.mil/geospatial/SW_TOOLS/NIMAMUSE/webinter/rast_roam.html. [Accessed 20 November 2012].

[47] M. Chernaikov, Bistatic Radars: Emerging Technology, West Sussex: John Wiley & Sons, 2008.

[48] ACMA, "Adelaide RA1," 2013. [Online]. Available: http://www.acma.gov.au/licplan/defmaps/documents/maps/la_499.pdf. [Accessed 14 April 2014].

[49] C. Coleman and H. Yardley, "Passive bistatic radar based on target illuminations by digital audio broadcasting," *IET Radar, Sonar and Navigation,* vol. 2, no. 5, pp. 366-375, 2008.

[50] ACMA, "LIPD Class License," October 2013. [Online]. Available: http://www.acma.gov.au/Industry/Spectrum/Radiocomms-licensing/Class-licences/lipd-class-licence-spectrum-acma. [Accessed 14 March 2014].

[51] ACMA, "Digital Radio Accessibility," ACMA, 24 October 2013. [Online]. Available: http://www.acma.gov.au/Industry/Broadcast/Spectrum-for-broadcasting/Broadcast-planning/digital-radio. [Accessed 15 April 2014].

[52] M. Brooks, 26 January 2006. [Online]. Available: http://www.ee.ic.ac.uk/hp/staff/dmb/courses/dab/dab_6.pdf. [Accessed 22 January 2015].

[53] H. Stenn, "The NTP Public Services Project," 2 February 2014. [Online]. Available: http://support.ntp.org/bin/view/Main/WebHome. [Accessed 23 January 2015].

[54] R. M. Hambly and T. A. Clark, "Critical evaluation of the Motorola M12+ GPS timing receiver vs. the master clock at the United States Naval Observatory, Washington, DC," *Syntonics LLC Columbia MD,* pp. 109-116, 2002.

[55] S. S. Saunders and S. R, "Factors influencing outdoor to indoor radio wave propagation," Exeter, UK, 2003.

[56] L. Besse and R. Gilmore, Practical RF Circuit Design for Modern Wireless Systems, Volume 1, Norwood, MA: Artech House, 2003.

[57] ACMA, April 2013. [Online]. Available: http://www.acma.gov.au/webwr/_assets/main/lib100059/stations_book_electronic_edition.pdf. [Accessed 5 November 2013].

[58] K. Malaric, EMI Protection for Communication Systems, Norwood, MA: Artech House, 2009.

[59] H. T. Friis, "A note on a simple transmission formula," *proc. IRE,* vol. 34, no. 5, pp. 254-256, 1946.

[60] Granite Island Group, "Technical Surveillance Counter Measures," 2010. [Online]. Available: http://www.tscm.com/2waybi.pdf. [Accessed 29 January 2015].

[61] W. L. Stutzman and G. A. Thiele, Antenna Theory and Design, John Wiley & Sons, 2012.

[62] J. H. Reisert, "Antenna Polarization," Astron Wireless Technologies, [Online]. Available: http://www.astronwireless.com/topic-archives-antennas-polarization.asp. [Accessed 24 April 2014].

[63] A. Henrik, J.-E. Berg, F. Harrysson, J. Medbo and M. Riback, “Propagation characteristics of polarized radio waves,” in *IEEE 66th Vehicular Technology Conference*, Baltimore, MD, USA, 2007.

[64] J. E. Hudson, Adaptive Array Principles, Exeter: The Institution of Electrical Engineers, London and New York, 1981.

[65] ACMA, “LIPD Class Licence,” 27 August 2014. [Online]. Available: http://www.acma.gov.au/Industry/Spectrum/Radiocomms-licensing/Class-licences/lipd-class-licence-spectrum-acma. [Accessed 1 October 2014].

[66] Mini-Circuits, “Monolithic Amplifier - Gali 74,” [Online]. Available: http://www.minicircuits.com/pdfs/GALI-74+.pdf. [Accessed 8 January 2016].

[67] Mini-Circuits, “Monolithic Amplifier - Gali 84,” [Online]. Available: www.minicircuits.com/pdfs/GALI-84+.pdf. [Accessed 29 January 2016].

[68] Temwell, “VHF UHF Helical Filter Specification Sheet,” [Online]. Available: http://www.temwell.com.tw/TF8929B1-201M.htm. [Accessed 8 January 2016].

[69] R. J. M. II, Introduction to Shannon Sampling and Interpolation Theory, New York: Springer-Verlag, 1991.

[70] Analog Devices, Inc, Linear Circuit Design Handbook, Newnes, 2011.

[71] P. Burns, Software Defined Radio for 3G, Norwood, MA: Artech House, 2003.

[72] Linear Technology, “LTC2207,” [Online]. Available: http://cds.linear.com/docs/en/datasheet/22076fc.pdf. [Accessed 7 June 2016].

[73] Opal Kelly, “XEM3010 User's Manual,” [Online]. Available: http://assets00.opalkelly.com/library/XEM3010-UM.pdf. [Accessed 8 January 2016].

[74] OsmoSDR, “OsmocomSDR,” 2014. [Online]. Available: http://sdr.osmocom.org/trac/wiki/rtl-sdr. [Accessed 1 July 2015].

[75] Polar Electronics, “Polar Electronics - Model 225,” [Online]. Available: http://www.polarelectronicindustries.com/model.php/model_id/228/. [Accessed 1 December 2015].

[76] G. Burke, “Numerical Electromagnetic Code,” Defense Technical Information Center, San Diego, 1977.

[77] A. Voors, “4nec2,” 26 January 2015. [Online]. Available: http://www.qsl.net/4nec2/. [Accessed 2 July 2015].

[78] G. Burke and A. Poggio, Numerical Electromagnetics Code (NEC) - Methods of Moments, Pennsylvania: Naval Ocean Systems Center, 1981.

[79] W. C. Gibson, Method of Moments in Electromagnetics, Second Edition, FL, USA: CRC Press, 2014.

[80] I. Stakgold and M. J. Holst, Green's Functions and Boundary Value Problems, Hoboken, New Jersey: John Wiley & Sons, 2011.

[81] Antenna-Theory, “VSWR,” 2013. [Online]. Available: http://www.antenna-theory.com/definitions/vswr.php. [Accessed 1 October 2014].

[82] K. Custer and M. Morris, “Vertical versus horizontal antenna separation,” 2003. [Online]. Available: http://www.repeater-builder.com/antenna/separation.html. [Accessed 26 September 2014].

[83] Polar Electronics, “Polar Electronics - Model 223,” [Online]. Available: http://www.polarelectronicindustries.com/model.php/model_id/226/. [Accessed 1 December 2015].

[84] Times Microwave, “LMR 400,” [Online]. Available: www.rojone.com.au/wp-content/uploads/2011/03/times-lmr400.pdf. [Accessed 15 December 2015].

[85] ZTE Corporation, “Telstra 4g Pre-Paid Wi-Fi,” [Online]. Available: www.ztemobiles.com.au/downloads/User_guides/MF90_Help_PDF.pdf. [Accessed 4 February 2016].

[86] European Broadcasting Union, “ETSI TS 102 563 V1.2.1,” European Telecommunications Standards Institute, 2010.

[87] Committee CT-002, “AS 4943.1,” Standards Australia, 2009.

[88] European Broadcasting Union, “ETSI TR 101 496-3 V1.1.2,” European Telecommunications Standards Institute, 2001.

[89] European Broadcasting Union, “ETSI EN 300 401 V1.4.1,” European Telecommunications Standards Institute, 2006.

[90] S. L. Hahn, Hilbert Transforms in Signal Processing, Michigan: Artech House, 1996.

[91] M. C. Kestwal, J. Sumit and L. Sin, “Prediction of Rain Attenuation and Impact of Rain in Wave Propagation at Microwave Frequency for Tropical Region (Uttarakhand, India),” *International Journal of Microwave Science and Technology,* vol. 2014, 2014.

[92] S. Okamura, “Electromagnetic wave propagation in rain and polarization effects,” *Proceedings of the Japan Academy Series B, Physical and Biological Sciences,* pp. 539-562, 2010.

[93] Bureau of Meteorology, “APS1 upgrade of the ACCESS-C Numerical Weather Pred,” 2013.

[94] D. S. Sawicki, “Cop Radar,” 2015. [Online]. Available: http://copradar.com/preview/chapt2/ch2d1.html. [Accessed 15 May 2015].

[95] Mini-Circuits, “Power Splitter/Combiner - JS4PS-1W+,” [Online]. Available: http://www.minicircuits.com/pdfs/JS4PS-1W.pdf. [Accessed 17 February 2016].

[96] J. Audet, “Coaxial Cable Delay,” [Online]. Available: http://ve2azx.net/technical/CoaxialCableDelay.pdf. [Accessed 1 October 2014].

[97] RF Cafe, “Coaxial Cable Specifications,” [Online]. Available: http://www.rfcafe.com/references/electrical/coax-chart.htm. [Accessed 1 October 2014].

[98] General Cable, “Velocity of Propagation,” [Online]. Available: http://www.generalcable.co.nz/getattachment/f81f14ee-7bec-4841-82d5-84b2df58b4f5/Velocity-of-Propagation.aspx. [Accessed 1 October 2014].

[99] Mini-Circuits, “Digital Step Attenuator - DAT-31R5-PP+,” [Online]. Available: http://217.34.103.131/pdfs/DAT-31R5-PP.pdf. [Accessed 7 December 2012].

[100] Mini-Circuits, “Power Splitter/Combiner - JPS-2-1,” [Online]. Available: http://www.minicircuits.com/pdfs/JPS-2-1.pdf. [Accessed 17 February 2016].

[101] Mini-Circuits, “Digital Controlled Variable Gain Amplifier - DVGA2-33PP+,” [Online]. Available: http://www.minicircuits.com/pdfs/DVGA2-33PP+.pdf. [Accessed 17 February 2016].

[102] Exlexol, “USB I/O 24 R Datasheet,” [Online]. Available: http://www.elexol.com/IO_Modules/documents/USBIO24Rds1.pdf. [Accessed 17 February 2016].

[103] ACMA, “Australia radiofrequency spectrum allocations chart,” [Online]. Available: http://acma.gov.au/~/media/Spectrum%20Transformation%20and%20Government/Publication/pdf/spectrum_chart2013%20pdf.pdf. [Accessed 1 January 2018].

[104] Mini-Circuits, “X3 Frequency Multiplier,” [Online]. Available: https://www.minicircuits.com/pdfs/RMK-3-92+.pdf. [Accessed 30 May 2017].

[105] nVidia, “nVidia Accelerated Computing,” [Online]. Available: https://www.nvidia.com/object/cuda_home_new.html. [Accessed 31 December 2017].

[106] C. Coleman, An introduction to Radio Frequency Engineering, Cambridge: Cambridge University Press, 2005.

[107] M. N and P. Temple, “Australian Atmospheric Sounding Information,” [Online]. Available: http://slash.dotat.org/cgi-bin/atmos. [Accessed 23 November 12].

Appendices

A. 2D and 3D Interpolation

Evaluating different interpolation methods for the output from the propagation tool.

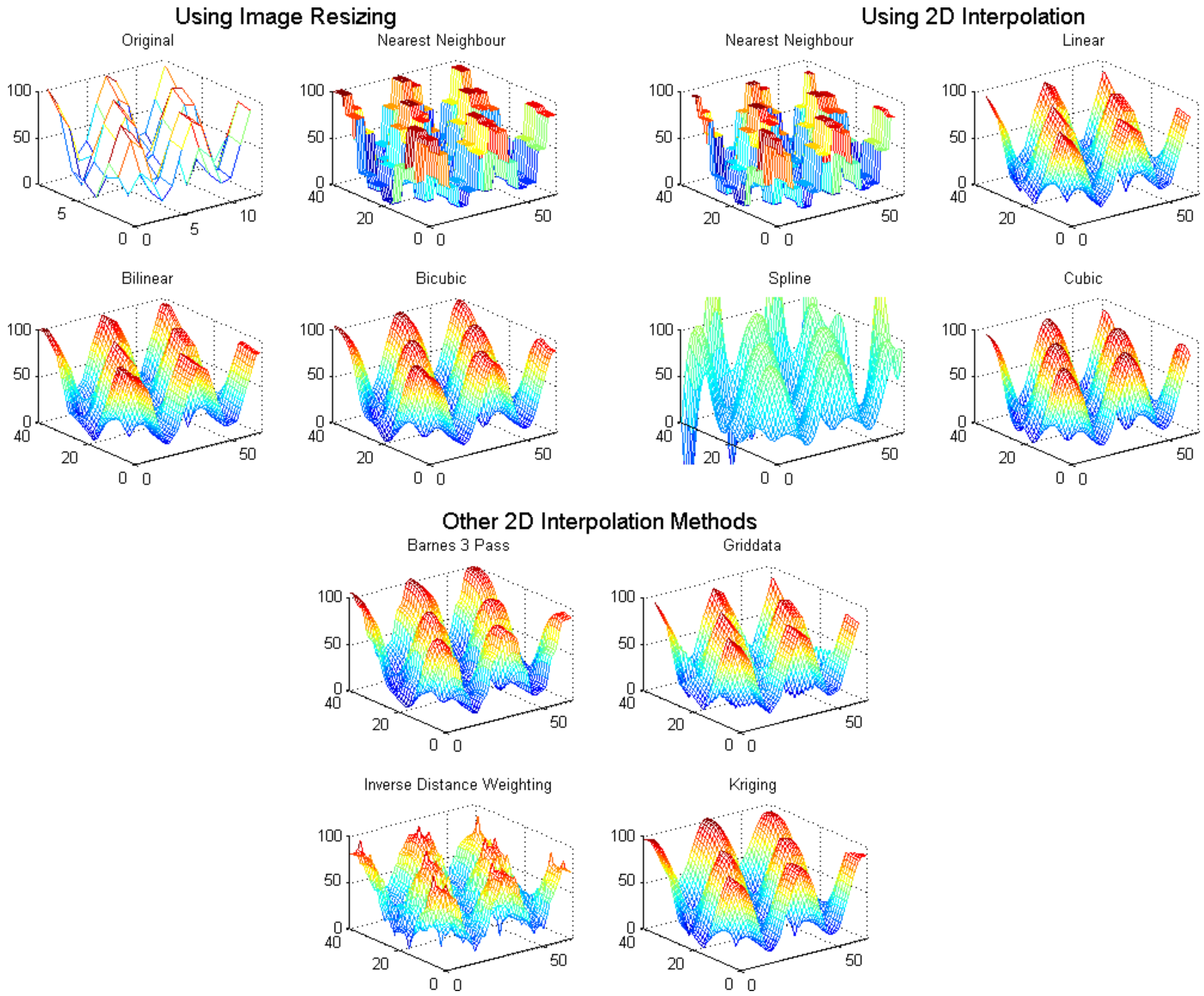

***Figure A-1**: 2D interpolation methods evaluated for terrain surface weather data.*

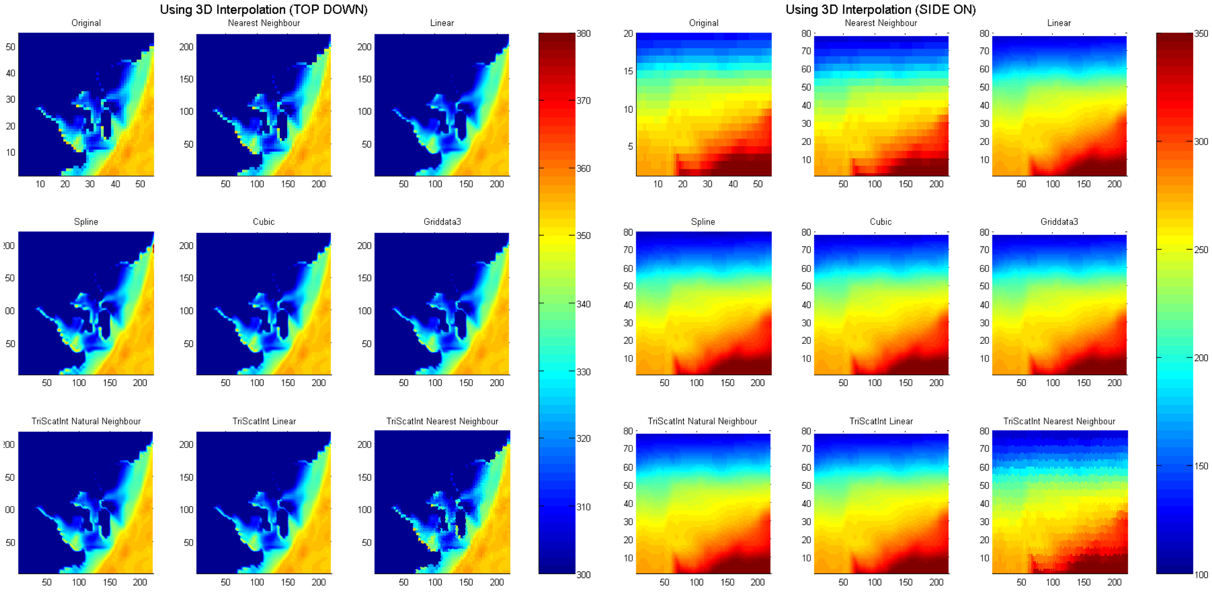
Using 3D Interpolation (TOP DOWN)

Using 3D Interpolation (SIDE ON)

__Figure A-2__: 3D interpolation methods evaluated for Numerical Weather Prediction (NWP) gridded data points.

In the case of 2D surface data, global interpolation methods allow the trend of the data to be taken into consideration instead of just the immediately surround points in a local interpolation. The global interpolation methods unsurprisingly require a large amount of working computer memory to perform the analysis on a large scale. However, for the small amounts of surface data available it was possible to test their performance. The performance of Kriging (an interpolation method used in mining statistical analysis) was also tested and observed to provide a smoothing effect on the interpolated data.

In the 3D data case (as is NWP output), global interpolation methods are impractical due to the sheer number of data points. Only the local interpolation methods are feasible. Illustrated are various 3D local interpolation routines creating a finer mesh of the original data by a factor of 4. Ultimately trilinear interpolation was chosen for its simplicity, speed, and ability to capture localised events.

B. Optimisation Comments

The propagation tool developed offers choice of optimisation routines depending on suitability to the atmospheric conditions. Time invested in investigating the fastest routines, whilst also finding improved optimisation results, has been a big component of the propagation software. There is not any singular best algorithm for a variety of reasons:

- Parallelised routines,
- Atmospheric scenario,
- Local vs global trends,
- Time constraints, and,
- Importance of obtaining the 'true' value to certain significance.

Despite these variables, two preferred approaches are implemented with MATLAB as part of the optimisation toolbox (https://au.mathworks.com/help/optim/index.html):

- a programmable solver to find the minimum of a constrained nonlinear function, and,
- pattern search.

Nonlinear multivariable function (fmincon function within MATLAB) specifies the minimisation problem given limit constraints and initial conditions. These initial conditions heavily influence the optimisation result, independent of the scaling of the function. Fmincon tended to get stuck searching for a result in local minima basins. Obtaining the global minimum can be achieved by a global fmincon (essentially randomising initial conditions).

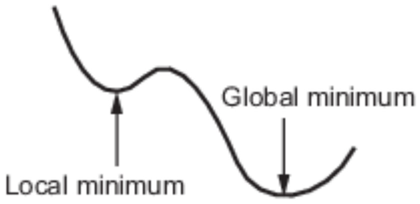

***Figure A-3**: Local vs global optima (image from https://au.mathworks.com, saved 11 April 2015).*

Despite searching for global minimum, MATLAB’s fmincon has a tendency to only moderately provide a better answer than initial conditions.

An alternative also provided by MATLAB’s optimisation toolbox is patternsearch. This is a far more rudimentary approach to locating the minimum of a problem. Fundamentally, a mesh is overlayed on the input function, and the independent variables shifted. Depending on the resulting answer, the mesh is tightened around the variable or loosened and iterates until a specified tolerance is reached in the solution. This function provided the best flexibility for any given atmospheric scenario; but required a longer time to run than local optimisation methods. This optimisation routine was validated against Snell’s Law in Section 2.5.

Due to the independent variables in the input function, optimisation function performance is improved with parallel programming. Systems utilising nVidia’s CUDA-capable graphics cards [105] can yield answers many times faster than multicore desktop systems alone. The second biggest influence on results and run-time come from choosing an appropriate optimisation method, reasonable initial conditions and constraints, and accuracy required in computing the solution.

C. Polarisation Mismatch Experimental Result

Using two LPDA antennas, the approximate effect of the polarisation mismatch to be expected between the two antennas was measured. One transmitting antenna was kept stationary and the second one was set to rotate around the first at a distance of 30 metres, with a transmitter power of 50 mW.

Bearing (degrees N)	Matched Polarisation (dB)	Cross Polarisation (dB)
0	-26	-34
45	-27	-36.7
90	-30.1	-33.4
135	-31.4	-36.3
180	-34.5	-44
225	-34.2	-35.3
270	-31.9	-31
315	-27	-35.4

***Table A-1**: Effect of polarisation mismatch around a Log-Periodic Dipole Antenna (LPDA) from 30 metres away.*

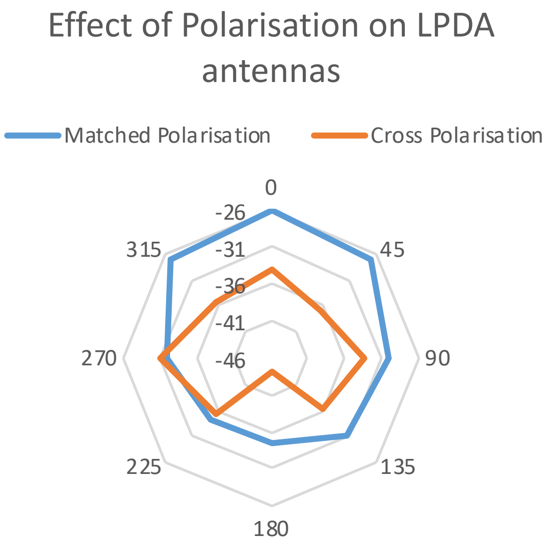

***Figure A-4**: Polarisation mismatch loss at different bearing angles.*

The effect of antenna mismatch on intended direction of propagation was found to be around -10 dB. Several others have performed similar experiments in anechoic chambers free of reflections and noise and obtained results of -20 dB at best.

D. Further Details of Experimental Procedure

1) State time of interest (YYYY-MM-DD HH:MM), remembering that NWP analyses are done hourly Zulu time
    a) Retrieve data from receiver containing the direct signal and repeated signals
        i) Remote desktop into machine if required (NAT traversal remote desktop)
        ii) Locate file matching time of interest, but converted to serial file name
        iii) Locate additional four files ±1 minute (repeated measurements) from time of interest for averaging purposes
        i) Transfer files via Adelaide University FTP server, or physical drive
    b) Retrieve NWP output
        i) Convert local time to UTC, and add two hour offset (required for naming conventions)
        ii) Connect to NCI server that hosts NWP output
        iii) Identify model file & folder based on NWP conventions, preferring earliest analysis
        iv) Optionally concatenate multiple files, but convert all GRUB to netCDF (easier to use)
        v) Securely copy from remote NCI server to local directory. Remove temp files from server
2) Load and process files through scripts
    a) Load the two different files into self-written toolbox in MATLAB
        i) Directly load the saved receiver workspace data
        ii) Import the netCDF file
        iii) Compare timestamp in workspace data to NWP file's 'valid_time' field to verify they are relating to the same atmospheric time (an independent check not based off filenames)
    b) Processing the NWP data to obtain expected path information
        i) Apply the tropospheric propagation tool explained in Chapter 2 with NWP data

        - ii) One of the tool’s outputs will provide a number for the path averaged refractivity
        - iii) Store path (Fermat optimised), as well as expected path averaged refractivity
    - c) Processing the receiver data to obtain recorded timing information
        - i) Separate the two channels of the receiver input
        - ii) Apply the methods described earlier in the thesis. Notably 5.2, 5.2.3
        - iii) Obtain path averaged refractivity from this time
- 3) Process Results
    - a) With two lots of timing information, compare them to validate methodology
        - i) Diurnal measurements. See how the phase changes over a 24-hour period
        - ii) Long-term measurements. See how the phase changes over months
        - iii) Weather event changes. See how the phase changes during storms, etc